INVESTIGATION OF THERMOPHYSICAL ASPECTS OF INFRARED DETECTOR CRYO CHAMBER WITH CRYOCOOLING

Thesis Submitted in partial fulfillment of the requirement for the degree of

DOCTOR OF PHILOSOPHY in MECHANICAL ENGINEERING

By

MAYANK SINGHAL (Roll No. 2K17/PhD/ME/35)

Under the Supervision of

Prof. Rajesh Kumar

Department of Mechanical Engineering Delhi Technological University, Delhi Prof. R.S. Walia

Department of Prod. & Ind. Engineering Punjab Engineering College, Chandigarh

Dr. S. K. Pandey Scientist 'F' DRDO, Delhi



Department of Mechanical Engineering DELHI TECHNOLOGICAL UNIVERSITY (Formerly Delhi College of Engineering) Bawana Road, Delhi- 110042, INDIA

July 2025

CANDIDATE'S DECLARATION

I hereby declare that the research work presented in this thesis entitled "Investigation of Thermophysical Aspects of Infrared Detector Cryochamber with Cryocooling" is original and carried out by me under the supervision of Prof. Rajesh Kumar, Department of Mechanical Engineering, Delhi Technological University, Delhi, Prof. R.S. Walia, Department of Production and Industrial Engineering, Punjab Engineering College, Chandigarh, and Dr. S.K. Pandey, Scientist, 'F', DRDO, Delhi, and being submitted for the award of Ph.D. degree to Delhi Technological University, Delhi, India. The content of this work has not been submitted either in part or whole to any other university or institute for the award of any degree or diploma.

CERTIFICATE BY THE SUPERVISOR(s)

This is to certify that the thesis entitled "Investigation of Thermophysical Aspects of Infrared Detector Cryochamber with Cryocooling" being submitted by Mayank Singhal (2K17/PHDME/35) to the Delhi Technological University, Delhi for the award of the degree of Doctor of Philosophy is a bonafide record of original research work carried out by him. He has worked under our guidance and supervision and has fulfilled the requirements for the thesis submission, which has reached the requisite standard. The results contained in this work have not been submitted, in part or full, to any other University or Institute for the award of any degree or diploma.

Prof. RAJESH KUMAR

SUPERVISOR
Professor
Department of Mechanical Engg,
Delhi Technological University
Delhi-110042, INDIA

Prof. R. S. WALIA

CO-SUPERVISOR
Professor
Department of Production & Ind. Engg,
Punjab Engineering College
Chandigarh-160012, INDIA

Dr. S.K. PANDEY
CO-SUPERVISOR
Scientist 'F'
Defence Research & Development Organisation (DRDO)
Delhi-110054, INDIA

ACKNOWLEDGEMENTS

I want to express my gratitude to my supervisors, Prof. Rajesh Kumar, Prof. R.S. Walia, and Dr. S.K. Pandey, for their valuable guidance, support, and encouragement throughout my Ph.D. program. This work could not have attained its present form without their supervision, direction, and interest in the research work. I express my gratitude to Prof. Atul Agarwal, DRC Chairman, Prof. B.B. Arora, Head of the Department of Mechanical Engineering for providing valuable comments and suggestions. I thank all faculty and staff members of the Mechanical Engineering Department for their continuous and useful support. I appreciate reviewers of research papers and industry people for sparing their valuable time and constructive comments.

I wish to thank my parents, brothers, family members, and friends whose blessings made this work a reality. I sincerely thank my wife, Juhi, and kids, Pranjali and Arnav, for their patience and support in accomplishing this research. I want to acknowledge Gaurav Pratap, my colleague, for his support. At last, I am thankful to the almighty for giving me the mental and physical strength to work sincerely, diligently, and honestly.

MAYANK SINGHAL (2K17/PHDME/35)

ABSTRACT

The present investigation represents a comprehensive analysis of the thermal conditions and phenomena for optimal operational efficiency of infrared (IR) detectors having multiple tactical and civilian applications. An extensive qualitative evaluation of the design considerations linked to the construction of an infrared cryochamber often referred to as a Dewar, that accommodates IR devices has been undertaken. This investigative analysis encompasses a broad spectrum of factors, including the mechanical design elements vital for ensuring structural integrity, the crucial necessity for upholding vacuum integrity to significantly reduce thermal conduction, as well as a thorough examination of the crycooling technologies that are indispensable for achieving the requisite operational cryogenic temperatures. Furthermore, a comprehensive finite volume analysis has been conducted to promote a more profound understanding of the thermal phenomena within the cryochamber such as the conduction heat transfer that occurs through an inner dewar, alongside the gaseous conduction mechanisms that arise because of outgassing phenomena, and complexities involved due to radiative heat transfer processes. Given that conventional analytical methodologies utilize an error function, widely acknowledged for being computationally intensive and resource-demanding, a more generalized numerical model has been adopted for both steady-state and transient thermal analyses.

To ensure that the thermal modelling of the infrared cryochamber undertaken for steadystate and transient conditions is sufficiently reliable and accurate in its predictive capabilities, a comprehensive assessment was conducted for both the grid convergence and the independence of time steps utilized in the simulations,

A comprehensive theoretical and thermophysical investigation of miniature Joule-Thomson (JT) and Stirling cryocoolers has also been conducted to elucidate design considerations and evaluate the influence of specified parameters on the operational efficacy and performance of both coolers. Joule Thomson cryocooler and Stirling cryocooler have been successfully realized as per targeted specifications.

Separate experimental setups were developed for testing cryochambers with JT cooler and Stirling cryocoolers. Results obtained from theoretical analysis and modeling exercise have undergone a rigorous validation process through experimental investigations conducted on developed test setups, to establish the efficacy and reliability of the proposed thermal models.

In the case of the glass cryochamber and JT cooler assembly, the experimental values for cooldown duration in the *device OFF*' mode, is approximately 98 seconds in comparison to the predicted simulation value of 94 seconds at 300 K. The experimental cooldown duration for the same glass cryochamber assembly in the '*device OFF*' mode at 328 K is approximately 116 seconds against the predicted simulation value of 114 seconds. For the same assembly functioning in '*device ON*' mode, the experimental cooldown duration increases to 109 seconds against the predicted simulation value of 105 seconds at 300 K. The cooldown duration is 118 seconds against the predicted simulation value of 116 seconds at 328 K.

In the case of rapid cooldown metallic (Inconel) cryochamber, the experimental results for cooldown duration in 'device OFF' mode, is approximately 10 seconds against the predicted simulation value of 9 seconds when the temperature is 300 K and the value in 'device OFF' mode at 328 K is approximately 11 seconds matching with the simulated value of 11 seconds. In 'device ON' mode, the experimental value of cooldown duration for the same assembly is 12 seconds and matches the predicted value of 12 seconds at 300 K while the cooldown duration is 14 seconds against the predicted simulation value of 13 seconds at 328 K.

Consequently, the numerical analysis accurately predicts the duration required for the cooldown process, as evidenced by an empirically observed maximum deviation of approximately 4.2% when applied to the case of glass cryochamber, while exhibiting a significantly lower error of 1% in the context of the rapid cooldown metallic cryochamber.

The thermal model enables the prediction of transient cooling performance of the cryochamber under various conditions viz., 'device OFF' and 'device ON' conditions, variation in ambient temperature, variation in cryochamber vacuum, and for varying materials and dimensional configurations with differing material and transport properties.

RESEARCH PUBLICATIONS

Journal Papers

- Mayank Singhal, Rajesh Kumar, R.S. Walia & S.K. Pandey 'Experimental Investigation and Thermophysics Analysis of Joule-Thomson Cooler Applicable to Infrared Imaging', **Defence Science Journal**, Vol. 73, No. 4, July 2023, pp. 457-467, DOI: https://doi.org/10.14429/dsj.73.18686
- Mayank Singhal, Rajesh Kumar, R.S. Walia & S.K. Pandey 'Evaluation of Tribological and Cooling Performance of TiN and DLC-coated pistons for miniature Stirling Cryocooler', MAPAN (2024) https://doi.org/10.1007/s12647-024-00764-z

Conference Papers

- Mayank Singhal, Rajesh Kumar, R.S. Walia & S.K. Pandey 'Development of a Sintered Porous Neck Filter for miniature Joule Thomson Cryo-cooler for cooling Infrared detectors', 2020 IOP Conf. Ser.: Mater. Sci. Eng. 748 012013 DOI 10.1088/1757-899X/748/1/012013
- Mayank Singhal, Rajesh Kumar, R.S. Walia & S.K. Pandey 'Thermophysics analysis of recuperative heat exchanger-based miniature J-T cooler applicable to IR devices', Paper presented at 13th International Exergy, Energy and Environment Symposium (IEEES-13); 14-17 March'2022; Umm Al-Qura University & College of Engg., Makkah, Saudi Arabia

TABLE OF CONTENTS

		Pag	ge No.
Cana	lidate's L	Declaration	i
Certi	ficate by	the Supervisor(s)	ii
Ackn	owledgei	ments	iii
Abstr	act		iv-v
Resea	arch Pub	olications	vi
Table	e of Cont	tents	vii-x
List o	of Figure	S	. xi-xv
List o	of Tables		xvi
Nome	enclature	?x1	vii-xix
Chaj	pter 1:]	Introduction and Literature Review	1
1.1.	Introd	uction	1
	1.1.1.	Fundamentals of Infrared (IR) Imaging	1
	1.1.2.	Infrared (IR) Imaging: Applications and Detection	3
	1.1.3.	Cryogenics and Need for Cryocooling	5
	1.1.4.	Cryochambers or Dewars	6
1.2.	Literat	ture Review	7
	1.2.1.	Studies on Realms of Thermal Sensor Operation	9
	1.2.2.	Studies on Thermal and Thermo-Mechanical Analysis of Cryochamber	10
	1.2.3.	Studies on Cryocooling Technologies for Infrared Detector Cryochamber	17
	1.2.4.	•	
	1.2.5.		
	1.2.6.	Brief Research Methodology	25
		Expected Outcome of Proposed Research Work	
Cha	pter 2: l	Design Aspects of IR Cryochamber	26
2.1.	-	yochambers or Dewars	
	_	Rapid Cool-down Dewars	27

2.2.	Details	s for Cryochamber Design	28
	2.2.1.	Required Thermal Load Capacity	29
		2.2.1(a). Estimation of Thermal Mass & Heat Load of Dewar	30
	2.2.2.	Required Operational Temperatures	31
	2.2.3.	Cryochamber Material	31
	2.2.4.	Specifications of Bond Wires	31
	2.2.5.	Dimensions of the Inner Dewar's Bore and Length	33
	2.2.6.	Diameter of Cryogenic Chamber	33
	2.2.7.	Specifications Regarding the Window Type, Cold Filter, or Shield	33
	2.2.8.	Dewar Degassing Through Thermal Baking	34
	2.2.9.	Implementation of Dewar Pinch-off for Sealing	35
	2.2.10	. Types of Getters	36
	2.2.11	. Temporal Parameters Such as Duration of Cool-down and Hold-on for the Cryogenic Chamber	38
	2.2.12	Selection of Appropriate Cryocooler	
		2.2.12(a). Cryocooler Characteristics and Its Requirement	
		2.2.12(b). Choosing a Cryocooler for IR Detector Cryochamber	40
	2.2.13	Design for Mechanical Strength	
		. Assessment of Mechanical Integrity and Robustness of the Cryogenic Chamber	
Chaj	oter 3: (Computational Modelling of IR Cryochamber	46
3.1.	Comp	utational Geometry	46
3.2.	Therm	al Loss Mechanisms	47
3.3.	Nume	rical Formulation	48
	3.3.1.	Steady State Operating Mode	48
	3.3.2.	Transient Operating Mode	50
3.4.	Result	s of Thermal Modelling	53
	3.4.1.	Results for Steady-state Case	53
	3.4.2.	Results of a Transient Case	59
Chaj		Thermophysical Analysis and Prototype Development	61
4.1.		of Miniature Joule Thomson Cryocoolerption of Miniature Joule Thomson Cryocooler	
4.1. 4.2.		etical and Thermophysics Analysis	
Τ.Δ.	THEOR	and incimophysics Analysis	03

4.3.	Geometrical Parameters of the J-T Cooler		
4.4.	Thermo-Fluidic Parameters of the J-T Cooler6		
4.5.	Effect of Various Parameters on J-T Cryocooler Performance		
4.6.	Typical Miniature Joule-Thomson Cooler Specifications		
Chaj	pter 5: Thermal Analysis and Prototype Development of Miniature Stirling Cryocooler	75	
5.1.	Description of Stirling Cryocooler		
5.2.	Thermodynamic Analysis		
5.3.	Sample Calculation to determine the Compressor Piston and Regenerator Tube Sizes		
5.4.	Calculations for Design Optimization		
5.5.	Loss Evaluation of System		
	5.5.1. Regenerator Ineffectiveness Loss		
	5.5.2. Pressure Drop Loss		
	5.5.3. Longitudinal Conduction Loss		
	5.5.4. Regenerator Efficiency		
	5.5.5. Shuttle Heat Transfer Loss		
	5.5.6. Dewar Losses	87	
5.6.	Analysis Results	87	
5.7.	Effect of Various Parameters on Stirling Cryocooler Design and Performance	94	
	5.7.1. Effect of Thickness and Material Thermal Conductivity on Cold Finger Design	94	
	5.7.2. Effect of Type of Coating on Cryocooler Pistons	95	
	5.7.2(a). Coating Methodology	95	
	5.7.2(b). Characterization of the Coating	96	
	5.7.2(c). Testing of Coolers with Coated Pistons	100	
5.8.	Developed Stirling Cooler Prototype	102	
Chaj	pter 6: Experimental Testing and Validation	103	
6.1.	Experimental Test Setup for Cryochamber Testing with JT Cooler	103	
	6.1.1. Actual Experimentation	104	
	6.1.2. Testing with Glass Cryochamber	105	
	6.1.3. Testing with Rapid Cooldown Inconel Cryochamber	106	
6.2.	Experimental Test Setup for Cryochamber Testing with Stirling Cooler		

Chap	oter 7: Conclusions	111
7.1.	IR Cryochamber	115
7.2.	Joule Thomson (JT) Cryocooler	116
7.3.	Stirling Cryocooler	117
7.4.	Industrial Relevance or Technology Readiness Level (TRL)	117
Chap	oter 8: Recommendations for Future Work	118
Refe	rences	120

LIST OF FIGURES

Figure No.	Title	Page No.
Figure 1.1	ElectromagneticSpectrum	2
Figure 1.2	Comparative analysis of conventional imaging (a) to infrared imaging (b)	
Figure 1.3	Typical Infrared (IR) cryochamber	6
Figure 1.4	Spectral blackbody emissivity power at different temperatures [14]	
Figure 1.5	Schematic of a cryogenic chamber incorporating a radiation barrier	
Figure 1.6	Heating wire and cold finger	13
Figure 1.7	Parts of a JT cooler	18
Figure 1.8	Schematic representation of Stirling cryocooler	21
Figure 2.1	Section of an Infrared (IR) dewar or cryochamber	29
Figure 2.2	Multipin feedthrough bonding to detector carrier with thin wire	
Figure 2.3	HTCC Feedthrough	32
Figure 2.4	(a) Metalized Germanium Window (\$\phi\$ 15mm) & (b) Cold Filter (\$\phi\$ 12mm)	
Figure 2.5	Cold Shield (a) Conical & (b) Baffled type	34
Figure 2.6	Cryochamber degassing station	35
Figure 2.7	Methods for Sealing a Cryochamber	36
Figure 2.8	Getter operation and the type used in IR cryochamber	37
Figure 2.9	Temperature and Pressure plot for varying enthalpies with inversion curve	
Figure 2.10	A typical (a) Joule Thomson (JT) cooler and (b) Stirling Cooler	-
Figure 3.1	Computational geometry and thermal loss mechanisms	47
Figure 3.2	Influences of thermal fluxes on unit element	48

Figure No.	Title	Page No.
Figure 3.3	Temperature length profile for diverse coefficients of gar conduction	
Figure 3.4	Emissivity length profile for diverse values of emissivity	55
Figure 3.5	Temperature distribution along the length for h=1.0	57
Figure 3.6	Temperature length profile for diverse coefficients of gas conduction for SS cryochamber	
Figure 3.7	Computational detector cool down time (CDT) for Case2 a an ambient temperature of 300K & 328 K under "device OFF" condition	e
Figure 3.8	Computational detector cool down time (CDT) for glass cryochamber at an ambient temperature of 300K & 328 k under "device ON" condition	
Figure 3.9	Computational detector CDT for Inconel cryochamber a ambient temperature measuring 300K & 328 K for "device OFF" state	e
Figure 3.10	Computational detector CDT for Inconel cryochamber a ambient temperature measuring 300K & 328 K for "device ON" state	e
Figure 4.1	(a) JT cooler with recuperative H.E (b) T-S diagram for JT cooler	
Figure 4.2	Geometry of Helical Tube fin	67
Figure 4.3	Impact of mass flow rate on heat exchanger performance	70
Figure 4.4	Variation of cooling capacity and pressure drop for hea exchanger	
Figure 4.5	Impact of fin density on HX effectiveness	71
Figure 4.6	Impact of fin density on the drop in pressure in the hea exchanger	
Figure 4.7	Impact of fin length on the drop in pressure in the HX	72
Figure 4.8	Relation between supply pressure and the cryocoole capacity	
Figure 4.9	Generic Flow chart for computational modelling of JT coole	

Figure No.	Title	Page No.
Figure 4.10	(a) Developed Prototype of JT Cryocooler (b) Prototype in a glass dewar	
Figure 5.1	Stirling coolers (a) split type (b) integral type	75
Figure 5.2	Ideal Stirling cycle: (a) P-V diagram (b) T-S diagram	76
Figure 5.3	Schematic representation of Stirling refrigerator	76
Figure 5.4	Processes of an Ideal Stirling Refrigerator	77
Figure 5.5	Ideal Stirling cycle phase diagram	77
Figure 5.6	Theoretical P-V curve for cryocooler (a) Expansion space (b) Compression space (c) Total working space	
Figure 5.7	Result of design parameters on dimensionless ne refrigeration/work done for different dead volume ratios X (a) α (b) κ (c) dead volume ratios	:
Figure 5.8	(a) Variation of Cooler speed vs heat lifted (b) variation of heat extracted vs temperature in expansion space	
Figure 5.9	Design method of regenerator	88
Figure 5.10	(a) Regenerator losses for wire mesh size 400 (b) Pressure drop loss	
Figure 5.11	(a) Effectiveness of regenerator with length (b) Efficiency o regenerator vs length	
Figure 5.12	(a) Convective and Conductive heat load for different cold- tip temperatures (b) Conduction and radiation losses for cold-tip, radiation loss on second Y-axis	r
Figure 5.13	Shuttle heat transfer loss as a function of stroke length for various radial clearances	
Figure 5.14	Generic Flow chart for computational modelling of Stirling cooler	
Figure 5.15	Effect of cold Finger Thickness and thermal conductivity or Heat Transfer	
Figure 5.16	Piston and cylinder pair of a Stirling cryocooler	96
Figure 5.17	Piston samples (1&2- TiN coated, 3 & 4- DLC coated)	96
Figure 5.18	EDAX elemental concentration & analysis of base materia and both coatings	

Figure No.	Title	Page No.
Figure 5.19	Microstructure of TiN & DLC samples after indentation (left to right)	
Figure 5.20(a)	Grazing Incidence X-ray diffraction (GIXRD) patterns of DLC-coated Piston	
Figure 5.20(b)) Grazing Incidence X-ray diffraction (GIXRD) patterns of TiN-coated Piston	
Figure 5.21	TiN & DLC coated pistons before and after the cooler operation	
Figure 5.22	Time vs Cold tip temperature (left) and power characteristics (right) for TiN coated piston (a-b) &DLC coated piston (c-d)	
Figure 5.23	Specification of Stirling cryocooler prototype developed	102
Figure 6.1	Test setup for integrated cryochamber and JT cryocooler assembly	
Figure 6.2	Experimental detector cool down time (CDT) for glass cryochamber at an ambient temperature of 300K & 328 K under "device OFF" condition	
Figure 6.3	Experimental detector cool down time (CDT) for glass cryochamber at an ambient temperature of 300K & 328 K under "device ON" condition	
Figure 6.4	Experimental detector cool down time (CDT) for Inconel cryochamber at an ambient temperature of 300K & 328 K under "device OFF" condition	
Figure 6.5	Experimental detector cool down time (CDT) for Inconel cryochamber at an ambient temperature of 300K & 328 K under "device ON" condition	
Figure 6.6	Test setup for testing integrated cryochamber and Stirling cryocooler	
Figure 6.7	Screenshot of (a) Cooldown & (b) Power consumption of Stirling cryocooler	
Figure 7.1	Comparison chart for predicted and experimental values of the cool-down duration for glass cryochamber under 'device OFF' condition	

Figure No.	Title	Page No.
Figure 7.2	Comparison chart for predicted and experimental values of the cool-down duration for glass cryochamber under 'device ON' condition	;
Figure 7.3	Comparison chart for predicted and experimental values of the cool-down duration for Inconel cryochamber under 'device OFF' condition	•
Figure 7.4	Comparison chart for predicted and experimental values of the cool-down duration for Inconel cryochamber under 'device ON' condition	•

LIST OF TABLES

Table No.	Title	Page No.
Table 1.1	Classification of Infrared Electromagnetic Waves	3
Table 1.2	Categorization of Cryochambers or Dewars	6
Table 3.1	Comparative Properties of different Inner Cryochambers Studied	54
Table 3.2	Properties of Glass Inner Cryochamber (Case-I)	54
Table 3.3	Properties of Glass Inner Cryochamber Prototype Developed (Case2)	56
Table 3.4	Properties of Inconel Inner Cryochamber Prototype Developed (Case3)	58
Table 5.1	Heat balance of Stirling cryocooler	92
Table 5.2	General parameters for TiN and DLC coating	95
Table 5.3	Elemental concentration of TiN Sample	98
Table 5.4	Elemental concentration of DLC Sample	98
Table 5.5	Microhardness of TiN and DLC coated piston on HV0.5 scale	98
Table 6.1	Comparison of Targeted specifications and the achieve specifications for the Stirling cooler	

NOMENCLATURE

- A Cross-sectional area of flow passage (m^2)
- C_p Specific Heat at constant pressure $\binom{J}{k_g K}$
- C Heat capacity rate of fluids defined by the product of m and $C_p(W/K)$
- C_r Heat capacity ratio
- d Diameter (m)
- d_{if} Inner diameter of finned tube (m)
- d_{of} Outer diameter of finned tube (m)
- d_{ofb} Outer diameter of finned tube without fins (m)
- D_e Equivalent diameter (m)
- D_h Helix diameter (m)
- f Fanning friction factor
- g_f Gap between to fins (m)
 - G Mass velocity, $\binom{K_g}{m^2 s} (G = m/A)$
 - h Coefficient of Heat Transfer $(W/m^2 K)$
 - k Thermal conductivity of wall material $(W/_{m-K})$
 - L Length of Heat exchanger (m)
- \dot{m} Mass flow rate $\binom{k_g}{s}$
- N_f Number of fins
- N Number of transfer units for individual fluid stream
- NTU Overall number of transfer units
 - p Perimeter of heat transfer (m)
 - Q Heat transfer (watt)
 - U Overall heat transfer coefficient $(W/m^2 K)$
 - x Axial co-ordinate of heat exchanger (m)
 - X Dimensionless axial co-ordinate in heat exchanger defined by $^{\chi}/_{L}$

 C_p Specific heat at constant pressure (J/Kg-K)

 k_m Wire mesh thermal conductivity (W/mK)

 k_{eff} Effective thermal conductivity (W/mK)

p_{mean} Mean pressure (Bar)

 Q_{net} Net refrigeration produced (Watt)

 Q_{max} Maximum refrigeration produced (Watt)

 Q_{exp} Expansion side heat removal (Watt)

Ntu Number of the transfer unit

 T_{comp} Temperature in compression side (K)

 T_{exp} Temperature in expansion side (K)

 T_{mean} Mean temperature (K)

 V_{exp} Expansion volume (m³)

V_{comp} Compression volume (m³)

X Dead volume ratio

 δ Intermediary parameter

au Temperature ratio

 α Phase difference

 ε Effectiveness

 \dot{m} Mass flow rate (Kg/sec)

 Ψ Regenerator efficiency

Greek symbols

σ Stefan Boltzmann constant $(W/_{m^2K^4})$

- ρ Density of the working medium $\binom{k_g}{m^3}$
- ε_s Emissivity of the outer shield
- ε_r Emissivity of the ambient
- ϕ Dimensionless Pressure
- θ Dimensionless temperature
- η_o Adiabatic efficiency
- η_f Efficiency of the fin
- Γ Relative residual flux

Subscripts

- 1-5 State points
- a Ambient
- c Cold fluid
- c_i Capillary inside
- c_o Capillary outside
- f Fin
- *f* Fin tube
- h Hot fluid or High-Pressure gas
- in Inlet
- m Mandrel
- m_o Mandrel outside
- o Outer
- out Outlet
- r Radiation
- s Shield
- s_i Shield inside
- s_o Shield outside
- w Wall of finned capillary

1.1 Introduction

The utilization of thermal sciences is expanding beyond traditional engineering fields into unexplored areas. A contemporary example includes assessing and forecasting the thermal performance of infrared (IR) detector cryochambers or dewars maintained at low temperatures by compact cryocoolers meeting stringent cooling requirements. IR detectors are sensitive to temperature, requiring cryochamber for optimal performance. This entire configuration, comprising a detector enclosed within a Dewar and thermally regulated by a cryocooler, is typically designated as an Integrated Detector Cooler Assembly (IDCA).

1.1.1 Fundamentals of Infrared (IR) Imaging

The Latin prefix "infra" signifies the notion of "below" or "beneath." Infrared refers to the electromagnetic waves just below the visible light spectrum. This rapidly evolving technology has become increasingly ubiquitous. The word "infrared" specifically refers to the segment that lies immediately beyond or below the red area of the visible light spectrum. This infrared spectrum is situated between the domains of visible light and microwaves. As objects at elevated temperatures emit energy within this infrared spectrum, it is often characterized as the thermal portion of the electromagnetic spectrum. Historically, infrared radiation has been associated with "thermal energy" or "thermal radiation." which has led to a common misconception that all types of radiant heating originate from infrared light and that all infrared radiation is intrinsically associated with thermal energy. This perspective constitutes a prevalent fallacy, as any wavelength of light and electromagnetic waves can raise the temperature of surfaces absorbing them. The radiation released in the infrared range by the Sun is responsible for approximately half of the Earth's heating, the remaining is attributed to absorbed visible light which is subsequently re-emitted at longer wavelengths. Every object emits a quantifiable amount of energy within the infrared spectrum, including one at ambient temperature and even ice.

Certain attributes of infrared radiation include its tendency to propagate in a linear manner (with significant exceptions relevant to our field), its inability to penetrate metallic materials except when they are exceedingly thin, and its capacity to pass through various crystalline, polymeric, and gaseous substances, encompassing the atmosphere of Earth. Infrared (IR) radiation constitutes a category of electromagnetic energy that adheres to principles analogous to those governing light, radio waves, and X-rays. Wavelength is the primary differentiator of IR radiation from these other forms. The diagram of an electromagnetic spectrum shown in Figure 1.1 depicts the distinction.

The limits that define visible light, infrared radiation, far-infrared radiation, and millimeter waves are not definitive; these categories have been established mainly for the sake of convenience in understanding and communication with crucial considerations being the sources employed and the detection instruments available. Typical light pertains to the spectrum part perceptible to the eye of a human. Conversely, millimeter waves represent the minimal wavelengths that can be identified using the most compact microwave-like devices, whereas infrared and far-infrared wavelengths are positioned within this spectrum.

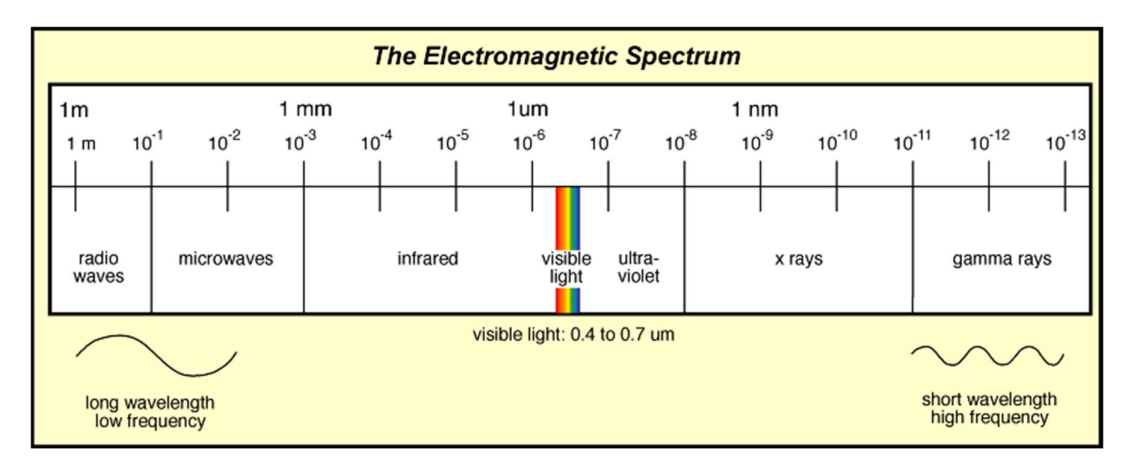


Figure 1.1 Electromagnetic Spectrum

Most infrared (IR) detectors predominantly exploit the existence of two specific atmospheric "windows," defined as spectral ranges that demonstrate highly advantageous transmission characteristics in the range of 3 to 5 micrometers and 8 to

12 micrometers. Consequently, it is entirely justifiable to consider the primary infrared spectrum as a range that spans from 3 micrometers to 12 micrometers [1]. Infrared techniques operate effectively across wavelengths from $0.7\mu m$ to $1000\mu m$. The conventional classification of the infrared spectrum is as in Table 1.1 below.

Table 1.1 Classification of Infrared Electromagnetic Waves [1]

Spectral Region (abbreviation)	Range of Wavelength (µm)
Near-Infrared (NIR)	0.78 -1
Short Wavelength- Infrared (SWIR)	1-3
Medium Wavelength -Infrared (MWIR)	3-6
Long Wavelength -Infrared (LWIR)	6 -15
Very long Wavelength -Infrared (VLWIR)	15 -1000

1.1.2 Infrared (IR) Imaging: Applications and Detection

The corpus of human understanding regarding infrared (IR) radiation dates back approximately two centuries. However, it was only at the end of the 20th Century that different sets of technologies for detection were identified and utilised successfully. [2]

Sir William Herschel identified the Infrared segment of the electromagnetic spectrum in 1800, and since then the evolution of infrared engineering and IR detector development have progressed concurrently. He conducted experiments to quantify energy distribution within sunlight utilizing a thermometer as a sensor. Building upon the contributions of Stefan Boltzmann, Kirchhoff, Rayleigh, Max Planck, and Wien ultimately advanced this pursuit with the renowned Planck's law. While the initial implementations of infrared (IR) technology primarily focused on detecting IR radiation, subsequent advancements evolved towards developing novel detectors and their application through the formation of IR arrays. Infrared (IR) detectors function analogously to visual organs and are often called optical sensing instruments within the digital operational environment. The demand in this field has been notably shaped and propelled by military applications in Western nations, akin to numerous other developing sectors. Beyond the diverse military utilizations of IR systems, which

include target acquisition, search, tracking, and missile guidance, the substantial potential for IR technologies exists in the commercial sphere, particularly due to the contraction and increasing specialization of the military market. It is estimated that around 20% of the market pertains to commercial applications. Forecasts indicate that in the next ten years, expansion surpassing 70% in volume and 40% in financial worth is expected in the commercial sector [3].

Civilian applications include assessments of thermal efficacy, remote temperature surveillance, short-range wireless transmission, spectroscopy, atmospheric prediction, and biological and medical applications for embryo and damaged tissue identification [4]. Infrared astronomy employs telescopes equipped with sensors to explore obscured areas of the universe, such as molecular clouds; detect celestial phenomena, and examine objects exhibiting substantial redshift originating from the universe's formative period.

Under infrared illumination, the surroundings disclose characteristics concealed under conventional visible light [5]. Humans and animals become significantly more visible in complete darkness, structural flaws are exposed, components nearing failure emit enhanced luminosity, and visibility is augmented in challenging conditions through infrared light when the observed scene is filled with smoke or the background is foggy.



a) The visual representation observed under standard illumination



b) The identical scene depicted in (a) as perceived through IR imaging

Fig 1.2 Comparative analysis of conventional imaging (a) to infrared imaging (b) As illustrated in Figure 1.2, the left image below exemplifies what one might observe under typical illumination conditions during a nocturnal setting. The depiction to the right illustrates the identical environment as perceived through an infrared imaging

device. It is evident that thermally elevated entities, such as human figures, are distinctly discernible from the generally cooler surroundings, irrespective of the existing visible illumination. Such detection capabilities are attainable through the utilization of appropriate infrared cameras and can prove advantageous in a myriad of military contexts.

1.1.3 Cryogenics and Need for Cryocooling

The branch of science that studies extremely low temperatures is called Cryogenics. Although it is generally accepted to be 120 K, the highest limit for cryogenic temperatures is not defined specifically.

Cryogenic temperatures are required to transport liquefied gases (LNG, etc.), gas purification, cryo pumping, and preserve biological stuff (blood, tissue, edibles, etc.). The magnetic field of certain materials increases due to a reduction in electrical resistance at cryogenic temperatures [6]. This superconducting effect is used in magnetic trains and MRI/NMR [7].

Notwithstanding the prevalent use of uncooled night vision technology, cooled systems continue to be recognized for their superior performance, characterized by diminished thermal noise, enhanced resolution [8,9], and the capability to identify and track rapidly moving objects within dynamic infrared environments [10,11].

Infrared (IR) detectors require cooling, typically below 123 K or -150°C (cryogenic temperature). This requirement arises from their inability to operate effectively at ambient temperatures or their performance enhancement when subjected to lower temperatures. Nonetheless, the necessity for such low-temperature functionality complicates the deployment of IR detectors. Additionally, this demands meticulous thermal analysis to determine the cooling requirements pertinent to each distinct application, given that these detectors engage thermally with their environment. Such analysis is essential for the formulation of appropriate cooling strategies that are specifically designed for individual scenarios.

1.1.4 Cryochambers or Dewars

From a scientific perspective, a vacuum vessel, commonly known as a thermos, is formally designated as a dewar, in honour of its inventor, Sir James Dewar. A diverse array of dewars exists, encompassing small glass receptacles with diameters of less than one inch to expansive testing chambers. Cryogenic substances are prone to rapid evaporation, and dewars are meticulously engineered to insulate them from elevated thermal conditions. An optimally designed dewar effectively minimizes thermal transfer via radiation, conduction, and convection, necessitating meticulous design considerations to maintain the desired thermal performance. These cryogenic vessels or dewars can be systematically classified in the subsequent table:

Table 1.2 Categorization of Cryochambers or Dewars

Category	Application/Purpose
Storage Cryochamber or Dewar	Cryogenic temperature storage of nitrogen, oxygen, argon, air, and helium in liquid state
Test Cryochamber or Dewar	For initial laboratory testing of devices grown on semiconductor material
Tactical Cryochamber or Dewar	For packaging a device for real war scenarios such as missiles, tanks, and thermal imaging

A typical IR cryochamber is shown in Figure 1.3 below.

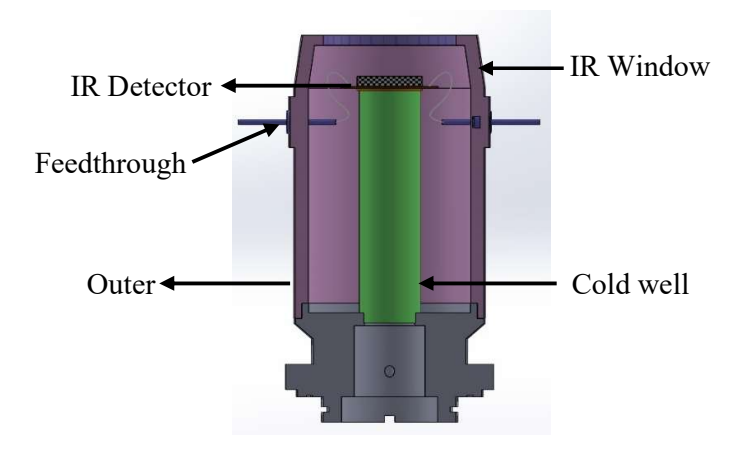


Figure 1.3 Typical Infrared (IR) cryochamber

The apparatus features several main components, specifically: i) an outer vacuum vessel, ii) a thin-walled inner dewar, iii) a ceramic feed-through, iv) an infrared (IR) sensor placed on the inner dewar or cold well, and v) an IR silicon/germanium window, which functions as the upper surface of the cryochamber and allows only signal in IR range to pass through. Typically, the outer vacuum vessel is fabricated from materials such as stainless steel or Kovar, and the Inner Dewar, or cold finger, is a slender cylindrical container constructed from steel, glass, or alloys like Inconel or Invar. The structural integrity of the glass necessitates a greater thickness compared to steel. The base of the apparatus may also be composed of Kovar or stainless steel. The interstitial region between the cold well and the vacuum chamber is preserved in a vacuum condition to minimize thermal dissipation, accomplished through evacuation using a pump. The inner dewar is of cylindrical geometry, and the cooling mechanism is enhanced by an ancillary cooling apparatus, which may utilize a range of refrigeration techniques, such as Joule—Thompson or Stirling cryocoolers.

1.2 Literature Review

Every atom releases infrared radiation due to electrons moving between different energy levels [12].

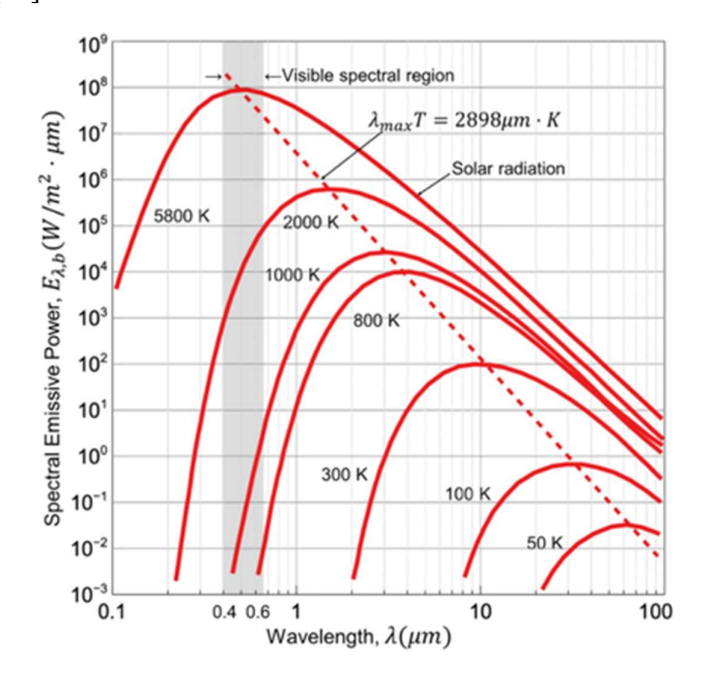


Figure 1.4 Spectral blackbody emissivity power at different temperatures [14]

There exist two principal approaches to infrared detection: thermal (energy-based) detection and quantum (photon-based) detection [13]. Figure 1.4 illustrates how an atom generates varying amounts of infrared light at various wavelengths for every temperature and IR detectors are used to detect these IR wavelengths.

Thermal sensors exhibit responsiveness to variations in temperature induced by incoming infrared radiation via alterations in material characteristics and do not necessitate cooling mechanisms. The interaction of photons with electrons leads to the production of free charge carriers in quantum sensors. The economic viability of energy sensors is notable, and they are primarily utilized in singular detection scenarios, with widespread applications in fire alarm systems and automated lighting controls. In range-finding systems and thermal imaging, the employment of cooled quantum detectors yields superior detection capabilities and quicker response intervals. A cooling mechanism in conjunction with quantum detector-based detection methodologies is generally required. A concise overview of the extensive body of literature addressing infrared detectors and their associated cooling mechanisms is presented in the following section.

The literature review has been carried out keeping the following perspectives in view:

- > Studies on realms of thermal sensor operation
 - Thermal radiation attributes, such as pertinent spectral range, atmospheric transmittance, the necessity for visualization, and the merits of cooling, are important.
 - Empirical techniques for the identification of thermal radiation
 - Techniques for interrogation and comparative analysis
 - Signal processing
- > Studies on thermal and thermo-mechanical analysis of cryochamber
 - Analytical/ Empirical analysis of thermal/ heat transfer
 - Computational thermal modelling
 - Experimental studies

- > Studies on cryocooling technologies for infrared detector cryochamber
 - Different applicable cryocooling technologies
 - Miniature and Multistage coolers
 - Motive fluids

The various works have been further analyzed in terms of:

- Proposed approach/ scheme
- Numerical/ Analytical/ Empirical models employed
- Obtained experimental results and model validation

1.2.1 Studies on realms of thermal sensor operation

The utilization of infrared (IR) detectors and focal plane arrays (FPAs) is prevalent in the acquisition and tracking part of target systems. An infrared director (IR) as a transducer transforms radiant energy within the infrared spectrum into a quantifiable format. As infrared radiation is independent of visible light, it detects the infrared energy emitted from the scene thus facilitating visibility in low-light or obstructed conditions. The energy captured is converted to images that illustrate the difference in energy dissipated within objects, enabling the observation of a scene that would otherwise be obscured.

Infrared imaging seekers and thermal imaging devices for their operation utilize cryogenically cooled focal plane arrays operating at 77K or lower. The detector dewar cooler assembly, which incorporates a Joule-Thomson cooler, alongside the Integrated Detector Cooler Assembly featuring a mini Stirling cooler, currently serves as the fundamental component for thermal imaging devices and missile seekers, respectively. Investigative initiatives have been directed towards enhancing the uniformity and crystalline integrity of detector materials, refining signal processing capabilities at the focal plane, developing advanced materials, minimizing size, weight, and power (SWaP), and increasing the reliability of infrared systems. [15]

Infrared detectors are extensively utilized across both industrial and commercial sectors. The efficacy of infrared detectors is significantly influenced by temperature, achieving optimal functionality when subjected to cryogenic conditions approximating 120K. Tidrow and Dyer [16] provided a comprehensive assessment of the current advancements in infrared sensors, elucidating the benefits and limitations associated

with various infrared material systems for applications in space exploration. Crucial characteristics for future focal plane arrays (FPAs) encompass large format, elevated sensitivity, minimal noise, excellent uniformity, and enhanced operability.

Amir Karim et al. [17] provided an overview of infrared (IR) detectors, emphasizing the obstacles encountered by contemporary IR detection technologies and the anticipated requirements for future advancements. The domain of high-performance infrared detector technology is advancing into a novel phase marked by heightened expectations concerning detection efficiency, operational temperatures, and, the ability for multicolor detection. Several significant emerging IR detector technologies were addressed in the analysis. Quantum dot-based infrared photodetectors (QDIPs) are projected to offer benefits such as elevated operational temperatures, normal incidence capabilities, multicolor detection, and reduced dark current. Although considerable research has been conducted on QDIPs, this technology continues to experience challenges related to low quantum efficiencies. The Type-II strain layer superlattice (T2SL) is the most advanced and novel Infrared detector technology.

Webb [18] examines pragmatic approaches for identifying thermal radiation and the methodologies through which detection instruments analyze and differentiate the observed environment. The processing of the acquired signal with various novel electronic components is also discussed.

1.2.2 Studies on thermal and thermo-mechanical analysis of cryochamber

The necessity for ruggedization is particularly pertinent for Integrated Detector Cryogenically Cooled Infrared Assembly (IDDA), wherein the infrared detector is mounted on an inner dewar or cold finger encased within a tubular dewar maintained under a vacuum. In the absence of adequate ruggedization, severe environmental vibrations may incite structural resonance responses, which can lead to diminished image quality and potentially induce mechanical failures attributed to material fatigue. Veprik et al. [19] detail their approach for making IDDA more rugged by securing the Focal Plane Array (FPA) or detector to a semi-rigid framework that extends from a damped outer Dewar envelope. By augmenting the total mass of the IDDA by 2%, the researchers have effectively reduced the detector's relative deflection and absolute acceleration by one-third.

Since IDDCA is a critical element for sophisticated infrared systems, particularly

within infrared (IR) applications, it must be highly reliable.

Canxiong Lai et al. [20] conducted a comprehensive examination of the failure mechanisms associated with IDDCA, identifying issues such as vacuum integrity failures, diode degradation, interconnect malfunctions, working medium leakage, spring fractures, mechanical wear, and contamination, all grounded in their reliability physics framework. They have determined that the predominant contributors to these failures are typically outgassing, process-induced defects, and thermal cycling.

The Integrated Dewar represents a crucial element in the infrared detector and requires a vacuum lifespan of ten years during its functional operation.

Shaohua Yang [21] analysed the key influencing factors and mechanisms of failure due to vacuum duration. Four distinct sets of accelerated life testing were employed. Utilizing the Weibull distribution, the characteristic lifetime for each sample group and activation energy was determined. Vacuum longevity of dewar was forecasted, after extrapolating under standard operational conditions of 25°C, to be 12.7 years, adhering to an acceptable vacuum level.

In real-world implementations, the efficacy of an infrared imaging device is constrained by extraneous thermal emissions originating from optical components as well as emissions from IDCA elements such as Dewar walls and vacuum windows, which are typically maintained at ambient temperature. To enhance the operational capacity of the imager, it is essential to implement corrective measures to mitigate their impact and assess these extraneous fluxes.

Ankur Jain et al. [22] delineate an analytical framework established to quantify parasitic fluxes produced by all the elements of a long-wave infrared imaging system. The proposed model was validated through simulations in ZEMAX optical design software employing the ray tracing technique after analytical calculations conducted in MATLAB.

Based on the research, the authors determined that enhancing the sensitivity of a space-based infrared imaging system necessitates lowering the surface temperature of surfaces within the detector's direct line of sight, thereby reducing thermal emissions. Kim et al. [23] conducted an analytical investigation into the steady-state cooling properties of a cryochamber, in the presence of radiation shields. Cryochamber modelling was done in two sets: in the first configuration, radiation shields were placed

at both the detector and the cold finger segments, and in the alternate configuration, a radiation shield was positioned solely at the detector. A schematic representation of these configurations is illustrated in Figure 1.5 below. An analysis of heat transfer for a cryochamber with a radiation shield was performed. 97% of the heat influx was found to be originating from the cold finger component. The presence of radiation shields at the detector and the cold finger reduced heat transfer by 26% at a pressure of 10⁻⁵ torr and by 12% at 1 torr, relative to the configuration where the radiation shield was solely located at the detector region. Beyond an internal pressure of 10⁻³ torr within the chamber, a marked increase in heat influx is attributed to heat transfer due to convection. The study concluded that it is essential to maintain the internal pressure below 10⁻³ torr and utilize radiation shields to mitigate heat transfer through the cold finger to minimize heat influx.

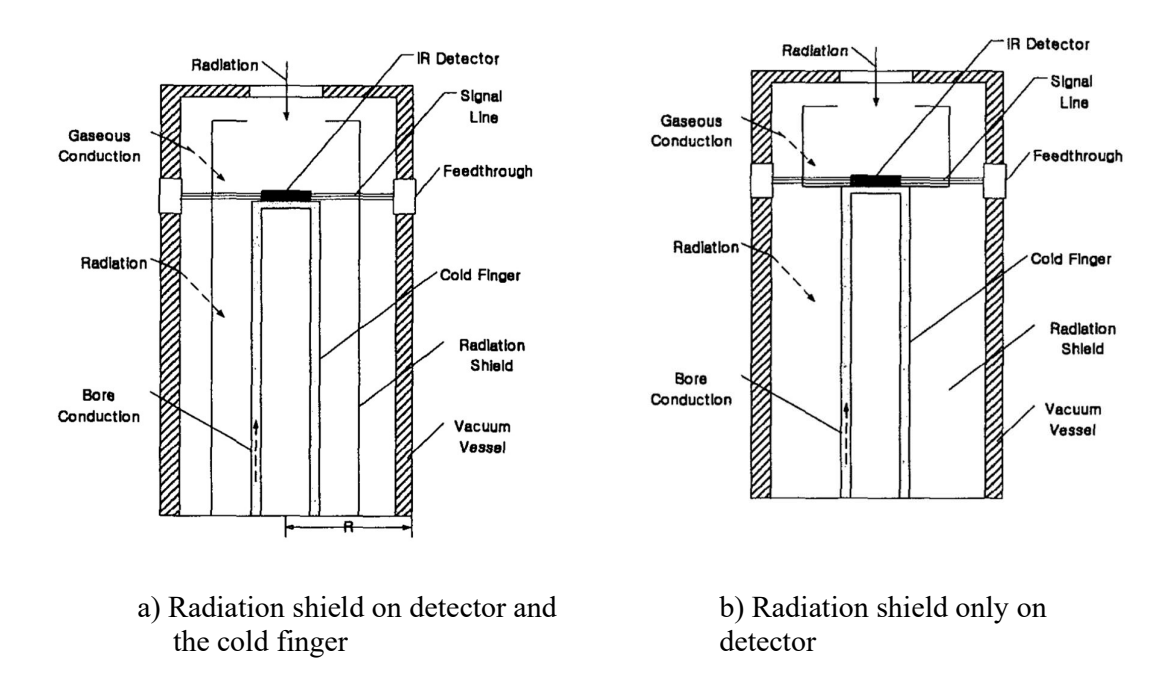


Figure 1.5 Schematic of a cryogenic chamber incorporating a radiation barrier.

Zhang et al. [24] delineated multiple vane designs incorporated in a cold shield for optimizing the suppression of stray radiation. This innovation significantly improved the operational efficacy of infrared systems. A computational tool employed simulated

and examined the influence of vane arrangement on the mitigation of stray radiation. Kang et al. [25] experimentally investigated cooling characteristics of transient nature by manipulating the internal pressure in the cryochamber. A suitable pump was introduced to attain the required level of vacuum. Given a significant gradient in temperature along the bore's cooling region, four temperature-sensing elements were strategically positioned at an interval of 10mm. The infrared sensor was cooled using

liquid nitrogen for optimal performance.

The researchers elucidated the heat transfer characteristics in the transitional state and variations in temperature within the bore by adjusting the chamber pressure from ambient levels to 0.1, 1, and 50 Torr. The vacuum inside the chamber predominantly influenced the cooling down time and influx of heat. It was noted that with chamber pressure falling less than 1 Torr, the temperature characteristics were largely unchanged and exhibited considerable similarity. In contrast, above a pressure threshold of 1 Torr, the cooling duration and heat influx were predominantly governed by natural convection phenomena.

Kim et al. [26] investigated an IR cryochamber having a radiation shield for thermal loads. The design and configuration of the cryochamber or dewar intended for the infrared detector resembles the one in Fig. 1.5 though the radiation shield is not there. The cooling load quantification within the chamber was done with a setup, having a turbo pump for vacuum generation and an injector of liquid nitrogen to facilitate the freezing of the low-temperature region.

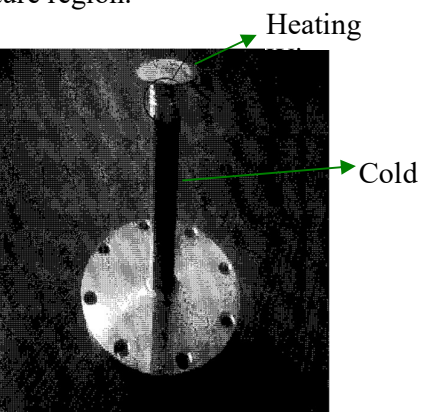


Figure 1.6 Heating wire and cold finger

A silicon diode thermal sensor was engaged to determine the temperature at the frontiers of the low-temperature sector. Moreover, to impose a thermal load on the cold side, a heating wire, as shown in Figure 1.6, was placed around the terminus of the low-temperature zone to enhance heat conduction upon the application of external power. This investigation evaluated the rate of liquid nitrogen evaporation for estimating the heat load on the dewar/cryochamber by filling liquid nitrogen in the cold well till the end where detector to be cooled is placed. The experimentation was carried out under high vacuum conditions to decrease convective heat transfer due to convection. As projected, the findings showed a direct relation between the extent of the thermal load applied and the subsequent rate of liquid nitrogen evaporation. The findings additionally demonstrated that the thermal transfer from the external environment in situations that employed a radiation shield was curtailed by 12.5% relative to scenarios without the application of a radiation shield.

Singhal et al. [27] developed steady-state numerical models intended for the thermal assessment of infrared cryogenic chambers employing MATLAB. The numerical data indicated that the coefficient of gas conduction substantially impacts the temperature distribution within the cryogenic chamber, in contrast to the minimal effect observed for the emissivity. Moreover, the experimental verification of the numerical outcomes is also assessed.

Kim et al. [28] examined the steady-state and transient cooling properties of an infrared cryochamber influencing the thermal load refrigeration mechanism needs to dissipate. The present thermal modelling encompasses the conductive heat transfer through a cold well, the gaseous conduction resulting from outgassing, and the radiation heat transfer. The cooling load in a steady state is established using a fin equation. The transient cooling behaviour, particularly the cool-down duration, is estimated utilizing a finite difference methodology.

Kim et al. [28] investigated the cooling characteristics of an infrared (IR) detector cryochamber under both steady-state and transient conditions, as it significantly influences the overall thermal load that the cooler is required to manage and dissipate efficiently. The thermal model formulated in this context incorporates several critical components, including heat transfer due to the conduction through inner dewar, gaseous conduction due to degassing phenomena, and radiation heat transfer. The

cooling load in the steady state is determined by fin equation, which allows for precise quantification of the heat transfer characteristics under stable operational conditions. Finite difference methodology that facilitates a detailed examination of the time-dependent thermal behaviours of the cryochamber is used for analysing transient behaviour such as determining cool-down phase duration. Research demonstrates that gaseous conduction is integral to the steady-state cooling load, although its effect on the cool-down time is slight as a result of a limited thermal penetration depth. The steady-state cooling load demonstrates a linear enhancement in response to an increase in bore conductivity. Conversely, in situations characterized by low bore conductivity and elevated gas pressure, the cooling load exhibits an increased sensitivity to fluctuations in bore conductivity. The steady-state cooling load exhibits a linear progression in response to the temperature differential between the surrounding and the operating detector; however, the cool-down time is directly related to the square of the temperature differential present during that period. This investigation can shape the thermally optimal architecture and operational parameters of the cryochamber.

Singhal et al. [29] formulated a robust numerical methodology for the thermo-physical analysis of infrared cryochamber dynamics under transient scenarios, which represent the most critical conditions while incorporating all pertinent thermal loads, including heat load due to radiation in its unaltered state. The proposed code scores over preavailable commercial software options such as ANSYS, COMSOL, etc in its proficiency to simultaneously address gas conduction alongside radiation components, utilizing widely accessible software like MATLAB. The developed codes were subsequently subjected to experimental validation, revealing that the observed cooling behaviors closely matched the predictions derived from the established model.

Mayuri et al. [30] undertook the development of a computational framework capable of hypothesizing the thermal characteristics of the Integrated Dewar Detector Cooling Assembly (IDDCA) along with their interrelationships. The investigation was conducted utilizing the heat transfer and ray optics modules available within the COMSOL environment for the assembly.

Raab et al. [31] developed, constructed, and evaluated an engineering prototype of the Integrated Detector Cooler Assembly (IDCA) intended for application in extraterrestrial instruments. The manufactured dewar assembly comprised four

essential components: the dewar, a 640×480 -pixel InSb focal plane, a long-lasting flexure bearing compressor, and a pulse tube cold finger. The IDCA and micro cooler were assessed for their thermal performance to ascertain the operational range of the system for compatibility with a diverse array of SWIR and MWIR focal planes.

The process of isothermal calorimetry involving Dewar-Detector Assemblies (DDA) constitutes a standard component of the Acceptance Testing Protocol. In this scientific methodology, the cryogenic liquid coolant, conventionally liquid nitrogen (LN₂) is permitted to evaporate naturally from the Dewar receptacle into the atmosphere via a mass flow meter; thereafter, the parasitic heat load is assessed as the product of the latent heat of vaporization and the rate of boil-off linked to the 'last drop.'

A fundamental and significant constraint of this methodology lies in its application solely at the specific boiling point of the selected liquid coolant. Additionally, an associated drawback pertains to the volatile characteristics of "last drop" boiling, which results in a fluctuating flow rate. This phenomenon is particularly relevant for sophisticated High Operational Temperature Dewar-Detector Assemblies, which are generally equipped with short cold fingers and operate at temperatures of 150 K and higher.

A Veprik et al. [32] advanced the existing methodology of dual-slope calorimetry and indicated that precise determinations of heat load can be accomplished by comparing the slopes obtained from thermal transients during warming trials along with additional heat loads. Due to its simplicity, precision, and capacity to conduct calorimetry at virtually any desired temperature, this approach exhibits considerable promise as a viable alternative to boil-off calorimetry.

Boffito et al. [33] examined the methodologies for achieving and sustaining the vacuum essential for optimizing thermal insulation within a cryogenic chamber. Specifically, the properties and applications of specialized non-evaporable getters, along with their sorptive behaviour, were analysed. The authors articulated that a vacuum serves as an optimal thermal insulator due to the minimization of molecular thermal conductivity. Moreover, enhancements in reducing thermal losses are frequently achieved through the implementation of reflective barriers (e.g., aluminium foils, interspersed with thin insulating materials such as fiberglass sheets) to mitigate another contributor to insulation loss, namely radiation. Additional losses are

contingent upon contact points and, consequently, the specific design of the cryogenic chamber. To preserve the vacuum throughout its operational lifespan, which can be compromised not only by outgassing but also by minute leaks that are challenging to detect, sorptive agents, or getters, are incorporated into the evacuated enclosure. These getters predominantly rely on physical adsorption (for instance, zeolites), although some function through the chemical transformation of gases (primarily hydrogen, as exemplified by the use of PdO). The attributes of "chemical adsorbers," specifically the non-evaporable getters, have been scrutinized in this context, taking into account other significant objectives for using getters: to facilitate in situ pump out that aids in enhancing and expediting the baking process duration.

1.2.3 Studies on cryocooling technologies for Infrared detector cryochamber

Cryogenic microcoolers are employed in a variety of electronic apparatuses, including superconducting devices, low-noise amplifiers, and optical detectors as these components require low thermal conditions to mitigate thermal noise. Photon detectors necessitate cooling to temperatures as low as 77K or even lower for optimal performance.

Glaister et al. [34] undertook a meticulous survey that revealed more than 30 reliable cooling systems applicable to space, encompassing various thermodynamic cycles and setups. Identified refrigeration systems display capabilities fluctuating from several milliwatts to exceeding 10 W, operating within temperatures as low as 10 K to beyond 120 K, and having configuration of both single and multi-stage type.

Wiecek [35] examined three primary cooling mechanisms, namely Stirling coolers, thermoelectric coolers, and JT coolers, which are utilized in infrared detectors. They remarked that thermoelectric coolers aid in the cooling of the detector with a relatively low level of efficiency and do not reach exceedingly low temperatures.

Wiatr et al [36] proposed a methodology for the co-simulation of circuits and electromagnetic (EM) fields to model the electrical properties of interconnects employed in thermoelectrically cooled infrared photodetectors. Thermoelectric coolers exhibit no vibrational production, thus making them fit for thermal detectors; however, the microphone effect could potentially detrimentally affect their operational performance.

Bhatia et al. [37] engineered a specialized cryogenic system that functions

independently of consumable liquid cryogens. The system has a three-stage cryocooler integrated with a cooler of three-stage sorption type to attain a low base temperature of 239 mK. This system has been harnessed for the thermal supervision of the detectors and optical components on the Polatron instrument, a terrestrial receiver implemented at a 5.5-meter telescope, focused on observing the 2.7 K cosmic microwave background.

Stirling Cryocoolers and Joule-Thomson (J-T) cycle-based cryocoolers are used to achieve cryogenic temperatures and for thermal regulation of infrared detectors.

J-T coolers exhibit greater operational simplicity compared to alternative cooling methodologies, as they facilitate a more rapid cooling process and are devoid of mechanical components. Applications encompassing infrared (IR) sensors [38], space exploration [39], cryosurgical procedures and cryopreservation [40, 41], superconductivity [42], as well as liquefaction systems [43, 44], represent domains in which J-T coolers are extensively implemented.

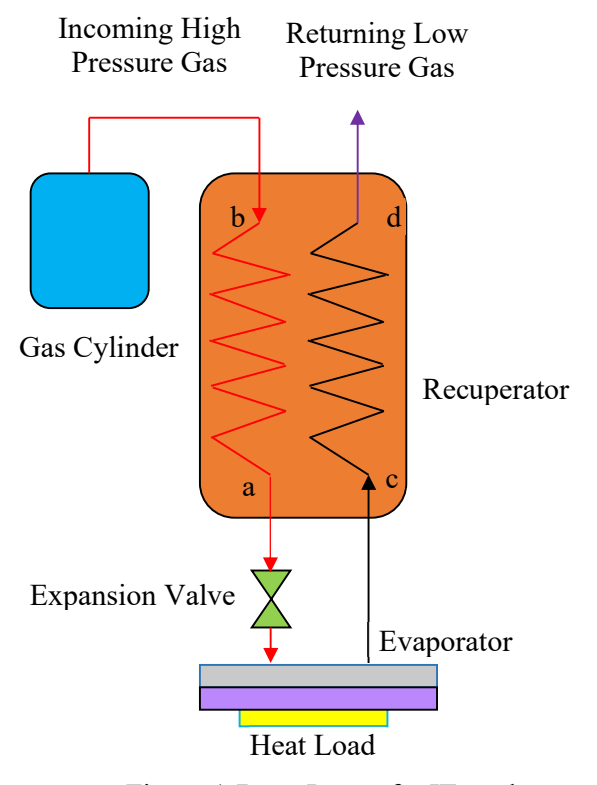


Figure 1.7 Parts of a JT cooler

The working fluid employed in J-T cryocoolers is generally Argon or Nitrogen gas, due to reasonable price and ease of availability. The principal components of a Joule Thomson cryocooler include a gas bottle for high-pressure working fluid, a recuperative heat exchanger, an expansion valve or orifice, and an evaporator or detector load. The complete configuration is shown in Figure 1.7. The pressurised gas from the storage container passes through the heat exchanger and undergoes expansion through the micro orifice or expansion valve experiencing cooling due to the J-T effect. The cooling phenomenon is realized within the evaporator or at the orifice end, after which the gas crosses the part of the heat exchanger which is at lower pressure. This low-pressure gas plays a crucial role in the cooling of the incoming gas at high pressure before discharging into the atmosphere. The configuration ends in a heat exchanger characterized as a recuperative type of heat exchanger. Such a heat exchanger involves a transfer of heat from incoming high-pressure gas at a higher temperature to the returning gas at a lower pressure and temperature, thereby cooling the entering highpressure fluid. The effectiveness of such a heat exchanger affects the efficiency of the Joule Thomson cryocooler.

In the absence of a recuperative type of heat exchanger, very high pressures are required for the liquefication of nitrogen [45]. Flynn [46] highlighted that a 90% effective heat exchanger does not liquefy nitrogen within a cycle functioning under pressure ranging from 1 bar to as high as 100 bar. An increase in heat exchanger effectiveness to about 97% is necessary. The recuperative heat exchanger is acknowledged as the most critical element of a Stirling cryocooler and has undergone comprehensive analysis by a multitude of researchers. Xue et al. [47] along with Ng et al. [48] engaged in steady-state studies of a miniature recuperative heat exchanger that employs argon as a working fluid, and have validated the conclusions experimentally.

Chua et al. [49] included a comprehensive geometric formulation of the finned capillary tube within the steady-state thermal analysis of the recuperative heat exchanger. Hong et al. [50] used the Number of Transfer Units (NTU) method to estimate the heat exchanger effectiveness under pressures as high as 500 bar while using Nitrogen and Argon.

Ardhapukar and Atrey [51] undertook a steady-state study designed to improve the

functional performance of a miniature cryocooler based on the Joule-Thomson cycle. Another study by Chou et al. [52] on a miniature J-T cryocooler presented a numerical investigation of transient characteristics augmented with empirical results. Chien et al. [53] proposed a comparable model for transient case that integrated a bellows mechanism for self-regulation into the framework delineated by Chou et al., aimed at regulating the flow rate of working fluid on liquefication.

Hong et al. [54] performed experiments to analyse the transient cooling dynamics of a miniature Joule-Thomson cryocooler operating with nitrogen as a working fluid with inlet pressures of 120 bar. Furthermore, Hong et al. [55] numerically assessed the operational dynamics of a refrigerator based on the Joule-Thomson cycle.

Extensive analyses have been reported, addressing the implementation of extra ejectors within the JT cycle framework and their exergy analysis [56], the optimization of operational fluids [57], the cooling dynamics linked to the JT effect, as well as aspects of finite reservoir capacity [58].

Comprehensive numerical assessments of clogging dynamics [59] and the impact of moisture on clogging sensitivity [60] have also been carried out for the Joule-Thomson cycle-based cryocooler.

Cryocoolers of pulse tube and Stirling type represent alternative cooling solutions for infrared detectors [61-65]. The pulse tube cryocooler (PTC) is distinguished by its remarkable reliability and capability to attain enhanced thermal efficiency, establishing it as a feasible alternative. However, even though pulse tube cryocoolers are envisaged for the refrigeration of infrared detectors in numerous space applications, they do manifest certain constraints. A significant constraint is the obstacle of miniaturization to scales as small as 0.15 W at 80 K while preserving high efficiency. A supplementary impediment consists of the increased diameter of the cold finger necessary to achieve equivalent refrigeration efficacy owing to the presence of the pulse tube. These two barriers have restricted their implementation in cooling infrared sensors for several military tactical initiatives [67].

Miniature Stirling cryocoolers, recognized for their size efficiency, operational effectiveness, and reduced weight, can effectively reach cryogenic temperatures appropriate for infrared detection [68-70]. The Stirling Cryocooler, as shown in Figure 1.8, comprises principal components including the piston-driven compressor, the

aftercooler, the transfer line for conveying working fluid, the hot heat exchanger for thermal exchange at high temperatures, the regenerator or displacer, and the cold heat exchanger, where only regenerator and piston exhibits motion.

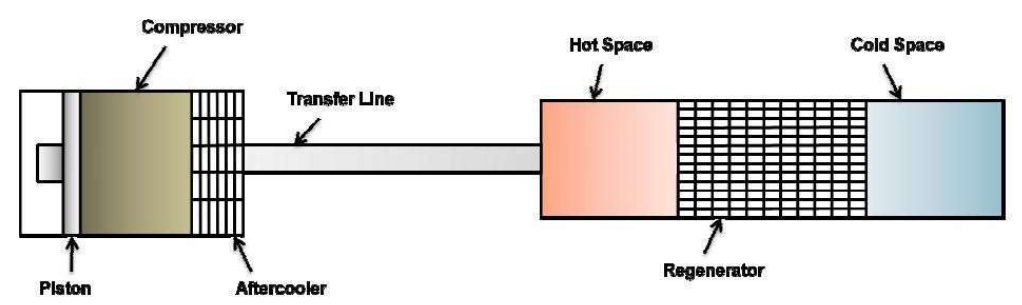


Figure 1.8 Schematic representation of Stirling cryocooler

A conventional Stirling cryocooler is comprised of two components that undergo periodic motion: a displacer and a piston, which are engineered to operate with a specific phase angle of displacement. A predetermined quantity of working gas is hermetically sealed within the apparatus, thereby establishing a closed refrigeration cycle. The piston, driven by an electrical motor, induces cyclic compression and expansion of the working gas, while the displacer facilitates its oscillation. Moreover, the regenerator serves as a critical heat exchanger, strategically located between the hot and cold extremities to promote efficient heat transfer within the working gas flow. Following the emergence of the Stirling engine of free-piston type in the early 1960s, alongside Philips Laboratories' development of the free-piston Stirling cryocooler (FPSC) [71], a series of significant advancements subsequently took place with the emergence of the split-Stirling cryocooler [72] engineered to achieve a considerable reduction in cold-tip vibrations and the Oxford split-stirling cryocoolers [73] with their enhanced operational lifespan. Furthermore, novel designs proposed include the duplex Stirling refrigerator [74-75], the Stirling refrigerator with liquid piston [76], and the diaphragm Free Piston Stirling Cryocooler (FPSC) [77].

The operational effectiveness of a Stirling cryocooler is influenced by several variables, such as the type of working fluid, and the performance of heat exchangers, in addition to the volume, pressure, and ratios of temperature, velocity, and phase angle [78].

Thermodynamic models based on theoretical assumptions regarding the functionality

of Stirling machines have been extensively recorded in the academic literature. Schmidt's analysis marked the inaugural performance analysis of the Stirling machine, which has since proven beneficial for design considerations [79]. Xu et al. [80] engineered a high-capacity cooling Stirling cryocooler of 700 W and studied the effect on cooling capacity with a change in frequency and charging pressure.

In space applications aimed at cooling infrared sensors, Bhojwani et al. [81] designed and assessed a two-stage Stirling cryocooler providing 2 KW and 1/2 W of cooling capacity at cryo temperatures of 120 K and 60 K respectively. Singh et al. [82] fabricated prototypes for the Stirling cooler and investigated the amalgamation of the cooler with thermal sight systems. They indicated that electromagnetic interference and the occurrence of vibrations constitute the fundamental shortcomings related to such devices. To evaluate the energy conversion attributes of basic components and their effect on the cooling system efficiency, the energy dynamics of the cryocooler were examined by applying the relevant Sage model developed by researchers Cai et al. [83].

After a seminal investigation conducted by Curzon and Ahlborn [84] regarding the Carnot direct cycle characterized by finite heat transfer, a diverse spectrum of thermodynamic models have been documented, employing finite time and finite speed thermodynamics (FTT & FST), [85,86], and finite physical dimensions thermodynamics (FPDT) [87,88].

Numerous investigations have been conducted on the regenerator of the Stirling cooler, with various studies focusing on its modeling as a porous medium. To evaluate the pressure drop associated with a steady-periodic (lateral and axial) flow of helium through wire mesh regenerators, Cha et al. [89] conducted empirical investigations. To ascertain the coefficients of the porous medium, Costa et al. [90] proposed a non-thermal equilibrium modeling approach based on the finite volume method (FVM), which effectively describes fluid dynamics and thermal transfer in a conventional small-scale flow domain of the woven wire matrix. The findings of Srinivasan et al. [91] regarding a cryocooler's regenerator, which is formed from porous sintered material, indicated that maximum system efficiency is attained at an optimal porosity of 69.62%. In his research, Boer [92] performed a one-dimensional evaluation of regenerative heat exchangers utilizing the relationship between the Stanton number,

St, and the Fanning friction factor, f, to investigate thermal and dissipative losses. The analysis revealed that maximum operational efficiency is obtained when there is a considerable proportion between the volume of the heated environment and the void volume of the regenerator.

The thermal transport dynamics and hydrodynamics of regenerators with assorted geometric and material properties were assessed by Tao et al. [93]. Zhao et al. [94] constructed a two-dimensional axisymmetric computational fluid dynamics (CFD) model of a compact Stirling-type pulse tube cryocooler, which incorporates both non-thermal and thermal equilibrium paradigms for the porous matrix to analyze different regenerator losses.

The contribution of several parameters to the cooling effectiveness of a Stirling cryocooler was subsequently assessed [95]. The study showed that the chief work loss was derived from mechanical friction, whereas the largest heat loss was linked to conduction.

1.2.4 Origin of Research Problem

The inferences drawn from the comprehensive literature survey are enunciated as follows:

- Many studies have been conducted concerning infrared detector assemblies and their viable applications in commercial industry and defense.
- The studies highlight the need for low-temperature operation of these detector assemblies for optimum performance by maximizing their quantum efficiencies.
- The essentiality of temperature operation coupled with low pressure to minimize heat loads brings an interplay of thermal and thermo-physical aspects into play due to the introduction of a cold finger, cryochamber assemblies, and evacuation to vacuum conditions.
- Several studies have been devoted to studying the thermo-physical aspects including modes of failure analysis and evaluating possible lifetimes under various operating conditions.

- Few studies have been carried out regarding thermal analysis for steady and transient operational scenarios and model development for the same has been explored.
- A further pertinent dimension that has garnered scholarly interest is the
 exploration of diverse cryocooling techniques, encompassing
 Thermoelectric, Stirling, and Joule-Thomson (J-T) coolers. An array of
 research undertakings has been conducted to assess these cooling
 methodologies' performance characteristics and the factors that affect their
 efficacy.

The prime **limitations** of the work carried out to date, which form the basis for defining the objectives of the present work are discussed as under:

- Most studies carried out are isolated studies of either the infrared detectors or thermal and thermo-mechanical aspects of cryochamber or cryocoolers. No integrated studies amalgamating all three together have been presented.
- Even regarding numerical models for thermal analysis, basic configurations
 have only been investigated and complex scenarios incorporating radiation
 shields or getters have not been investigated in sufficient details.
- Further, experimental validation of various developed algorithms for even basic configurations and more so for complex scenarios in a comprehensive manner requires significant further studies, and corresponding analysis, which may also consider application scenarios.
- As far as aspects related to cryocooling techniques are concerned, specific studies experimentally proving their efficacy including parametric investigations specifically for complex J-T coolers and Stirling in direct application environments are yet to be carried out.

1.2.5 Objective of the Research Work

- Thermal analysis of cryochamber assemblies in applicable scenarios.
- Investigation of thermal design aspects of cryocoolers with specific emphasis on Joule-Thomson and Stirling cryocoolers and their influencing parameters.

- Empirical investigations concerning cryochamber and cryocooler configurations, focusing on the validation of models and the assessment of their effectiveness.
- Parametric experimental studies in the integrated scenario of an infrared detector operating with cryochamber assemblies and cryocoolers.

1.2.6 Brief Research Methodology

The research methodology after the detailed literature survey already carried out will involve identifying the conditions of various practical operation scenarios of integrated infrared detector assemblies. Subsequently, a thermal analysis that may include analytical integral solutions, computational thermal modelling, and influencing mechanical aspects will be taken up suitable for most conservative conditions. It will be followed by developing each assembly viz., cryochamber, and cryocooler based on their design and independent testing of the same and corresponding parametric studies. These will then be integrated and tested comprehensively under different operating conditions and possible mutual influences and interdependencies identified experimentally.

1.2.7 Expected Outcome of Proposed Research Work

- Realization of cryochamber assemblies based on thermal design, analysis, and models developed.
- Realization of cryocoolers with specific emphasis on J-T and Stirling cryocoolers based on thermal design, analysis, and models developed.
- Experimental investigation of cryochamber assemblies and cryocoolers and evaluating their performances due to varying major influencing parameters.
- Parametric experimental studies in the integrated scenario of an infrared detector operating with cryochamber assemblies and cryocoolers and identifying suitable parameters for integrated operations.

DESIGN ASPECTS OF IR CRYOCHAMBER

Cryochambers, also known as Dewars (after their inventor, Sir James Dewar), are double-walled evacuated containers that often achieve high vacuum levels (below 1 x 10^-6 torr). This vacuum is a highly efficient thermal insulator against ambient temperature and ensures a contaminant-free environment. The parameters for the design of a cryochamber are primarily dictated by the applications intended. The function of the cryochamber or Dewar is crucial for providing appropriate conditions for liquefied cryogenic substances or ensuring the optimal functionality of the housed detector.

This chapter investigates and expounds upon the key considerations integral to the design of an infrared (IR) cryochamber, including its components, to elucidate their specific roles in supporting the optimal functionality of IR detectors.

2.1 IR Cryochambers or Dewars

In the sphere of cryochambers tailored for devices like infrared detectors, the design assumes heightened importance. Similar to other cryochambers, the maintenance of a vacuum is essential for preserving a contamination-free environment for the sensitive components located within the infrared cryochamber. The advancement of rapid cooldown cryogenic infrared systems is anticipated to depend on lightweight, compact, and cost-effective designs that employ cutting-edge configurations, materials, and mass-production manufacturing methodologies. An optimized miniature infrared cryochamber, integrated with both the detector and cryocooler, is particularly advantageous for applications necessitating prolonged storage durations (10-15 years), rapid cool-down intervals (30-60 seconds), and brief operational missions (< 3 minutes). The predominant applications for such cryochambers include cooled seekers in missiles, projectiles, or "smart" munitions. In these scenarios, the environmental parameters, including temperature, acceleration, shock, and vibration, are extreme, necessitating the minimization of volume, weight, and overall expenses.

The all-glass cryogenic chambers/dewars, conventionally supplied with liquid nitrogen, were previously utilized for experimental purposes in laboratories and were deemed ineffective for alternative applications.

Conversely, an infrared detector cryogenic chamber/dewar may be composed entirely of glass, entirely of metal, or a hybrid of both materials. Such tactical dewars, employed in military operations, require a design that is both compact and robust, facilitating ease of transport while minimizing thermal load and physical mass.

2.1.1 Rapid Cool-down Dewars

All cooled components must exhibit minimal mass, low specific heat capacity, elevated thermal conductivity, adequate heat transfer surface area, shortened thermal pathways, and, ultimately, a high thermal diffusivity to fulfill the criteria for rapid cooling. To mitigate heat influx from the surrounding environment on the cooled components, it is imperative to appropriately design or insulate the thermal pathways leading to components at ambient temperature. Neglecting these essential considerations will inevitably lead to an increased demand for cooling, coolant supply, and extended cooling durations. All thermal parameters must be meticulously evaluated for the device to operate effectively.

A conventional rapid cooling Dewar assembly is required to comprise a focal plane array (FPA) detector assembly, cold shield, and dewar well structure housing the cooler, windows, and outer casing, as illustrated in Figure 2.1.

The dewar well (a cold finger or cold stem) acts as a cantilever and thermally isolates the FPA and cold shield within the housing. It provides essential support and alignment for the FPA, ensuring optical integrity under environmental shock, vibration, and acceleration. Moreover, the dewar well accommodates the JT cryo-cooler and its exhaust gases upon activation. Typically, it consists of a thin-walled tube and a 'cold end' plate aimed at minimizing thermal conduction from the warm end, usually constructed from a low thermal conductivity, high-strength material. Conversely, the cold end plate is fabricated from a high thermal conductivity material that closely aligns with the coefficient of thermal expansion of the cold finger tube and the FPA base material. Historically, dewar wells were constructed from borosilicate glass; however, contemporary designs favour metal tubing of austenitic stainless steel, Fe-Ni (Invar), or Ni-Co (Kovar) alloys, alongside invar or alumina endplates (comprising either polycrystalline or mono-crystalline alumina, sapphire, for enhanced thermal conductivity). Innovations in metalizing ceramics and furnace brazing of ceramics to

metals have facilitated these design advancements. The diameter of the dewar well is typically calibrated to ensure that the attachment surface area of the FPA and cold shield to the endplate is fully wetted with refrigerant. The nearest cooler size is subsequently selected accordingly. Consequently, a specified dewar well diameter and length must be thermally optimized and structurally robust to withstand the anticipated vibration, shock, or acceleration forces.

This chapter discusses the design features of an infrared (IR) accentuating their significant role in realizing the intended operational capabilities of the IR detector.

2.2 Details for Cryochamber Design

The fundamental details necessary for establishing the specifications of a cryochamber are listed below:

- 1. Required thermal load capacity
- 2. Required Operational temperatures
- 3. Cryochamber Material
- 4. Specifications of bond wires
- 5. Dimensions of the inner dewar's bore and length
- 6. Diameter of the cryogenic chamber
- 7. Specifications regarding the window type, cold filter or shield
- 8. Dewar degassing through thermal baking
- 9. Implementation of dewar pinch-off for sealing
- 10. Classification of materials for getter
- 11. Temporal parameters such as duration of cool-down and hold-on for the cryogenic chamber.
- 12. Selection of appropriate cryocooler
- 13. Structural design considerations for mechanical strength
- 14. Assessment of mechanical integrity and robustness of the cryogenic chamber

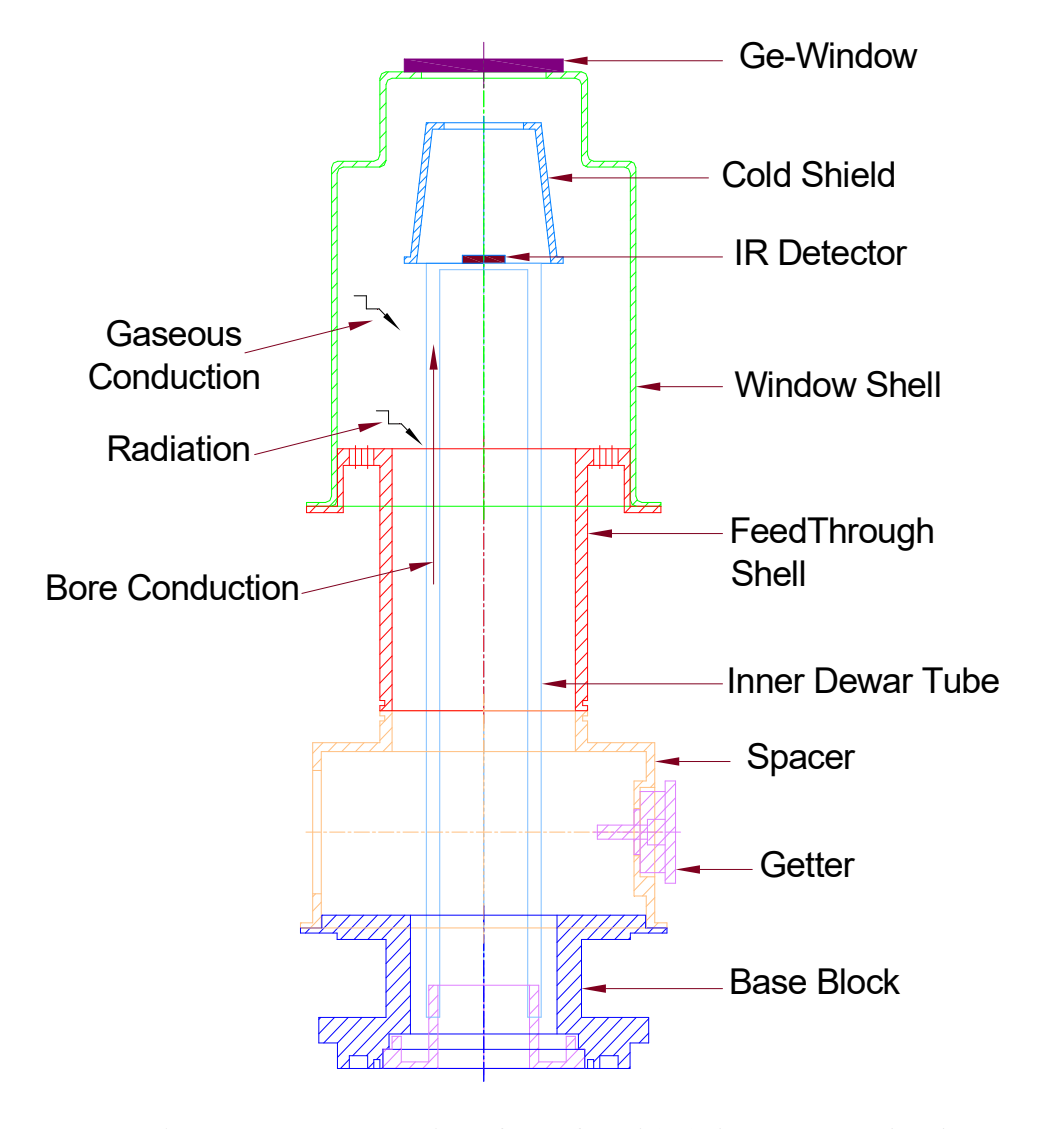


Figure 2.1 Section of an Infrared (IR) dewar or cryochamber

2.2.1 Required Thermal Load Capacity

For estimating the thermal load within a cryochamber, the following key factors as illustrated by Figure 2.1 are considered:

- i) Conduction due to inner dewar tube
- ii) Conduction occurring in connecting wires
- iii) Gas conduction resulting due to low pressures alongside gas convection due to vacuum degradation in the cryochamber
- iv) Thermal load due to radiation on inner dewar tube

- v) Thermal radiation falling on the detector through the IR window
- vi) Radiation of heat by metallic dewar parts
- vii) Production of Heat on operating the detector

2.2.1(a) Estimation of Thermal Mass & Heat Load of Dewar

Dewar design must effectively reduce the overall thermal mass and the steady-state heat load for rapid cooldown. Thermal mass is the initial heat load cooler eliminates to attain the targeted low temperature. Once this initial heat load from the detector dewar system is removed, indicative of the establishment of a cool-down state, the detector will exhibit a warming trend at a rate directly proportional to the system's steady-state heat load. Consequently, at this juncture, the cooler must possess sufficient refrigeration capacity to extract heat at the rate corresponding to the steady-state heat load of the Dewar at the desired cold temperature. The cryocooler integrated into the cold finger of the cryochamber, as illustrated in Figure 2.1 cools the detector. The feedthrough unit, responsible for transmitting the electronic signals from the detector to the external circuit, is generally installed at the assembly base or the detector level. In the latter scenario, electrical connections can be established through wire bonding.

The following aspects are taken into consideration while estimating the heat load of dewar:

- a. Thermal conduction through cold-finger,
- b. Thermal conduction due to conductor leads joining header to feedthrough pads
- c. Thermal radiation from an external surface of dewar & through IR window
- d. Gaseous conduction can be neglected if a high vacuum is maintained and
- e. Electrical heat load of the Detector, while it is operational.

The approximate contribution of the above factors in the heat load of the dewar is as follows:

a. Thermal conduction from Dewar cold finger = 65%

b. Thermal conduction through leads = 15%

c. Thermal radiation through walls & window = 20%

Thus, Total Steady State Heat Load of Dewar (w/o device load) =100%

Similarly, the various components of the detector /dewar system and their estimated contributions to the **Thermal mass** are as follows:

a.	Detector Cold Shield	=	30%
b.	Dewar Cold Finger	=	30%
c.	Detector Platform	=	32%
d.	Detector	=	7%
e.	Mounting Adhesive	=	0.5%
f.	Thermal Cable	=	0.5%
	TOTAL JOULE MASS	=	100%
	1011L JOULE MILES		100/0

2.2.2 Required Operational Temperatures

Dewar or infrared cryochamber is typically designed to function within a temperature range of -40°C, for instance, in regions characterized by snow-covered terrain, to +70°C, for example, in arid desert environments. Elevated temperature may result from the thermal conditions of the vehicle or the external atmospheric temperature of the surroundings.

2.2.3 Cryochamber Material

Metallic cryochambers or dewars are typically constructed from Kovar, stainless steel, or Inconel. Nonetheless, in the case of cryochambers that incorporate both glass and metal, 'Kovar' alloy and 'Kovar-matching glass' are employed due to their closely aligned coefficients of thermal expansion. Kovar is an iron-based alloy consisting of approximately 54% iron, 29% Nickel, and 17% Cobalt.

Low thermal conductivity is a significant characteristic of Kovar which is approximately 23 times less than copper at a similar temperature and closely aligns with the thermal conductivity of stainless steel. Additionally, it is ductile, thereby facilitating ease of deep drawing.

2.2.4 Specifications of Bond Wires

The specifications of the wire used for connecting the device mounted inside the dewar to multi-pin feed-through for external connections significantly influence the thermal load experienced by the dewar. For minimising the heat load of the cryochamber, wires of 1 mil diameter of a very low thermal conductivity material (such as 10% Iridium

Platinum) are used, which are bonded or welded at the opposite pads of the feedthrough and the detector carrier as shown in Fig 2.2.

As illustrated in Figure 2.2, a device affixed to a detector carrier is connected to an external suitable multipin feedthrough using wires of thin geometry and low thermal conductivity. The material of LTCC (Low-Temperature Co-fired Ceramic) feedthrough is composed of glass and alumina, which renders it brittle and provides inferior vacuum integrity relative to HTCC (High-Temperature Co-fired Ceramic) materials which consists of 92% alumina.

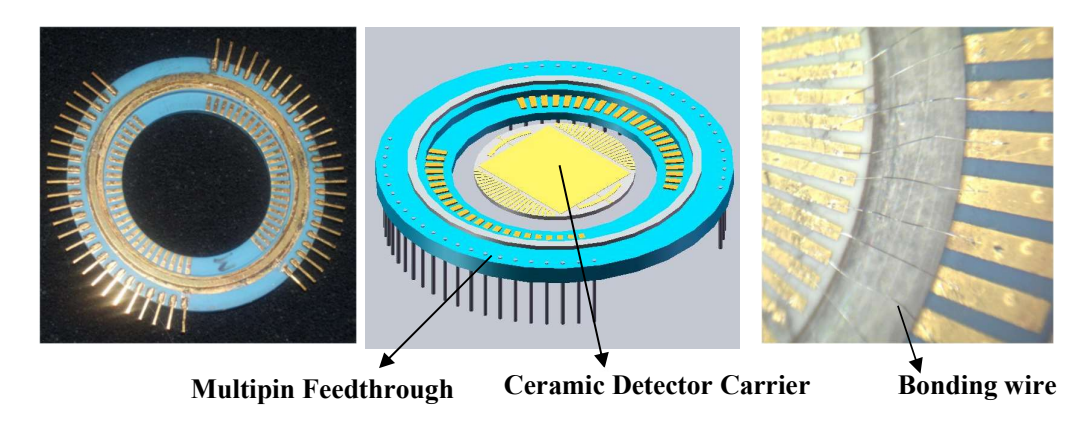


Figure 2.2 Multipin feedthrough bonding to detector carrier with thin wire

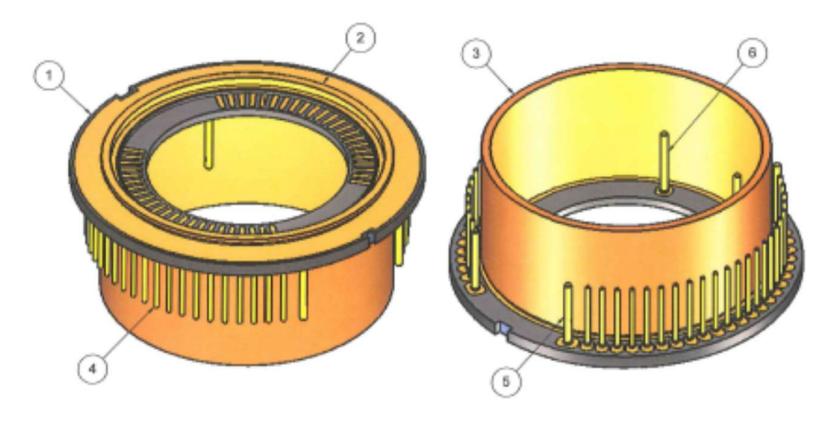


Figure 2.3 HTCC Feedthrough

Furthermore, given that the HTCC (High-Temperature Co-fired Ceramics) feed-throughs undergo firing at significantly elevated temperatures around 1600°C, they exhibit reduced porosity more appropriate for utilization in high vacuum dewars. In

this context, the upper and lower metallic rings are also brazed to the main body eliminating additional integration issues with the dewar structure through soldering. In this scenario, the metallic rings may be elongated, resembling cylindrical shells, which can also be brazed to the dewar body. Consequently, for all these considerations, the HTCC feedthrough shown in Figure 2.3 has certain advantages over the LTCC feedthrough.

2.2.5 Dimensions of the Inner Dewar's bore and length

The method of achieving cryogenic temperature significantly impacts the specifications of the dewar apparatus. When utilizing Joule Thompson (JT) cooling, there are stringent tolerance requirements concerning the inner dewar's bore; specifically, the bore must be maintained within $\pm 10\mu m$, and the tube length should not surpass 3mm of the cooler's finned length. Likewise, for the Stirling cooler, tolerances applied to the cold finger are comparably rigorous.

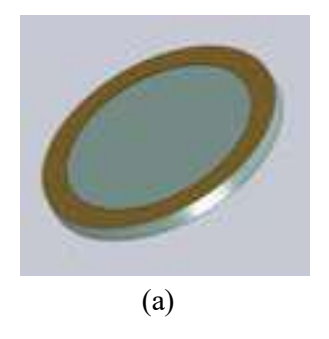
2.2.6 Diameter of cryogenic chamber

The outer diameter of the cryochamber is selected based on the spatial constraints of the installation site and to ensure adequate vacuum insulation for the inner cryochamber surface.

2.2.7 Specifications regarding the window type, Cold Filter, or shield

The "aperture" depicted in Figure 2.4 (a) serves as a radiation filter that permits only those radiations within the specified wavelength range to enter the cryochamber. For instance, the wavelength interval of 8-14µm is typically deemed suitable for infrared (IR) devices. Consequently, a Germanium filter window is utilized, permitting only wavelengths of the desired infrared range to traverse. An anti-reflective coating enhances its performance, potentially increasing transmission rates close to 95%. The window size depends on the dewar dimensions and must have sufficient strength to endure vacuum pressure.

A germanium cold filter (see Figure 2.4 (b)) and a cold shield diminish the background.



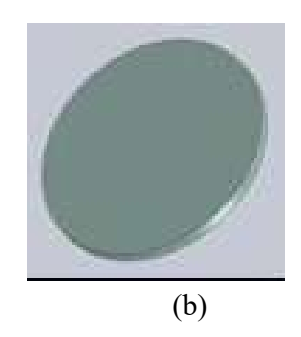


Figure 2.4 (a) Metalized Germanium Window (\$\phi\$ 15mm) & (b) Cold-Filter (\$\phi\$ 12mm)

An appropriate cold shield, either conical or baffled in design, as depicted in Figure 2.5 below, is essential. This shield encircles the apparatus, functioning as a radiation barrier while being thermally regulated in tandem with the detector. A filter positioned atop the cold shield termed a cold filter gets cooled enhancing its filtration efficacy due to the lower operational temperature. The conical configuration of the cold shield effectively establishes an optimal "Field of View" for the detector.

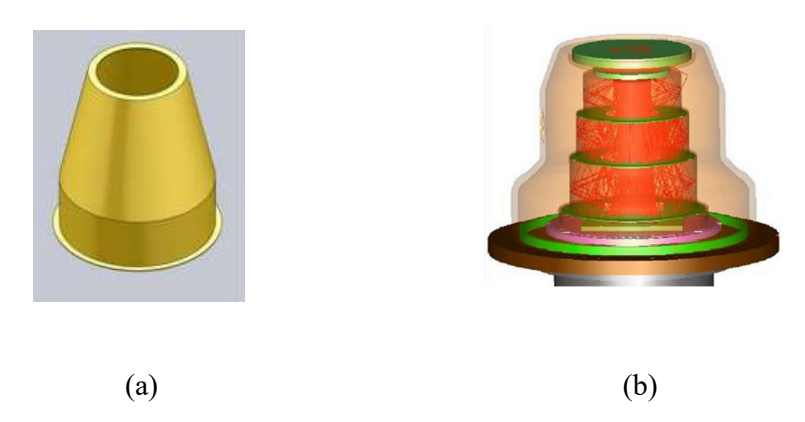


Figure 2.5 Cold Shield (a) Conical & (b) Baffled type

2.2.8 Dewar degassing through thermal baking

The dewar must undergo a degassing procedure before its ultimate sealing from the pump. This degassing operation is performed utilizing a dedicated degassing apparatus.

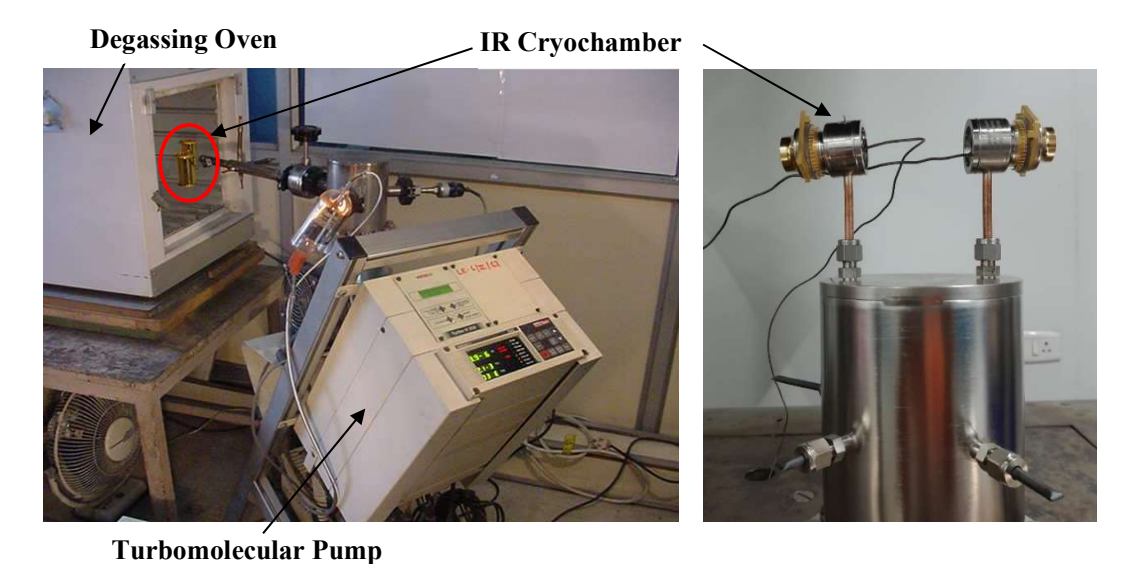


Figure 2.6 Cryochamber degassing station

The components of a dewar typically adsorb gaseous molecules on their surfaces, necessitating their removal before the sealing. The release of gases trapped within the material termed out-gassing happens when subjected to an ultra-high vacuum and is dependent upon the dewar surface temperature, duration of vacuum exposure, and the gas properties involved. This procedure is termed baking, since the temperature may go as high as 400°C.

Nevertheless, operational constraints decide the upper-temperature limit; for a cryochamber designed for infrared devices, the temperature cannot exceed 65 to 70°C due to the detector's thermal tolerance. Figure 2.6 illustrates the baking process. The baking process can continue for several hours extending to several days, with the discussed dewars requiring approximately 7 to 8 days of continuous operation without interruption.

2.2.9 Implementation of dewar pinch-off for sealing

Dewar pinch-off or sealing is performed at ultra-high pressure of 1×10^{-9} mbar on completing a long evacuation process or degassing at a specific temperature that continues for 7 to 8 days. When the material for both the external dewar shell and evacuation tube is glass, the sealing is done by a flame torch. The temperature produced by the torch induces the melting of the glass, thereby affecting the complete sealing of the dewar from the vacuum pump.







a) Flame torch method

b) Cold weld method

Figure 2.7 Methods for Sealing a Cryochamber

Nonetheless, where the external casing of the dewar is composed of a metallic material, it is customary to employ OFHC (oxygen-free high conductivity) copper tubing for evacuation. The sealing in such cases can be done manually or by a hydraulic tool, as shown in Fig. 2.7 (b). The oxygen free soft copper tube is first flattened by the semi-cylindrical jaws of the pinch-off tool and on further applying the pressure the tool cuts the tube in two portions, sealing both ends, one is retained with the pumping system and the other portion becomes the part of the Dewar.

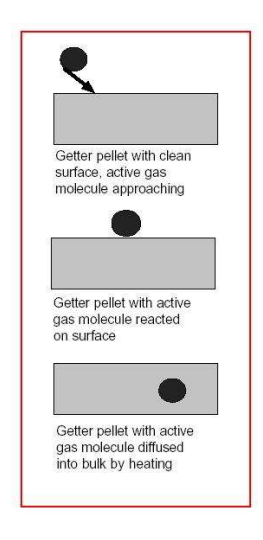
The sealing methodologies employed are illustrated in Figure 2.7 above. The minimal oxygen content (below 10ppm) in the OFHC copper tubing facilitates an optimal cold weld of the tubing during the pinching-off procedure, thereby enabling the maintenance of a high vacuum within the dewar.

2.2.10 Types of getters

In an infrared cryogenic chamber characterized by an evacuated interstitial space, it is not feasible to eliminate the residual gases emanating from the interstitial surfaces of the surfaces of cryochamber material, as the gas molecules adsorbed within the chamber under ultra-high vacuum try to escape. To mitigate this residual out-gassing, getters, which are highly absorptive substances functioning as auxiliary pumping

mechanisms, are employed. Upon activation within a sealed dewar, getters can effectively diminish the pressure from 10^-4 to 10^-6 torr. The activation of getters (which can be activated 10 to 12 times) throughout the entire operational lifespan of the cryogenic chamber allows for an extension of the dewar's lifespan to exceed a decade.

Physio-sorption and chemisorption classifications are the main types of getters with the chemisorption type employed in IR cryochambers due to their operational mechanism, which relies on chemical interactions with gaseous molecules restoring the degraded vacuum. The conventional getters utilized in dewars and their functional mechanisms are illustrated in Figure 2.8.





a) Getter Mechanism

b) Chemisorption type getter

Figure 2.8 Getter operation and the type used in IR cryochamber

These getters of non-evaporable type are predominantly composed of Zr-V-Fe and exhibit the subsequent merits:

- a) Low temperature for activation,
- b) The capacity for multiple reactivation cycles to reveal pristine surfaces, and
- c) An exceptional gettering efficiency.

The standard getter utilized in IR cryochamber with its operational mechanism is illustrated in Figure 2.8.

2.2.11 Temporal parameters such as duration of cool-down and hold-on for the cryogenic chamber

The cooldown duration of an IR cryochamber is defined as the required time for reducing the device's temperature from ambient states to the requisite operational cold temperature, in this case, 88K/78K, indicative of the liquefaction temperature of argon/nitrogen gas. Dewars designed for rapid cooldown may typically exhibit cooldown durations ranging from 10 to 15 seconds, contingent upon the cooling power of the cryocooler and the dewar heat load. In a similar vein, the dewar hold on time is the period for which the mounted detector maintains stability at the required cryogenic temperature of 88K/77K after the cessation of high-pressure fluid supply to the Joule-Thomson (JT) cooler or the deactivation of the power input to the Stirling cooler. Standard durations of approximately a few seconds to a minute are attainable, dependent on the cryochamber heat load.

2.2.12 Selection of appropriate cryocooler

It is essential to have an appropriate cryocooler to achieve the necessary cryogenic temperatures within cryochambers. These devices typically employ insulating methods analogous to dewars and necessitate similar safety measures.

Refrigeration systems are classified into two primary types depending on their operational mechanisms and how they manage refrigerants: closed-cycle refrigerators recycle the same refrigerant, and open-cycle refrigerators, operate by utilizing a pressurized working fluid that releases into the atmosphere following its cooling function.

a) Cryocooler Characteristics and its requirement

The necessary cooling power ranges from a few watts (milli-watts) to a maximum of 10 W, covering temperature intervals that commence at 1K or below and extend to levels that greatly surpass the upper threshold of 120 K linked with the cryogenic domain.

The evaluation of cryocoolers frequently hinges on their refrigeration capacity articulated in watts. However, specifying both the cooling power of the cryocooler

and the associated temperature is essential. The cooling capacity of a cryocooler specified at 1 W at 80 K (the temperature indicative of liquid nitrogen) reveals significant fluctuations relative to its functionality at, for instance, 1 K.

Cryo-coolers are frequently evaluated based on their refrigeration capacity, quantified in watts, at specific temperatures, such as 1W at 80K.

Another critical metric is the input power or the work necessary to attain the refrigeration effect.

The coefficient of performance of a refrigerator is defined as the ratio:

COP = refrigeration capacity/power input or

COP = heat lifted / work done

The ideal coefficient of performance is the Carnot value:

$$COP_{carnot} = \frac{T_R}{\left(T_C - T_R\right)}$$

where T_R is the minimum cycle temperature (usually the refrigeration temperature) and T_C is the maximum temperature of the cycle (generally the atmospheric temperature). The ratio of the actual coefficient of performance to the Carnot coefficient of performance is called the efficiency (η). This cooler efficiency indicates how an actual apparatus compares to the theoretical ideal machine in thermodynamic terms. Thus:

$$\eta = \frac{COP_{actual}}{COP_{actual}} = \frac{(\text{Re } f. capacity/Powerinput)}{(T_R/T_C - T_R)}$$

The operational efficacy of presently accessible cryocoolers fluctuates between a minimum threshold below 1% and a maximum ceiling approaching 50%.

The compact cryocoolers employed in electronic applications exhibit the lowest levels of efficiency because almost all refrigeration is spent to maintain the cryo temperature domain within the apparatus. The rest of the refrigeration, which denotes the refrigeration output obtainable from these units, is minimal (measured in fractions of a watt). In instances where the refrigeration demand is elevated, larger refrigeration units are utilized, which generally demonstrate enhanced efficiency.

The essential factors relevant to the performance of cryocoolers include not only the overall mass and volumetric dimensions of the entire system but also, in specific instances, the mass and volume associated with the cold region itself. This latter aspect

holds particular significance in missile guidance systems, with cryocooled detectors and optoelectronic components securely mounted on rotating gimbals. For optimal configuration minimal mass and low volume are necessary for a swift response to dynamic conditions without the influence of substantial inertial forces.

The cool-down time defined as the interval required for achieving stable operational performance with specified conditions post-initiation, is a vital consideration in numerous applications of miniature systems, especially those connected to weaponry. The dual requirement of a rapid cool-down with a gradual warm-up presents a formidable challenge, as it necessitates the management of opposing high and low thermal masses. The cool-down process may be expedited by initiating operations at elevated pressure or high speed and returning to the standard operational configuration. Mechanical vibrations and electromagnetic emissions within the cold part represent critical cryocooler attributes. Certain applications necessitate the complete eradication of mechanical and electromagnetic acoustic signatures achieved by

- i) Physically separating the cold area from the compressor part, where the large input power is needed and extensive heat transfer occurs.
- ii) Complete removal of dynamic parts from the cold area;
- iii) Construct cold regions parts of plastic, ceramic, and other non-magnetic materials

The operational lifespan represents an additional essential variable often referred to as the Mean Time Before Failure (M.T.B.F.) or, the mean time before maintenance (M.T.B.M.). This variable is the average operational time before failing or undergoing maintenance in the case of several identical cryocoolers operational in analogous environments.

b) Choosing a Cryocoolers for IR detector cryochamber

The cryocooler selection is dependent upon the specific application at hand. In missile applications with a system on board and the limited defined cooling time, a Joule Thomson (JT) mini-cooler is employed; conversely, when a dewar is necessitated for terrestrial applications such as the imaging systems of tanks and Hand Held Thermal Imager (HHTI), a Stirling cooler is deemed more appropriate.

The two predominant categories of cryocoolers utilized for achieving cryogenic temperatures in a dewar are:

A) Joule Thomson Minicooler: Miniature JT Cryocoolers are fundamentally predicated on the Joule-Thomson effect, a phenomenon named in honor of James Prescott Joule and William Thomson (1st Barron Lord Kelvin), two British scientists who elucidated this fundamental yet profoundly advantageous principle in the year 1850 in Manchester, England. The principle states "When a gas undergoes expansion from a state of elevated pressure to a state of reduced pressure through an orifice while maintaining constant enthalpy, a decrease in temperature will be observed." The resultant effect of temperature variation due to isenthalpic alterations in pressure is quantitatively expressed by the Joule-Thomson coefficient, denoted as μJT, which is formally defined by

$$\mu_{\rm JT} = (\partial T / \partial P)_{\rm h}$$

For a real gas, the Joule-Thomson coefficient, represented by the symbol μJT exhibits either a positive or negative value depending upon the specific fluid temperature before the expansion process.

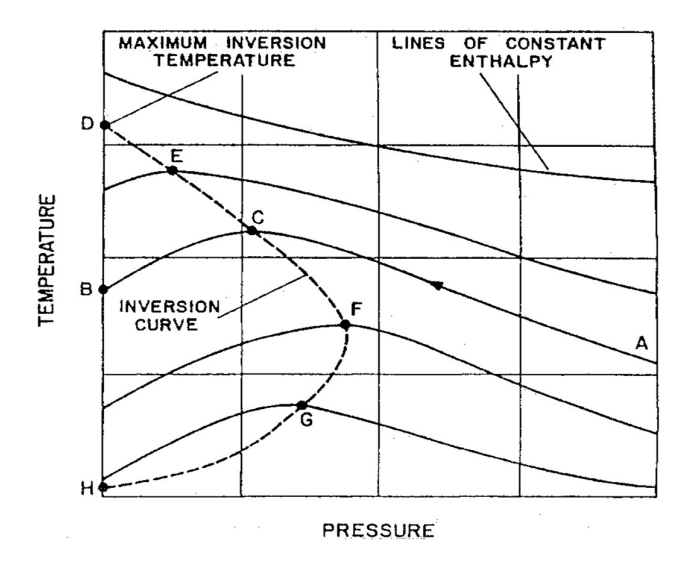


Figure 2.9 Temperature and Pressure plot for varying enthalpies with inversion curve

The Joule-Thomson coefficient, µJT for ideal gases is zero. Figure 2.9 illustrates the relationship between temperature (T) and pressure (P) for different enthalpy values, specifically concerning a real gas. For cooling, one must function within the area on the left of the inversion curve. The maximum inversion temperatures for commonly used gases such as nitrogen and argon are above ambient temperature.

Typically, high-pressure nitrogen or argon gas, exceeding 400 bar and situated below its respective inversion temperatures of 623K and 722K, is subjected to expansion through a micro-orifice, resulting in a temperature reduction. The gas that has undergone expansion facilitates the cooling of the incoming hot gas via the exchange of heat, and the cooling of incoming gas ensues till the liquid is formed.

To operate the heat exchanger at maximum efficiency, the interface between the Joule-Thomson cooler and the cryochamber must be within a stringent tolerance, of approximately \pm 10 micrometers.

To achieve maximum efficiency in the heat exchange process, the fitting of the Joule-Thomson cooler with the cryochamber must be maintained within a stringent tolerance range of approximately 10 microns.

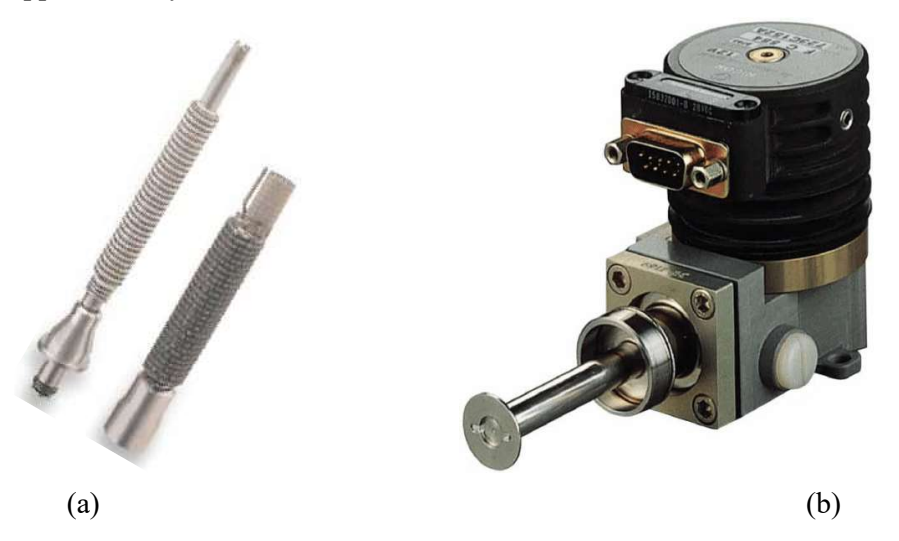


Figure 2.10 A typical (a) Joule Thomson (JT) cooler and (b) Stirling Cooler The merits of the Joule Thomson cryocooler shown in Figure 2.10 (a) are as below,

- i) Instantaneous cooling capability
- ii) Minimum temperature fluctuations
- iii) Lightweight & compact design
- iv) Noise-free operation
- v) Operates without any power requirement
- vi) No moving parts
- vii) Sturdy and Reliable

A few Joule Thomson cryocooler demerits are as,

- i) Challenge to operate at very high pressure
- ii) Limited cooling power
- iii) The capacity of the gas reservoir dictates operation time
- iv) Issue of clogging or blockage
- v) Requirement of high-purity gas or filtration
- vi) Need for high-pressure gas booster, supply lines, and storage equipment
- B) Stirling Cryocooler: It operates as a refrigerator within a closed thermodynamic cycle, activated with electrical energy. This cooler is offered in an integral configuration (where the compressor and cold finger constitute a single unit) and a split configuration (where a flexible line connects the compressor to the cold finger). Consequently, the design of this cooler dictates the corresponding architecture of the infrared cryochamber or dewar.

In contrast to the Joule-Thomson mini-cooler, the Stirling cooler does not require a continuous supply of high-pressure working fluid, thereby minimizing the requisite auxiliary components. Its sole requirement is an electrical power source, enabling it to operate continuously for extended durations. This renders it particularly advantageous for applications such as night vision systems in armored combat vehicle.

2.2.13 Design for Mechanical Strength

The majority of infrared cryochambers are characterized by a cylindrical geometry and possess wall structures of adequate thickness to endure a pressure of one atmosphere (approximately 14.7 psi) when exposed to an ultra-high vacuum environment, thereby ensuring that the dewar remains structurally intact under the influence of the existing atmospheric pressure.

The design of the Cryochamber or Dewar, when subjected to an external pressure of one atmosphere, can be articulated through the following equation (per ASME, Section-8, Part II):

$$P_{CP}\!=\!\left[2.6\;E\;\left(t/d_{o}\right)^{\;2.5}\;\right]/\left[\left(L/d_{o}\right)-0.45\;\left(t/d_{o}\right)^{\;0.5}\;\right]$$

where,

 P_{cp} = Collapsing pressure,

E = Young's Modulus of Cryochamber material (SS),

t = Wall thickness of Cryochamber,

L = Length of Cryochamber &

 d_0 = Outer dia. of Cryochamber.

Sample calculation for a DDCA Dewar assuming,

L = 70 mm; $d_0 = 30 \text{mm}$; t = 0.1 mm &

 $E = 2x10^6 \text{ kg/cm}^2 \text{ or } 3x10^7 \text{ psi}$

The calculated value of collapsing pressure (Pcp) is 21.7 psi, which exceeds the standard atmospheric pressure of 14.7 psi. Thus, even a wall thickness of 0.1 mm possesses sufficient structural integrity to avert any potential collapse when subjected to an external pressure of 1 atmosphere.

Nonetheless, to ensure adequate rigidity of the cryochamber, a wall thickness typically ranging from half an mm to one mm is employed, as per the specifications necessitated by various fittings and the requisite joints of the cryochamber or Dewar.

2.2.14 Assessment of mechanical integrity and robustness of the cryogenic chamber

To mitigate the transmitted thermal load, the size of mechanical supports is minimized and specialized materials are employed. The subsequent specialized treatment is requisite:

- a. IR cryochamber being fragile is advised to be handled gently.
- b. Electrical connections from the cold end must be managed and modified solely after a comprehensive thermal evaluation.
- To avoid heat loss due to radiation clean and highly polished surfaces are prepared.

The determination of the requisite sturdiness of a cryochamber is influenced by the specific applications intended and the design specifications of the cryochamber are finalized to meet those application criteria. Dewar is subjected to environmental testing to evaluate its structural integrity and performance.

Before each environmental examination, the dewar undergoes a radiographic

assessment and is meticulously evaluated for any observable impairments. After the test, radiographic imaging is conducted and analyzed with the initial radiographic findings recorded before the environmental assessments. In the absence of any detected damage, the dewar is sanctioned for utilization. Comprehensive evaluations of electronic components are also performed to determine the presence of any damage or degradation.

COMPUTATIONAL MODELLING OF IR CRYOCHAMBER

Predicting the cooling characteristics of an IR cryochamber is an involved computational problem due to the occurrence of various heat transfer processes and their significant influences.

It entails considering the heat transfer occurring due to conduction and radiation for steady-state and transient operational scenarios. Thereby, only scant computational studies are available in open literature.

This chapter dwells on the computational analysis of all relevant heat transfer modes and parametric analysis of cryochamber characteristics in steady-state and transient operation scenarios. A pure analytical methodology is relevant only for steady state and is arduous to extend to transient cases due to the introduction of error function and associated numerical rigor. Hence, a universal computational methodology capable of handling both IR functioning modes is proposed.

3.1 Computational Geometry

Fig (3.1) shows the computational geometry and the relevant heat transfer modes considered for computational modeling. Primarily, the chamber consists of the understated sub-sections:

- i) Cylindrical Outer enclosure or the Vacuum Vessel
- ii) Inner cylindrical structure (Cold well)
- iii) Multi pin Feedthrough
- iv) Infra-Red detector mounted on top of the inner dewar
- v) Optical IR window for the detector to receive signal.

Typically, the entire internal assembly viz. the outer enclosure and the inner structure are kept under vacuum conditions to mitigate thermal loss. The inner structure is interfaced with a cooler assembly, which may be based on a variety of refrigeration cycles/ mechanisms viz., JT (Joule Thompson) or Stirling cycle-based cooler.

The construction material is mostly SS-316 for all the sub-sections/ assemblies. However, occasionally, the inner structure may be made from glass, which will obviously have a greater wall thickness than the metal construction.

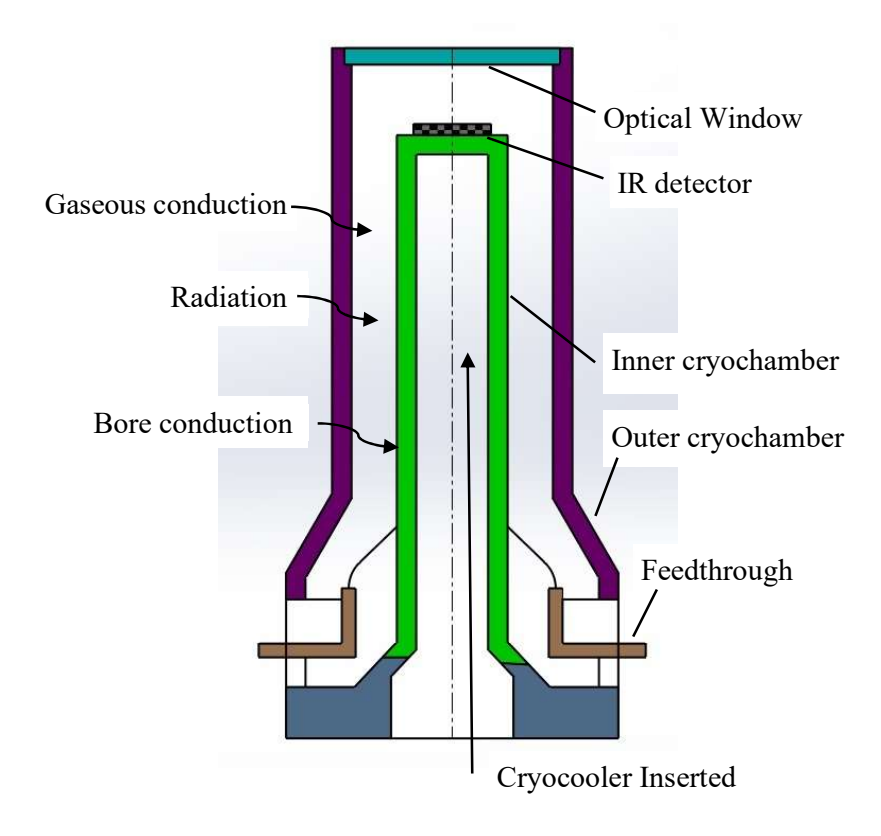


Figure 3.1 Computational geometry and thermal loss mechanisms

3.2 Thermal Loss Mechanisms

A physically correct solution for the above-stated thermal problem requires clear identification of the thermal modes influencing the performance. Significant thermal terms are retained and those with negligible effect are omitted for computational ease and practical outcomes.

The applicable thermal modes in the present problem are;

- i) Conduction along the walls of the inner dewar or cold well
- ii) Heat transfer due to radiation between the cold well (outer) and the outer enclosure (inner)
- iii) Convective heat transfer to the cold well (usually insignificant, hence neglected)
- iv) Thermal load transferred on account of gaseous conduction
- v) Thermal load of detector for steady operating conditions putting necessary demands on the cryocooler assembly

Relevant Assumptions:

- i) Conduction is considered one-dimensional along the cold well
- ii) Temperature variation is considered at only the cold well external surface
- iii) $T_{base} = T_{ambient}$ and $T_{end} = T_{detector}$
- iv) Convective hast load contribution is neglected
- v) Shape function for radiation heat transfer is taken as '1'

3.3 Numerical Formulation

The numerical formulation for the present problem has been worked out for steady and transient operation modes. The steady-state case is illustrated below.

3.3.1 Steady State Operating Mode

The figure below represents a thermal flux balance for the unit element.

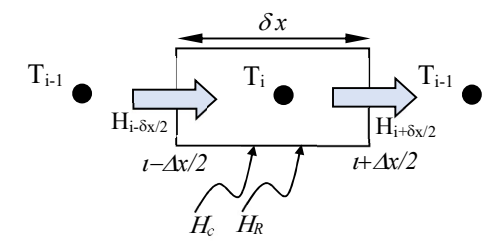


Figure 3.2 Influences of thermal fluxes on unit element

The thermal balance may be expressed as,

$$\sum H_i = 0 \tag{3.1}$$

All thermal fluxes coming into the cell are considered positive and outgoing fluxes are negative. The incoming and outgoing conduction fluxes on the cell surfaces are based on Fourier's law.

 H_c is the gas conduction flux dependent on the heat transfer coefficient, and other factors such as temperature differential and the available surface area to the flux (basically the curved surface area).

 H_R is the thermal flux transferred to radiation and is expressed through Stefan Boltzmann's law. Hence, Eq. (3.1) is expressed as the following equation,

$$-k_{w}A_{w}(\Delta T/\Delta_{x}) + P_{c}\Delta x h_{i}(T_{amb} - T_{i}) + P_{c}\Delta x \sigma_{s} \varepsilon_{c}(T_{amb}^{4} - T_{ii}^{4}) =$$

$$-kA_{w}(\Delta T/\Delta_{x}) + \frac{d}{dx}(-kA\frac{\Delta T}{\Delta x})\Delta x$$
(3.2)

The relation may be simplified as given below,

$$k_w A_w \frac{d^2(T_i)}{dx^2} + P_c h_i (T_{amb} - T_i) + \sigma_s P_c \varepsilon_c (T_{amb}^4 - T_i^4) = 0$$
(3.3)

Eq. (3.3) can further be modified as,

expressed as follows,

$$\frac{d^{2}(T_{i})}{dx^{2}} + \frac{P_{c}h_{i}}{k_{w}A_{w}}(T_{amb} - T_{i}) + \frac{\sigma_{s}P_{c}\varepsilon_{c}}{k_{w}A_{w}}(T_{amb}^{4} - T_{i}^{4}) = 0$$
(3.4)

The finite Difference Method is used for discretizing the above equation and the first term is resolved using the Taylor Series expansion whereas the last term may be linearized.

$$T_{i+1} = T_i + \frac{\partial}{\partial x} T_{i.} \Delta x + \frac{1}{2} \frac{\partial^2 T_i}{\partial x^2} \cdot \Delta x^2 + \cdots$$
 (3.5)

$$T_{i-1} = T_i + \frac{\partial}{\partial x} T_i \cdot \Delta x + \frac{1}{2} \frac{\partial^2 T_i}{\partial x^2} \cdot \Delta x^2 + \cdots$$
 (3.6)

The term-1 is determined by adding Eq. (3.5) and Eq. (3.6) and is substituted in Eq. (3.4). The term-1 is linearized by considering that T_i^4 is expressed as $T_{i*}{}^3T_i$ wherein the power law function is converted to a linear function of T_i with diagonal dominance. Here '*' represents values of the variable that is currently under investigation, which have been derived from the preceding iterations. Therefore, the Eq. (3.4) may be

$$\left[\frac{T_{i+1}-2T_i+T_{i-1}}{(\Delta x^2)}\right] + \frac{P_c h_i}{k_w A_w} T_{amb} - \frac{P_c h_i}{k_w A_w} T_i + \left[\frac{\sigma_s P_c \varepsilon_c}{k_w A_w}\right] T_{amb}^4 - \left[\frac{\sigma_s P_c \varepsilon_c}{k_w A_w}\right] T_i^3 T_i = 0$$
 (3.7)

Therefore, the foregoing equation may be generically expressed as per its dependence on preceding, succeeding, and unit cell temperatures.

$$a_i T_i = a_{i+1} T_{i+1} + a_{i-1} T_{i-1} + S_i$$
 (3.8)
Here,

$$a_{i} = \frac{2}{(\Delta x)^{2}} + \frac{P_{c}h_{i}}{k_{w}A_{w}} + \left[\frac{\sigma_{s}P_{c}\varepsilon_{c}}{k_{w}A_{w}}\right]T_{i}^{3}$$

$$a_{i+1} = \frac{1}{(\Delta x)^{2}}$$

$$a_{i-1} = \frac{1}{(\Delta x)^{2}}$$

$$S_{i} = \frac{\sigma_{s}P_{c}}{k_{w}A_{w}}\varepsilon_{c}.T_{amb}^{4} + \frac{P_{c}h_{i}}{k_{w}A_{w}}T_{amb}$$

Dirichlet Boundary constraints

- i) T_{base} represents the temperature of the metal at the base of the inner cylinder and is the same as the temperature of the surrounding environment (ambient) viz., T_{amb} is typically taken as 300 K.
- ii) The other end temperature is commensurate for infrared detector functioning i.e. $T_{detector}$ is -198 0 C or 77K.

The boundary constraints are the fixed conditions of temperature at both ends.

Operating algorithm

The discerned system of equations for the entire domain may be solved enunciated below:

- i) Provide Inputs: Dimensions and metal/glass characteristics
- ii) Input the number of elements
- iii) Domain discretization and computing the coefficients a_i , a_{i-1} , a_{i+1} , and S_i for each unit cell.
- iv) Specify the appropriate constraints of temperature
- v) The system of equations may be solved by employing the Thomas algorithm to compute the entire field of temperature along the inner cylinder wall
- vi) The set of equations demands iteration for resolving the inherent non-linear nature up to the point where the residuals are $< 1 \times 10^{-3}$

3.3.2 Transient Operating Mode

The operating demands of an IR-detector require that the transient mode be examined quite rigorously as in defense applications reaching optimal temperature conditions is time critical.

This requires computing the time duration to reach the optimal functional temperature i.e. 77K or 88K, referred to as the Cool Down Time (CDT). This CDT depends on the cooling capacity and operational characteristics of the cryocooler utilized.

The thermal flux balance employing the 1-D transient equation accounting for all applicable fluxes is as stated in the equation below.

$$\frac{1}{a_w} \frac{dT_i}{dt} = \frac{d^2 T_i}{dx^2} + \frac{\lambda^2}{\rho_w C_w} (T_{amb} - T_i)$$
Here,
$$\Lambda = \frac{h_i P_c}{k_w A_w}; \quad \alpha = \frac{k_w}{\rho_w C_w}$$
(3.9)

Also, h_i includes thermal contribution due to outgassing gas conduction and radiative effects. $\Lambda = \frac{h_i P_c}{k_w A_w}$

The generic manner of representing gas conductive and radiative heat fluxes is as stated in the equation below, wherein h_i may only account for the former.

$$\frac{dT_i}{dt} = \alpha_w \frac{d^2 T_i}{dx^2} + \Lambda^2 \alpha_w (T_{amb} - T_i) + \beta^2 \alpha_w (T_{amb}^4 - T_i^4)$$

$$\beta^2 = \frac{\sigma_s P_c \varepsilon_c}{k_w A_w}$$
(3.10)

The equation is essentially non-linear and may be linearized by considering the contribution of radiation heat flux as a source term, thereby reducing the numerical intensiveness. Hence, the above equation may be expressed as,

$$\frac{dT_i}{dt} = \alpha_w \frac{d^2 T_i}{dx^2} + \Lambda^2 \alpha_w (T_{amb} - T_i) + \beta^2 \alpha_w (T_{amb}^4 - T_{i*}^4)$$
 (3.11)

The finite Difference Method (FDM) is used to discretize the above equation for transient analysis and Taylor Series expansion to resolve the time- and space-dependent terms. The explicit method of discretization for the equation is elaborated in Eq. (3.12).

$$T_{i}^{n+1} = T_{i}^{n} + \frac{\alpha_{w}\Delta t}{(\Delta x)^{2}} \left[\frac{T_{i+1}^{n} - 2T_{i}^{n} + T_{i-1}^{n}}{(\Delta x)^{2}} \right] + \Lambda^{2} \alpha_{w} (T_{amb} - T_{i}^{n}) + \beta^{2} \alpha_{w} (T_{amb}^{4} - T_{i*}^{4}) \Delta t$$

$$(3.12)$$

Initial Value Constraints

The initial temperature of the inner cylinder including the detector is the ambient temperature (T_{amb}) and drops with the operation of the cooling system. Mathematically, expressed as,

$$T_i = T_{amb}$$
 for all i , at $t=0$

Spatial Constraints

The constraints for computation at each time step,

i) Dirichlet condition:
$$T^n(x=0) = T_{amb}$$
, for all n

ii) Neumann Condition: The detector end forms a flux boundary condition, where the rate of heat extraction bears a linear relation with the local heat temperature value, hence,

$$iii) \quad H_{cool} = l.T(L)(t) + m \tag{3.13}$$

Therefore, the comprehensive representation of the energy equilibrium at the extremity of the grid is mentioned below. It establishes the Neumann boundary condition essential for the mathematical modelling of heat transfer phenomena within the specified domain.

Thus, the energy balance at the tip grid is written as follows, which serves as the Neumann boundary condition.

$$\frac{dT}{dt} = \alpha \frac{dT}{dx}|_{X=L} + \Lambda^2 \alpha \left(T_a - T_p\right) \Delta x + \beta^2 \alpha \left(T_{amb}^4 - T_{i*}^4\right) \Delta x - \left[l.T(L) + m\right]$$
 (3.14)

Operating algorithm

The operating methodology for solving the time-dependent thermal problem is enunciated below,

- i) Provide Inputs: Dimensions and metal/glass characteristics
- ii) Input the number of elements
- iii) Identify the applicable physical equations including all thermal processes
- iv) FDM is employed for equation discretization, and the solution employs explicit formulation with appropriate time steps.
- v) The equations demand iteration for resolving the inherent non-linear nature up to the point where the residuals are $< 1x10^{-3}$ at each discrete time step

a. Effect of gas conduction

The IR devices housed in Dewar assemblies work under extremely low-pressure conditions ($10^{-6} < P < 1$ millibar), and the available mean free path (λ) is comparable to the smallest domain dimension (l), it makes heat transfer in rarefied gas applicable [96, 97]. The extent to which the gas is rarefied is determined by the range of Knudsen's number, the ratio of the mean free path denoted as l to the smallest domain dimensions (l). The corresponding thermal regimes may be segregated as,

- I. Kn > 10: Free Molecular
- II. 0.1 < Kn < 10: Transition
- III. 0.01 < Kn < 0.1: Slip

IV. Kn < 0.01: Continuum

Also, as heat transfer through heat conduction is concerned the gas pressure (P_g) plays the most significant role on account of the molecular number density differentiating between various regimes from free molecular to continuum. Typically, for cases P_g < P_{gfm} defines cases where free molecular conduction is vital and for higher gas pressure close to 1 torr, continuum regime occurs. Furthermore, on comparative analysis of the ratios of heat fluxes associated with both slip and continuum flow regimes, the criterion for regimes is mentioned as,

$$h_c = 1.48P_g \text{ for } P_g < P_{gfm}$$
 (3.15)

Where,
$$P_{gfm} = \frac{kT_{avg}}{10.\sqrt{2d^2l}}$$

$$P_{gfm} = 4 \times 10^{-4} \text{ torr}$$

 $P_{gfm} = 4 \times 10^{-4} \text{ torr}$ $k = \text{Boltzmann constant equal to } 1.38 \times 10^{-23} \text{ JK}^{-1}$ $T_{avg} = \text{Mean temperature of lowest and highest recorded temperature}$

Air's molecular diameter constant as 0.37

$$h_c = \frac{1.48P_g}{1 + 0.34P_g}$$
 for $P_{gfm} < P_g < 1$ torr (3.16)

$$h_c = 4.35$$
 for $P_g > 1$ torr (3.17)

3.4 **Results of Thermal Modelling**

This section explains parametric outcomes derived from thermally modelling a cryochamber. Steady-state analysis results are initially addressed.

3.4.1 Results for Steady-state case

The comparative properties of all three cases of inner cryochamber studied are shown in Table 3.1.

a) Case 1: In examining a test case involving a glass cryochamber (Kim et al, 28), incorporating both material and transport characteristics as listed again in Table 3.2 for better clarity, the temperature distribution along the entire length of the chamber was ascertained.

Table 3.1 Comparative Properties of different Inner Cryochambers Studied

Inner Cryochamber material		Glass (Kim 28)	Glass	Inconel	
Ge	Geometrical Parameters				
a.	O.D. of Cold Finger	9 mm	13.2 mm	11.4 mm	
b.	I. D. of Cold Finger	7 mm	11.2 mm	11.2 mm	
c.	Length of Cold finger	48 mm	30 mm	30 mm	
The	Thermal & Transport Properties				
a.	Gas conduction coefficient	0.632Wm ⁻² K ⁻¹	1.0 Wm ⁻² K ⁻¹	1.0 Wm ⁻² K ⁻¹	
b.	Thermal conductivity	0.8 Wm ⁻¹ K ⁻¹	1.2 Wm ⁻¹ K ⁻¹	7.0 Wm ⁻¹ K ⁻¹	
c.	Specific Heat	800 Jkg ⁻¹ K ⁻¹	800 Jkg ⁻¹ K ⁻¹	435 Jkg ⁻¹ K ⁻¹	
d.	Emissivity	0.02	0.02	0.074	
Ma	Material properties				
a.	Density	2640 kgm ⁻³	2640 kgm ⁻³	8470 kgm ⁻³	
b.	Dewar base temperature	328K & 300K	328 & 300K	328 & 300K	
c.	Detector end temperature	77K	88K	88K	

Table 3.2 Properties of Glass Inner Cryochamber (Case-I) (Kim et al 28)

	Geometrical Parameters			
a.	Outer Diameter of Cold Finger	9 mm		
b.	Inner Diameter of Cold Finger	7 mm		
c.	Length of Cold finger	48 mm		
Thermal & Transport Properties				
a.	Gas conduction coefficient	0.632Wm ⁻² K ⁻¹ (@ 0.5 Pa or 3.8 x 10 ⁻³ torr)		
b.	Thermal conductivity	0.8 Wm ⁻¹ K ⁻¹		
c.	Specific Heat	800 Jkg ⁻¹ K ⁻¹		
d.	Emissivity	0.02		
Material properties				
a.	Density	2640 kgm ⁻³		
b.	Dewar base temperature	328K & 300K		
c.	Detector end temperature	77K		

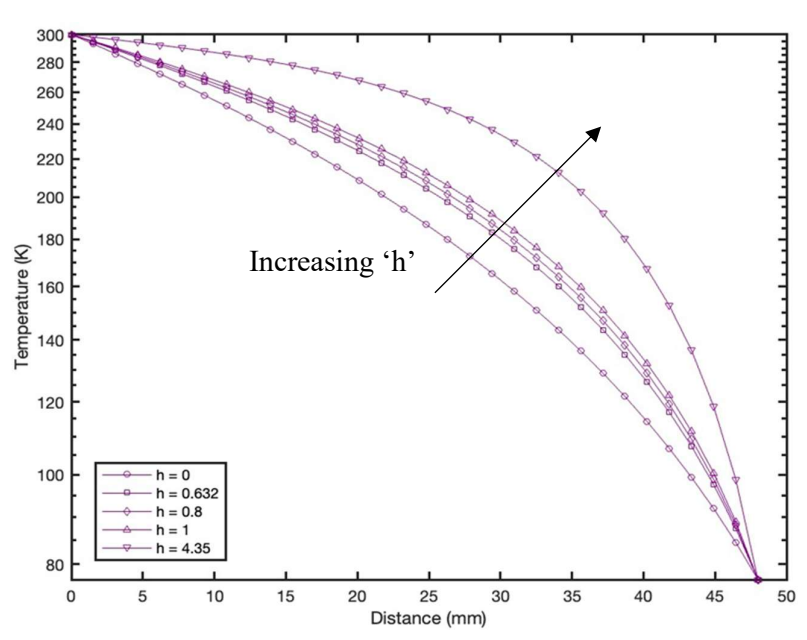


Figure 3.3 Temperature length profile for diverse coefficients of gas conduction Emissivity (ε) is another parameter that may fluctuate due to the degree of surface polish of the cryochamber achieved.

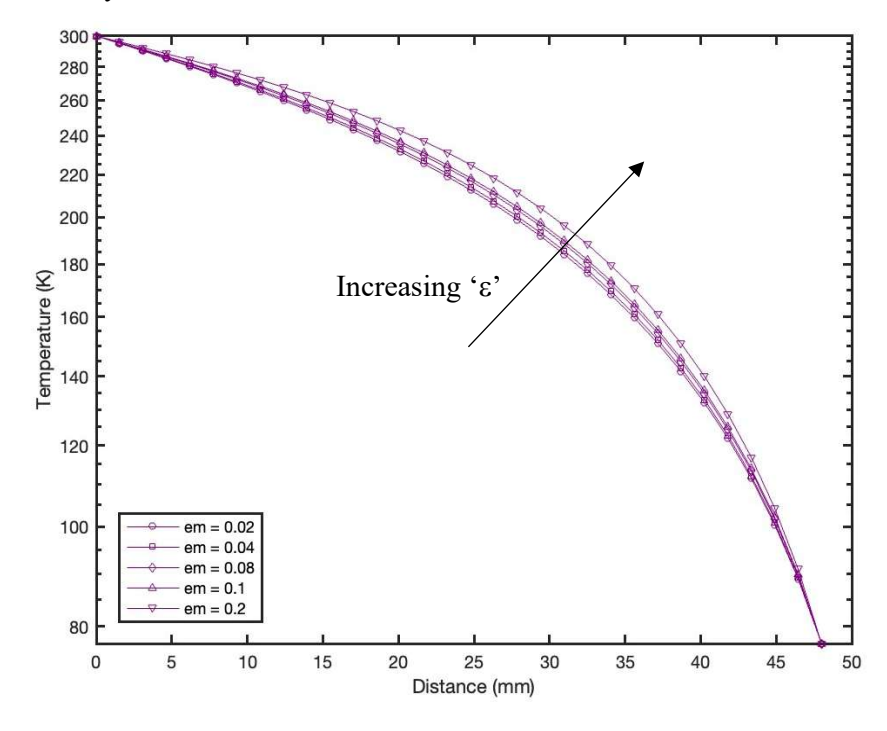


Figure 3.4 Emissivity length profile for diverse values of emissivity

Upon verifying the model's effectiveness, a detailed analysis of the variables through the manipulation of the coefficient of gas conduction (h) is undertaken while keeping the geometric configuration the same.

The coefficient of gas conduction (h) is one parameter that is pressure-dependent and is noted to exhibit an increase with an elevation in pressure. The ramifications of varying gas conduction coefficients on the thermal profile are depicted in Figure 3.3. Consequently, the thermal profile produced due to emissivity variation is plotted in Figure 3.4. As mentioned, Case I pertains to the specifications of the glass cryochamber considered by Kim et al. [28], and the computational results derived match the analytical results anticipated.

b) Case 2 discussed is for an inner glass cryochamber matching with the outer diameter of the developed Joule Thomson cryocooler, and properties are the same as shown in Table 3.1. However, for better understanding and clarity, properties are again mentioned in Table 3.3.

Table 3.3 Properties of Glass Inner Cryochamber Prototype Developed (Case 2)

Geometrical Parameters				
a.	Outer Diameter of Cold Finger	13.2 mm		
b.	Inner Diameter of Cold finger	11.2 mm		
c.	Length of Cold finger	30 mm		
Thermal & Transport Properties				
a.	Gas conduction coefficient	1.0 Wm ⁻² K ⁻¹ (@ 0.5 Pa or 3.8 x 10 ⁻³ torr)		
b.	Thermal conductivity	1.2 Wm ⁻¹ K ⁻¹		
c.	Specific Heat	800 Jkg ⁻¹ K ⁻¹		
d.	Emissivity	0.02		
Material properties				
a.	Density	2640 kgm ⁻³		
b.	Dewar base temperature	328K & 300K		
c.	Detector end temperature	88K		

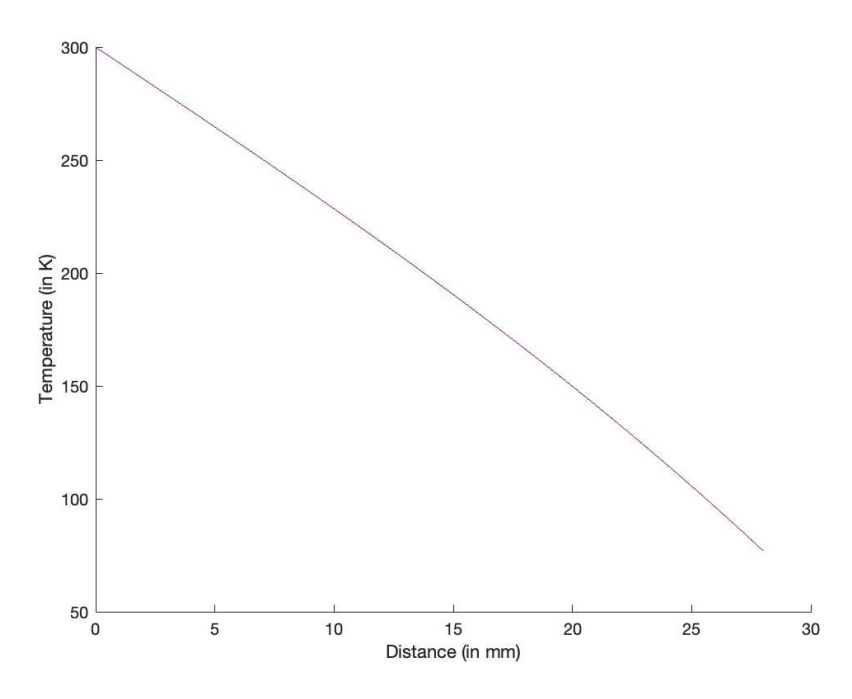


Figure 3.5 Temperature distribution along the length for h=1.0

The distribution along the length in Figure 3.5 exhibits qualitative similarities to one acquired in Case – I, when the gas conduction coefficient is assumed unity.

a) Case 3 is for a Metallic Cryochamber for Rapid Cool Down

Certain projectile munitions need rapid cooling of a sensor into the cryogenic temperature range. A cryochamber with the right material and appropriate geometric and thermal design supports the infrared sensor and promotes rapid cooling.

Certain cases with different hollow inner cryochamber materials were analysed. Both properties related to material composition and transport mechanisms considered for Inconel, though shown in Table 3.1, are again listed in Table 3.4 for better understanding. The fluctuations in the heat conduction coefficient have been investigated, and the outcomes of the study are graphically represented in Figure 3.6, which specifically depicts the behavior of the gas conduction coefficient as it varies within the numerical range extending from '1' to '4.35'.

Table 3.4 Properties of Inconel Inner Cryochamber Prototype Developed (Case 3)

	Geometrical Parameters		
a.	Outer Diameter of Cold Finger	11.4 mm	
b.	Inner Diameter of Cold finger	11.2 mm	
c.	Length of Cold finger	30 mm	
Thermal & Transport Properties			
a.	Gas conduction coefficient	1.0 Wm ⁻² K ⁻¹ (@ 0.5 Pa or 3.8 x 10 ⁻³ torr)	
b.	Thermal conductivity	7.0 Wm ⁻¹ K ⁻¹	
c.	Specific Heat	435 Jkg ⁻¹ K ⁻¹	
d.	Emissivity	0.074	
Material properties			
a.	Density	8470 kgm ⁻³	
b.	Dewar base temperature	328K & 300K	
c.	Detector end temperature	88K	

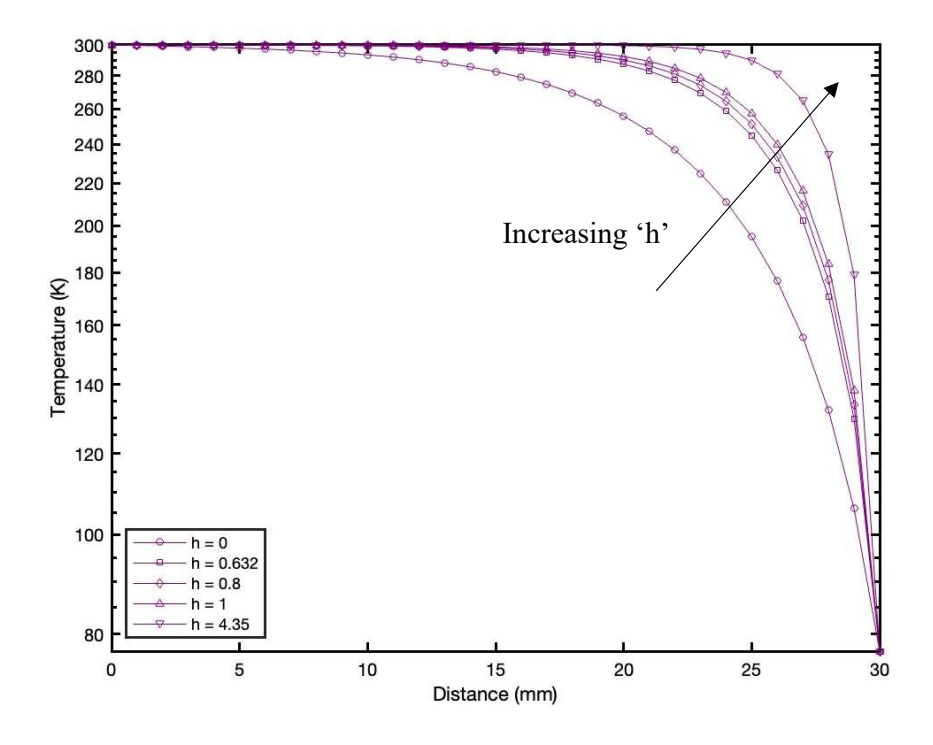


Figure 3.6 Temperature length profile for diverse coefficients of gas conduction for SS cryochamber

Analyzing Figures 3.3, 3.5, and 3.6 reveals that the thermal gradient in the case of steel is significantly more pronounced than in glass. This observation is rationalized by the fact that a substantial fraction of heat transfer occurs via conduction, and steel possesses a markedly higher thermal conductivity than glass.

The subsequent section addresses the quantitative findings of the transient scenario, which is of paramount importance in the context of strategic applications, wherein the duration of the cooling process must be reduced to a minimum. A numerical model that accurately forecasts the cooling duration while considering all heat transfer mechanisms facilitates selecting a cryocooler with sufficient cooling power and associated thermal parameters.

3.4.2 Results of a Transient Case

After demonstrating that the anticipated results exhibit numerical reliability and remain unaffected by the selection of grid quantity and temporal discretization, it is apparent that, for the specified parameters of the cryochamber, the cooldown duration approximates 27 seconds. Given that the reference data utilized is sourced from the work of Kim et al. [28], the forecasted cooldown duration aligns with their findings. The corroborated numerical model for the transient scenario was subsequently employed to estimate the cooldown duration for the constructed test glass cryochamber, matching the JT cryocooler prototype geometry. The geometric configuration of the cryochamber utilized in experimentation is detailed in Table 3.3. Furthermore, the cryocooler in our experimental setup exhibits distinct cooling characteristics, with cryocooler constants a= 0.005 W/K and b= 0.22 W. The pressure within the cryochamber is recorded at approximately 6.8 x 10⁻³ torr, with the gas conduction coefficient (h) quantified as 1.0 Wm⁻²K⁻¹. The emissivity and specific heat remain consistent with those presented in Table 3.3. Figure 3.7 shows the predicted numerical cooldown duration for Case 2.

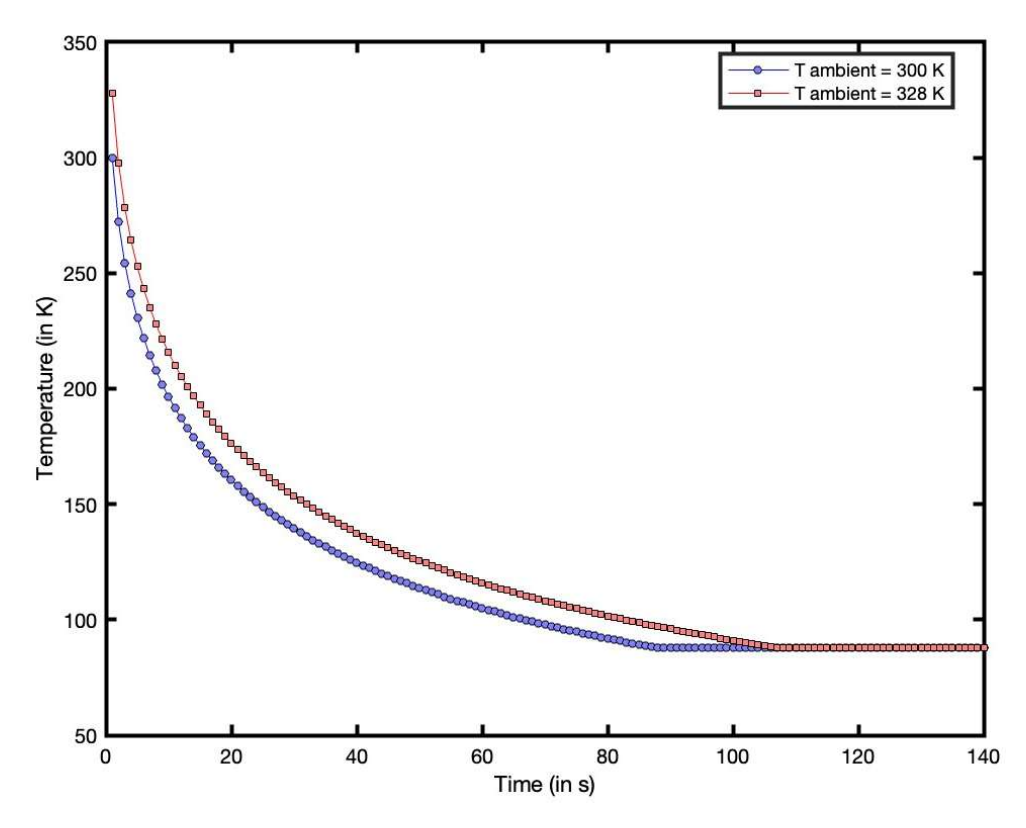


Figure 3.7 Computational detector cool down time (CDT) for Case2 at an ambient temperature of 300K & 328 K under "device OFF" condition

It is apparent from Figure 3.7 that the cooldown duration in 'device OFF' mode, specifically the time required to attain the target temperature of 88 K, is approximately 94 seconds, or 1 minute and 34 seconds when the ambient temperature is 300 K. Furthermore, the influence of ambient temperature on the cooldown duration for the detector is discernible in the same figure. The estimated cooldown period in the 'without device load' condition at 328 K is approximately 114 seconds, or 1 minute and 54 seconds, which exceeds the duration observed when the cryochamber is operated at a standard ambient temperature of 300 K.

In instances where the cryochamber is functioning in 'device ON' mode, the anticipated cooldown duration increases to 98 seconds, or 1 minute and 38 seconds, when the ambient temperature is 300 K, while the cooldown duration extends to 116 seconds, or 1 minute and 56 seconds, at an ambient temperature of 328 K. The findings are illustrated in Figure 3.8.

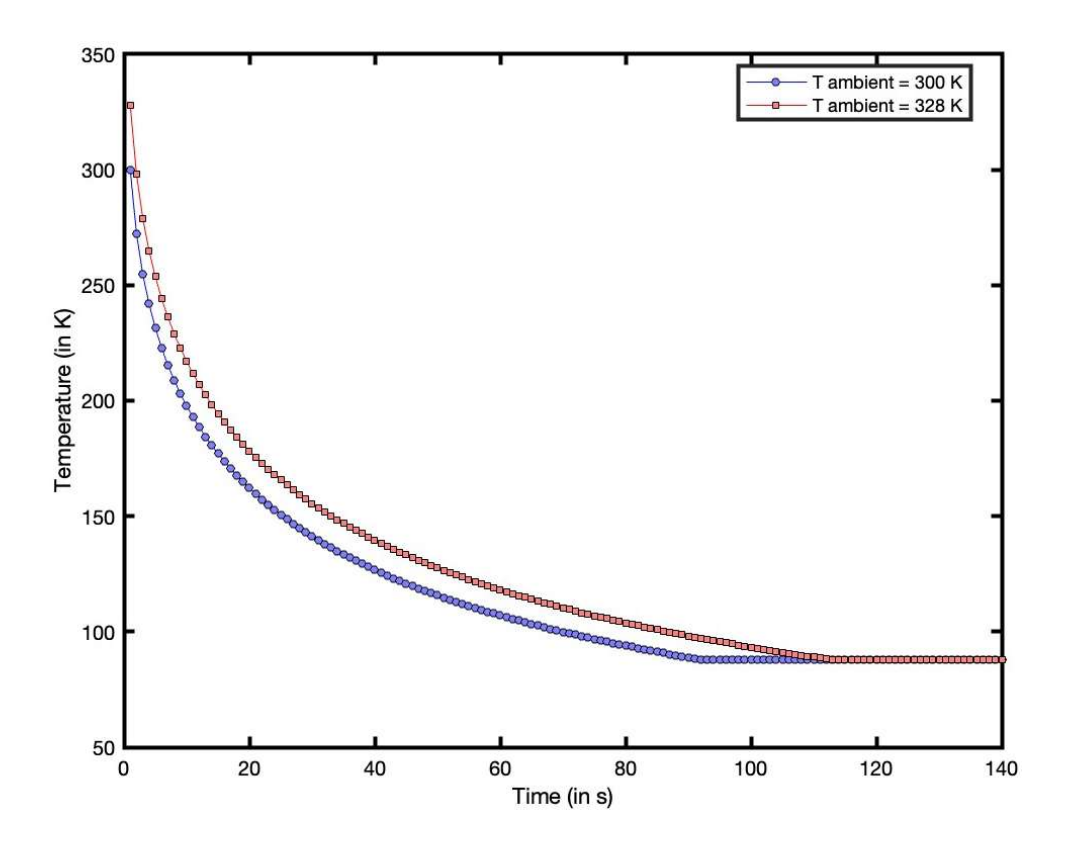


Figure 3.8 Computational detector cool down time (CDT) for glass cryochamber at an ambient temperature of 300K & 328 K under "device ON" condition

After plotting the numerical results for the glass inner cryochamber of glass, the same numerical model was employed to estimate the cooldown duration for the inner cryochamber of Inconel for rapid cooldown requirements. The geometric configuration of the cryochamber utilized is detailed in Table 3.4 and the characteristics of the cryocooler are also the same as in the case of glass cryochamber. The pressure within the cryochamber is recorded at 6.84 x 10^-3 torr, with the gas conduction coefficient (h) quantified as 1.0 Wm^-2K^-1. The numerically predicted cooldown duration for this scenario is illustrated in Figures 3.9 & 3.10.

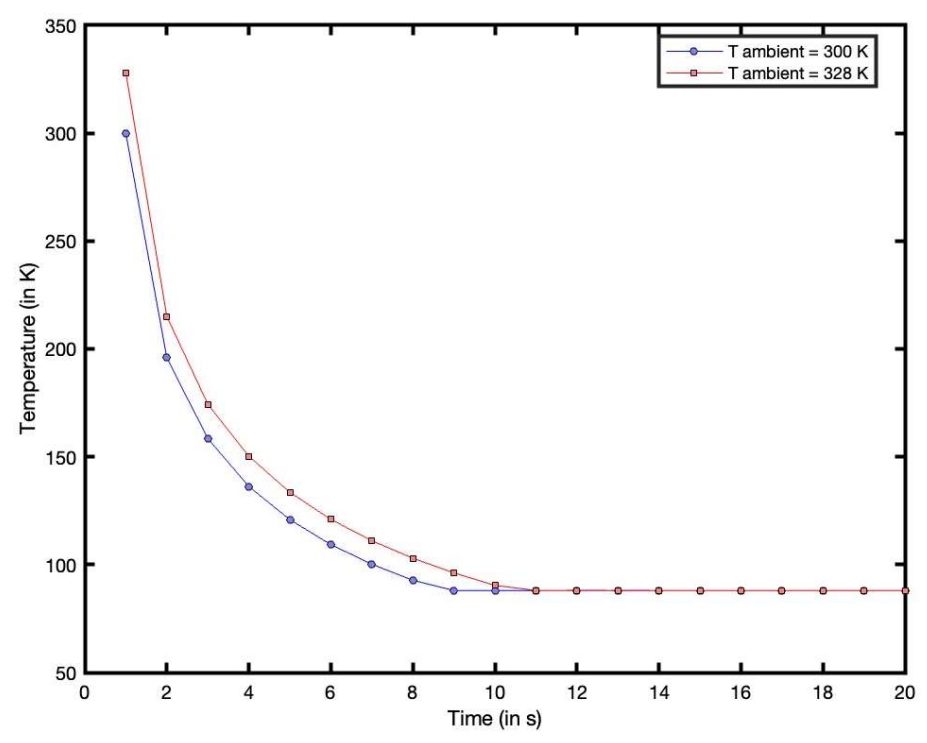


Figure 3.9 Computational detector CDT for Inconel cryochamber at ambient temperature measuring 300K & 328 K for "device OFF" state

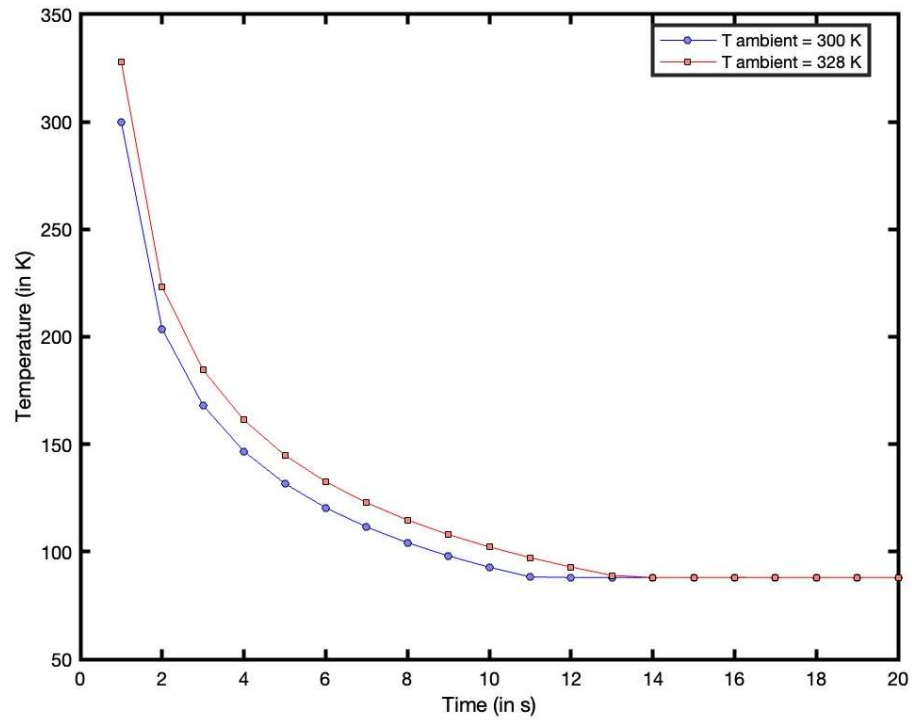


Figure 3.10 Computational detector CDT for Inconel cryochamber at ambient temperature measuring 300K & 328 K for "device ON" state

Figures 3.9 and 3.10 clearly show that the cooldown duration in 'device OFF' mode, in case of rapid cooldown cryochamber is approximately only 09 seconds, when the ambient temperature is 300 K and the same CDT at 328 K ambient temperature is 11 secs in 'device OFF' condition.

The cooldown duration of the same Inconel cryochamber when operating in 'device ON' marginally increases to 12 seconds, when the ambient temperature is 300 K the cooldown duration increases to 13 seconds, at an ambient temperature of 328 K.

It is noted that the variation in thermal conductivity plays a crucial role in influencing the duration required for the cooling of the detector to cryogenic temperature. Furthermore, when one takes into account the fact that the thermal penetration depth, a critical parameter, can be expressed as a function of the square root of thermal diffusivity (α) and cool-down time (t_c) , along with the understanding that the refrigeration capacity exhibits a linear relationship with temperature, it becomes evident that the cooldown time can be approximated by the equation $t_c \sim k(\rho c)\Delta T$, wherein ΔT signifies the differential between the detector temperature and the surrounding ambient temperature.

A noteworthy finding from the analysis indicates that gas pressure exerts a negligible influence on the cooldown duration, in contrast to the steady-state scenarios. This phenomenon can be attributed to the constrained effect of gaseous conduction, confined to a localized area adjacent to the cold end, failing to exert any considerable effect on the cooldown duration. In steady-state conditions, the entire domain is involved, wherein the gas conduction coefficient manifests a pronounced effect regarding the established temperature length profile. The thermal penetration depth requires approximately 400 seconds to increase to a value commensurate with the total length of the bore.

THERMOPHYSICAL ANALYSIS AND PROTOTYPE DEVELOPMENT OF MINIATURE JOULE THOMSON CRYOCOOLER

4.1 Description of Miniature Joule Thomson Cryocooler

A typical miniature Joule–Thomson cryocooler mainly consists of a recuperative heat exchanger, an expansion device, and an evaporator as shown in Fig. 4.1 (a). The Temperature-Entropy (T-S) diagram is shown in Fig. 4.2 (b).

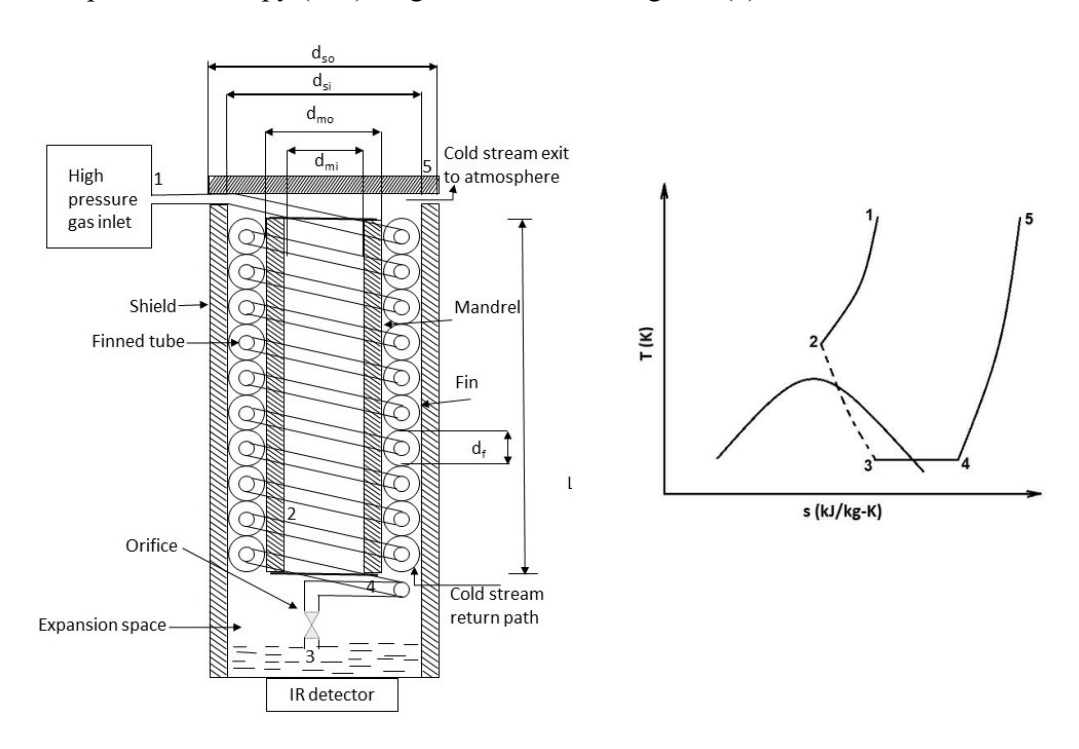


Figure 4.1 (a) JT cooler with recuperative H.E (b) T-S diagram for JT cooler

The recuperative type heat exchanger of the J-T cryocooler consists of a capillary tube helically wound around a cylindrical mandrel. To increase the heat transfer rate of the shell side, the capillary tube is finned in the radial direction. The sum of the fin thickness and the gap between two fins is called the fin pitch. The helical capillary together with the mandrel is placed inside a cylindrical shield. The mandrel and shield form the framework of the cryocooler. The orifice is placed at the end of the heat

exchanger. The finned capillary is connected to the orifice. Hot high-pressure (h.p.) stream of gas (1) passes through a heat exchanger. Cold low-pressure (l.p.) stream (4) flows through the space between the outer diameter of the mandrel and the inner diameter of the outer shield (shell). The top end of cooler (5) is the heat exchanger's hot end (at ambient temperature), while the bottom end (3,4) is the cold end (typically at 80K/90K). The high-pressure (2) gas expands through an orifice into an evaporator (or reservoir) space (at the bottom of the cooler) and is cooled by the Joule-Thomson effect. Under a steady state condition, some gas liquefies after isenthalpic expansion through the orifice. This liquid cryogen extracts heat from the target body to be cooled.

4.2 Theoretical and Thermophysics Analysis

Theoretical analysis for the geometry of the Joule Thomson cooler model is done for specified thermal performance specifically for the cooling capacity of the J-T cooler required. The underlying assumptions for the analysis are as follows:

J-T Cooler operates under steady state condition

Gas streams operate at an average inlet and outlet temperature. The Spatial and temporal temperature profile along the longitudinal direction is neglected

Considering the above-stated assumptions, the heat exchanger geometry is developed and analyzed. The mathematical formulation concerning the theoretical model of the J-T heat exchanger is discussed in the following section.

4.3 Geometrical Parameters of the J-T Cooler

Wetted area:
$$A_w = \left[\frac{\pi}{4} \times (d_{of}^2 - d_{ofb}^2) \times 2 + \pi \times d_{ofb} \times g_f\right] \times N_f$$
 (4.1)

Free volume:
$$\frac{\pi}{4} \times (d_{of}^2 - d_{ofb}^2) \times g_f \times N_f$$
 (4.2)

Equivalent Diameter:
$$D_e = \frac{(4 \times Free\ Volume\)}{A_W}$$
 (4.3)

4.4 Thermo- Fluidic Parameters of the J-T cooler

Cooling Capacity:
$$Q_{cool} = m(H_4 - H_3)$$
 (4.4)

$$Overall\ Heat\ Transfer\ Coefficient:\ \frac{1}{U} =\ \left[\frac{1}{(\eta_f \times h_c)}\right] \ +\ \left[\frac{\frac{A_{o,c}}{A_{o,h}}}{(\eta_{o,h} \times h_h)}\right] +\ \left[\frac{A_{oc}\ln\left(\frac{d_{of}}{d_{if}}\right)}{2\pi kL}\right]$$

(4.5)

wherein, correlations for the heat transfer coefficient are given by Flynn [98].

Convective Heat transfer coefficient:
$$h = \frac{kNu}{D_e}$$
 (4.6)

Hot stream:
$$h_c = 0.023 C_{p_h} G_h Re_h^{-0.2} Pr_h^{-2/3} \left(1 + 3.5 \frac{D_e}{D_h}\right)$$
 (4.7)

where $G_h = {m \choose A_h} D_e = d_{ci}$ (inside diameter of the capillary tube) and

 $D_h = Helix diameter$

Cold stream:
$$h_c = 0.235 \, C p_c G_c R e_c^{-0.4} P r_c^{-2/3}$$
 where $G_c = m/A_c$ (4.8)

Reynolds Number:
$$Re = \frac{D_e G}{\mu}$$
 (4.9)

The effectiveness is calculated using standard principles using No. of transfer Units (NTU) as given by Holman [99] & Hong et al. [50]

Effectiveness:
$$\varepsilon = \frac{1 - e^{(-NTU(1 - C_r))}}{1 - C_r e^{(-NTU(1 - C_r))}}$$
 (4.10)

wherein,

No. of Transfer Units:
$$NTU = \frac{UA}{c_{min}}$$
 (4.11)

Ideal Effectiveness:
$$\varepsilon = \frac{T_{c,o} - T_{c,i}}{T_{h,i} - T_{c,i}}$$
 (4.12)

Pressure Drop:
$$\Delta P = f\left(\frac{L}{D}\right)\rho \frac{V^2}{2}$$
 (4.13)

Also, the Fanning friction factors for hot and cold streams are given by Flynn [98] as stated below,

$$f_h = 0.184 Re_h^{-0.2} \left(1 + 3.5 \frac{D_e}{D_h} \right) \tag{4.14}$$

$$f_c = 2 Re_c^{-0.15} \left(0.088 + 0.16 \frac{X_L}{(X_T - 1)^{-n}} \right)$$
 (4.15)

Here, $X_T = {p_T}/{d_{of}} = {D_h}/{d_{of}} X_L = {p_L}/{d_{of}}$ where p_T and p_L are transverse and

longitudinal pitch respectively, and $X_L = \frac{p_L}{d_{of}} n = 0.43 + \frac{1.13}{X_L}$

corresponding

to the fin geometry shown in Fig. 4.2.

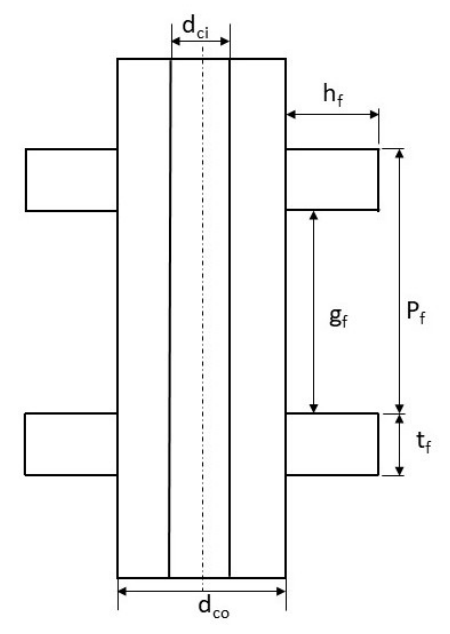


Fig 4.2: Geometry of Helical Tube fin

Further, the liquid fraction in the evaporator may be determined considering typical heat exchanger efficiency using the relation below,

$$\chi = \frac{H_4 - H_3}{H_4 - H_f} \tag{4.16}$$

It is worth noting that the mass flow rate of active gas undergoing isenthalpic expansion is controlled by the backpressure and orifice throat area. A typical relation for determining mass flow rate for a choked condition for a given fixed area orifice and known backpressure and stagnation temperature conditions suggested by James [100] is as

$$m = \frac{p_0 A}{\sqrt{T_0}} \sqrt{\frac{\gamma}{R} \left\{ \frac{2}{\gamma + 1} \right\}^{\frac{\gamma + 1}{2(\gamma - 1)}}}$$
 (4.17)

where the discharge coefficient (ratio of actual or measured flow rate to theoretical flow rate) is taken as unity. In this context, Hong et al. [50,54], have treated mass flow as a variable independent of pressure. Maytal et al. [101] have treated free mass flow and recuperative mass flow separately, having direct and square root proportionality respectively. However, in the present study, the mass flow computations are strictly based on Eq. (4.17), considering a fixed area orifice operating under choked flow conditions.

Although the theoretical analysis discussed is vital for developing the J-T heat

exchanger geometry it has obvious limitations in predicting an accurate temperature profile in the exchanger in the presence of a mandrel or shield. Furthermore, the theoretical models also have potential shortcomings emanating from the underlying assumptions made. Therefore, comprehensive numerical modeling is performed and thermal analysis is conducted on the developed J-T cooler geometry.

Note that the present rigorous numerical analysis essentially involves generating the temperature profiles along the viz., h.p. gas flow, the wall separating the h.p. and the l.p. gas flows, l.p. gas flow, mandrel, and shield. In addition, the material properties of the shield, boundary wall, and mandrel, along with pressure and temperature dependences of gas (both in h.p. and the l.p. streams), are accounted for in the present numerical modeling using heat flux balancing methodology outlined by Anderson et al. [102] & Singhal et al. [27] is given as

Hot Stream:
$$m_c C_{ph} \frac{dT_h}{dx} = h_h p_{ci} (T_w - T_h)$$
 (4.18)

Cold Stream:
$$m_c C_{pc} \frac{dT_c}{dx} = h_h [p_{co}(T_c - T_w) + p_{si}(T_c - T_s) + p_{mo}(T_c - T_m)]$$
(4.19)

Wall Temperature:
$$k_w A_w \frac{d^2 T_w}{dx^2} = h_h p_{ci} (T_w - T_h) + h_c p_{co} (T_w - T_c)$$
 (4.20)

Mandrel Temperature:
$$k_m A_m \frac{d^2 T_m}{dx^2} = h_c p_{mo} (T_m - T_c)$$
 (4.21)

Shield Temperature:
$$k_s A_s \frac{d^2 T_s}{dx^2} = h_c p_{si} (T_s - T_c) + h_r p_{so} (T_s^4 - T_{amb}^4)$$
 (4.22)

Here, the radiation heat transfer coefficient h_r (in Eq.15) is given as,

$$h_r = \frac{\sigma}{\frac{1}{\varepsilon_S} + \frac{A_{SO}}{A_r} \left\{ \frac{1}{\varepsilon_r} - 1 \right\}} \tag{4.23}$$

The J-T cooler numerical model is tested for Argon gas but may be easily configured for various combinations of gases and the tube, shield, and mandrel materials to arrive at the most optimum design solution.

Here, the radiation term is linearized by using the equation suggested by Patankar [103] viz. $S = S_c + S_p T_p$. It may be made a known source term instead of making it temperature-dependent by considering $S_p = 0$ and $S_c = \alpha (T_{amb}^4 - T^{*4}) \cdot T^*$, is the cell temperature of the previous iteration (assumed value at initialization), and it is known.

Further, the pressure drop is another significant parameter in the design of the J-T heat

exchanger's length, the pressure variation along the flow direction may be computed employing the following relation.

$$\frac{dp}{dx} = \frac{\frac{2f}{\rho D_h}}{\frac{d\rho}{p^2 dp} - \frac{1}{G^2}} \tag{4.24}$$

In governing equations, a set of variables is suitably non-dimensionalized. All the temperature terms are normalized with $(T_1 - T_4)$. X –coordinate is normalized with L. All areas are normalized with $A_c = \Sigma(A_{co}, A_{mo}, A_{si})$. Similarly, the wall thermal resistance is normalized with mC_{pc} (happens to be C_{min}).

While solving the above-stated five coupled differential equations (4.18) - (4.22), an additional approximation of neglecting variation of thermo-physical gas properties with temperature is made. This assumption is essentially valid primarily due to the low-temperature regime of the J-T cooler operation.

As stated below, the Dirichlet boundary conditions are employed at both the cold and the hot end of the J-T heat exchanger.

Hot end (x=0):
$$T_h = T_{hin}, T_w = T_{hin}, T_s = T_{hin}$$

$$Cold\ end\ (x=L): \qquad T_c = T_{cin}\ \&\ \frac{dT_w}{dx} = \frac{dT_m}{dx} = \frac{dT_s}{dx} = 0$$

4.5 Effect of various parameters on J-T cryocooler performance

The impact of listed parameters on the comprehensive performance of the Joule-Thomson cryocooler system is investigated with argon as the working fluid.

- i) Rate of Mass flow
- ii) Density of Fins
- iii) Fluid supply pressure
- iv) Length of fin

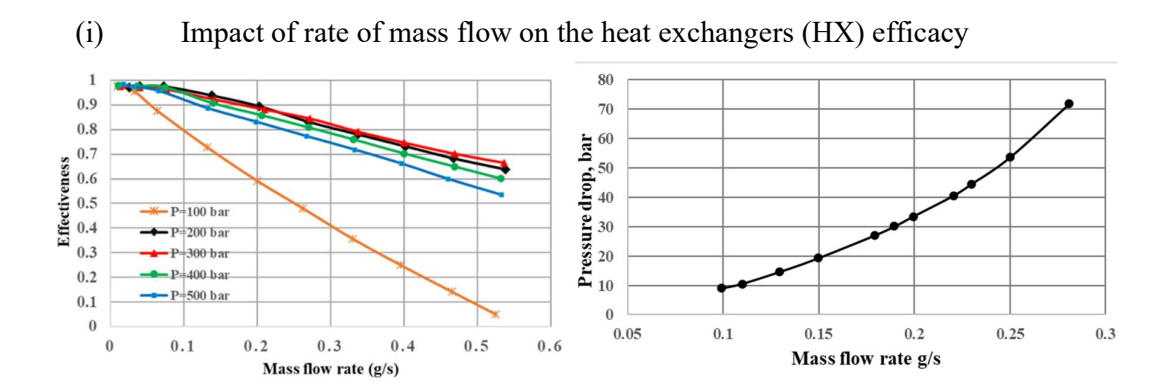
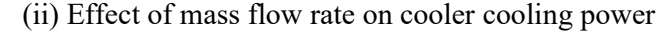


Figure 4.3 Impact of mass flow rate on heat exchanger performance

Fig. 4.3 indicates that an elevated mass flow rate correlates with a pronounced increase in the pressure differential of the thermal fluid, accompanied by a reduction in the efficacy and operational efficiency of the heat exchanger.



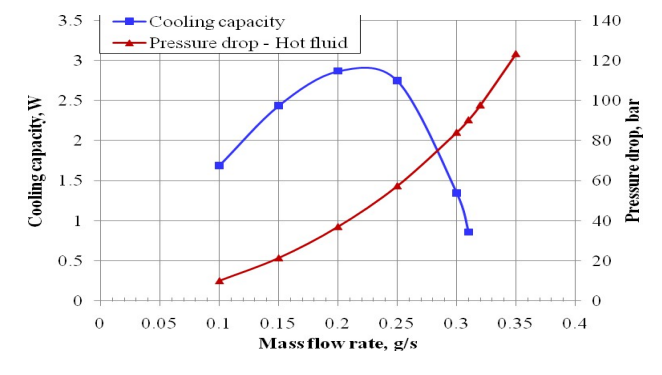


Figure 4.4 Variation of cooling capacity and pressure drop for heat exchanger

Analyzing Figure 4.4, one can deduce that there exists a direct correlation whereby increasing the mass flow rate increases the cooling capacity of the system, reaching a maximum at 0.2 grams per second specific mass flow rate, after which a reduction in operational efficiency is observed. Furthermore, increasing the mass flow rate increases the pressure drop experienced by the hot fluid.

(iii) Relation between fin density and overall effectiveness of recuperative HX

Fig. 4.5 illustrates how fin density influences heat exchanger performance under varying supply pressures. It has been noted that increasing fin density increases the total efficiency and effectiveness of the heat exchange process. However, a higher fin density might result in greater resistance to flow on the cold side.

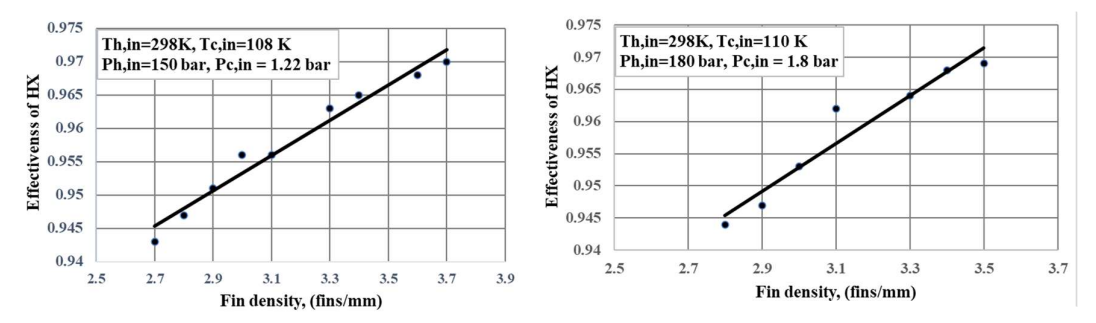


Figure 4.5 Impact of fin density on HX effectiveness

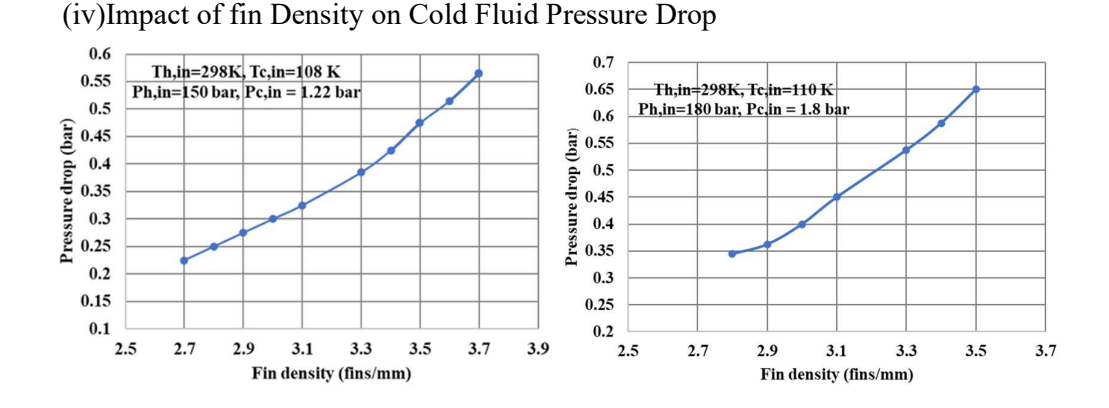


Figure 4.6 Impact of fin density on the drop in pressure in the heat exchanger

Fig. 4.6 effectively demonstrates the correlation and pressure drop experienced by the cold fluid increases with an increase in fin density as it traverses through the cooler. The analysis reveals that the optimal fin density for Case I is 3.3, while for Case II, the optimal fin density is slightly higher at 3.5, indicating a variation in performance based on differing conditions or configurations.

(v) Impact of fin length on the drop in pressure in the heat exchanger

Fig. 4.7 illustrates that the observed pressure drops for both the hot entering gas and the cold gas exiting exhibit a notable reduction with an increase in the fin length. Moreover, the decrease in pressure drop the returning cold gas experiences is substantially greater than in the entering hot high-pressure gas.

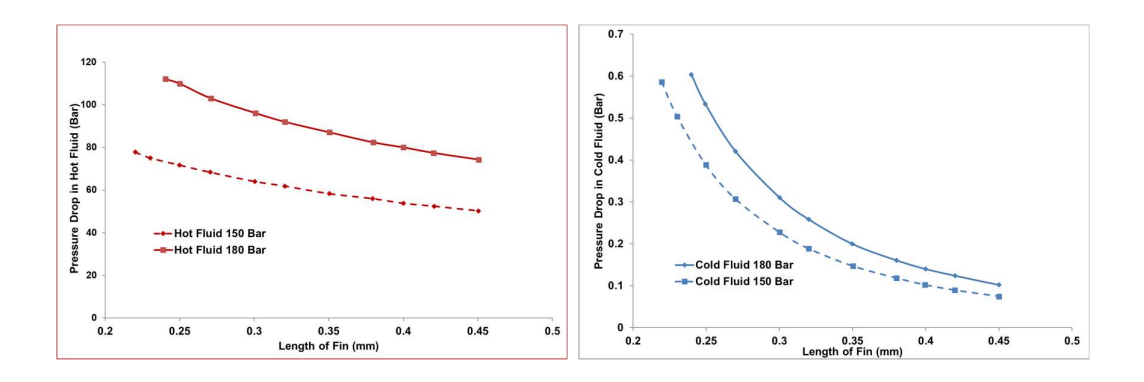


Figure 4.7 Impact of fin length on the drop in pressure in the HX

(vi) Impact of supply pressure on the cooler performance

Fig. 4.8 illustrates that the cooler's cooling capacity increases with increased supply pressure. Further, with increasing supply pressure levels the mass flow rate increases to maximize cooling power or capacity.

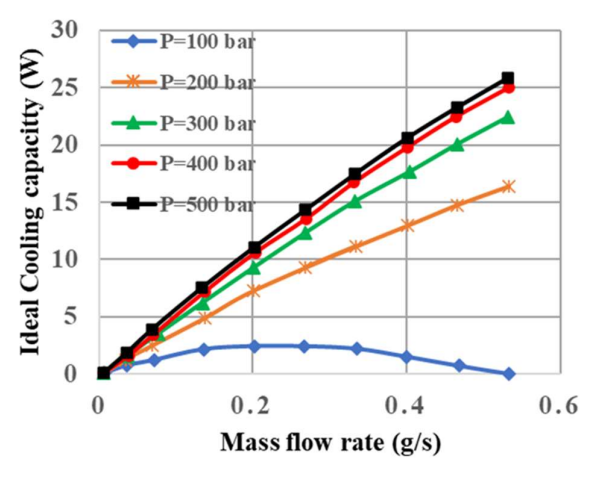


Figure 4.8 Relation between supply pressure and the cryocooler capacity

A generic flowchart highlighting the computational modelling approach for JT cryocooler simulation is shown in Fig. 4.9.

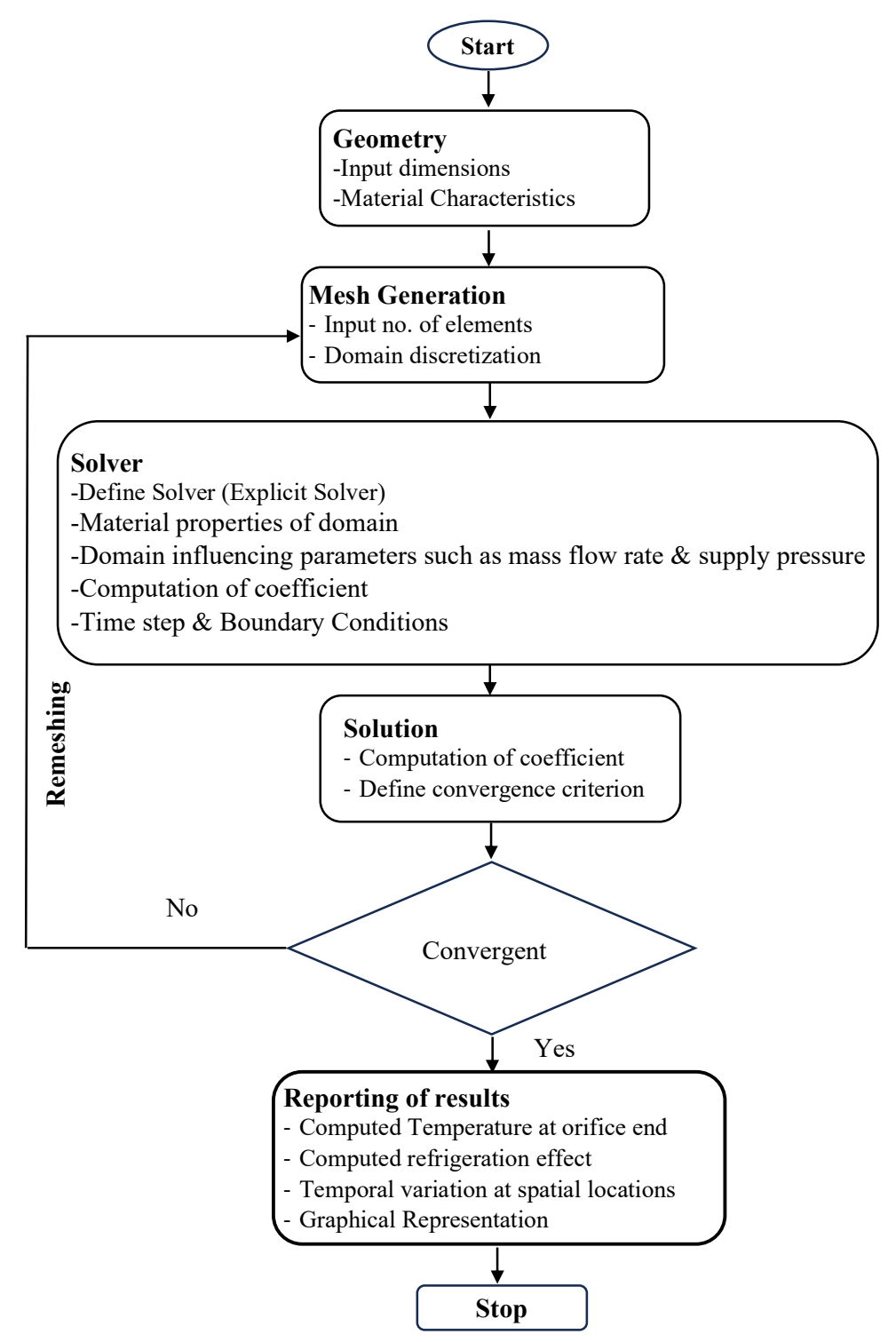


Figure 4.9 Generic Flow chart for computational modelling of JT cooler

4.6 Typical Miniature Joule-Thomson Cooler Specification

The miniature type of Joule-Thomson cryocooling systems which are designed with specific operational attributes in mind are identified by the following distinctive features:

- a) Operational Pressure
- b) Evacuated Cryochamber or Dewar
- c) A Long Heat Exchanger
- d) Low Heat Capacity
- e) Coolants
- f) High Purity Gases
- g) Criteria of performance
- h) Operational Conditions

Specifications of developed JT cooler prototype

- Cool down time at 100K < 15 Secs
- Temperature stability $\pm 1K$
- Initial gas consumption < 160 NLPM
- Steady-state gas consumption < 8 NLPM
- Weight < 15 grams (approx.)





Figure 4.10 (a) Developed Prototype of JT Cryocooler (b) Prototype in a glass dewar

THERMAL ANALYSIS AND PROTOTYPE DEVELOPMENT OF MINIATURE STIRLING CRYOCOOLER

5.1 Description of Stirling Cryocooler

The cooler choice is based on application requirements like cool-down temperature, time, detector load, efficiency, life, and operating temperatures. Based on these application-based requirements, in addition to the JT cryocooler, the Stirling cryocooler is the other preferred system for detector cooling. There are in principle two kinds of Stirling coolers, rotary and linear motors. Rotary means when the motion available is rotary which is further converted into reciprocating motions. These can be split where the cold side is separated from the compressor side with a connecting duct and integral means these are integral with the compressor as shown in Fig. 5.1. The integral rotary coolers are known for their small size, less weight, high efficiency and faster cooling and highly reliable operation.

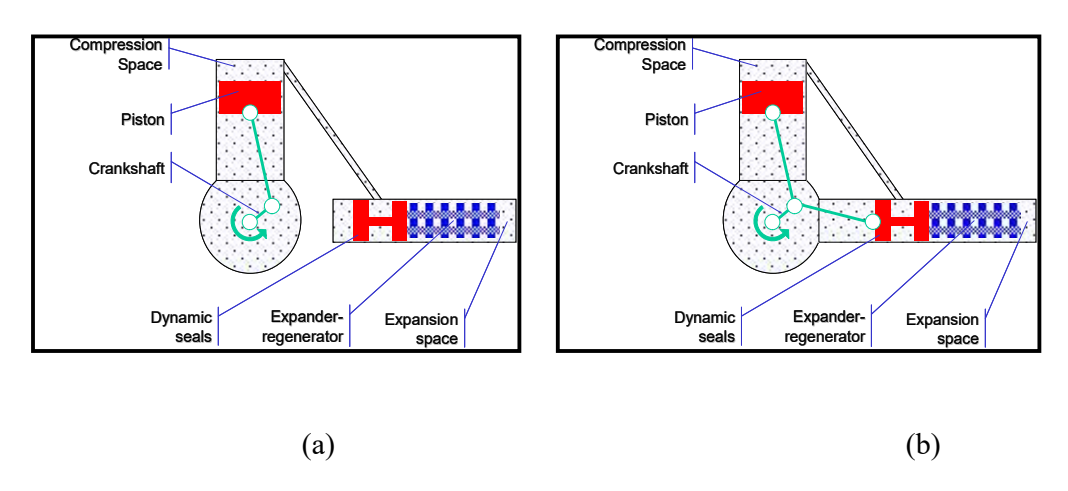


Figure 5.1. Stirling coolers (a) split type (b) integral type

The Stirling cryocooler operates using the Stirling cycle principle. The P-V and T-S diagrams for the ideal theoretical Stirling cycle are shown in Fig. 5.2

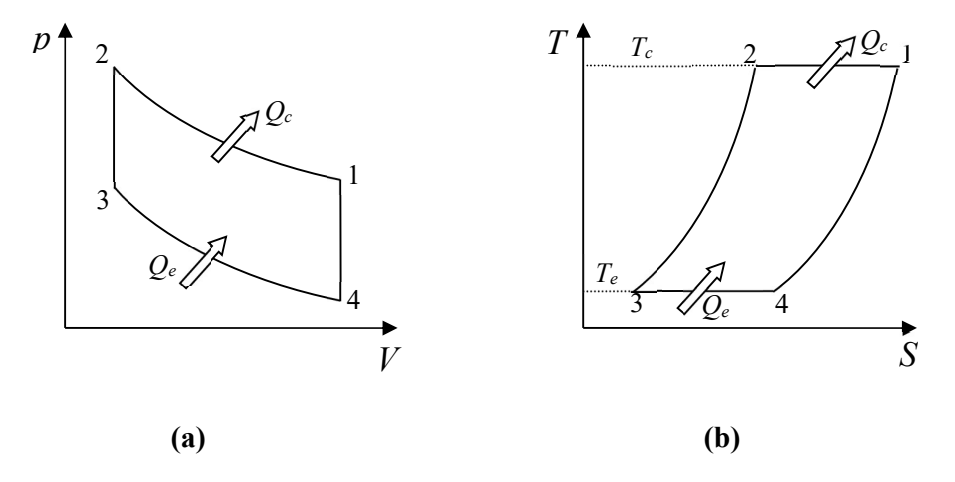


Figure 5.2. Ideal Stirling cycle: (a) P-V diagram (b) T-S diagram

An ideal Stirling cycle comprises a compression volume, a regenerator, and an expansion volume as per Figure 5.3.

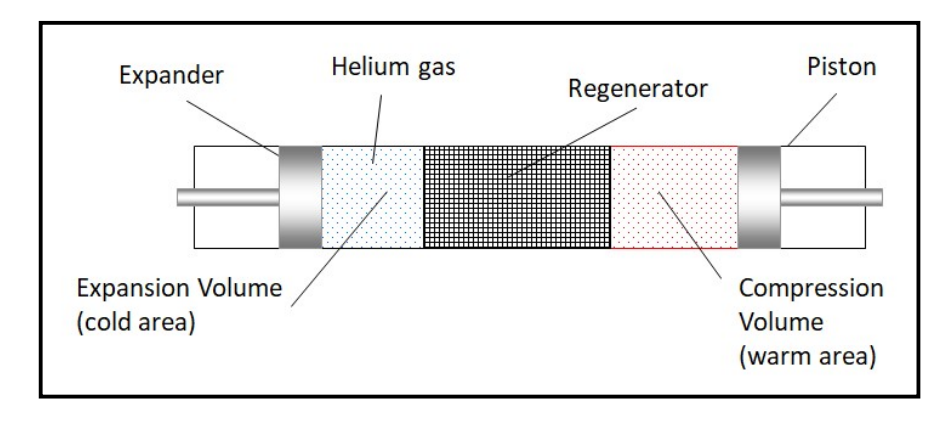


Figure 5.3. Schematic representation of Stirling refrigerator

Fig. 5.4 illustrates the stages of the ideal Stirling cycle. In this process, 1 to 2 is isothermal compression where the piston moves but the expander stays still and the generated heat is released at a constant temperature. 2-3 is constant volume cooling of the gas to the cryogenic temperature. Whereby both the piston and expander move simultaneously to maintain constant volume conditions. 3-4 the piston stops but the expander moves further and the gas is expanded, heat is taken from the space to be cooled. Finally, both the piston and expander move to the right to complete the 4-1 constant volume process whereby the gas is again heated by the energy earlier stored by the regenerator. The regenerator works like a thermodynamic sponge alternatively storing the heat and again giving this back to the gas.

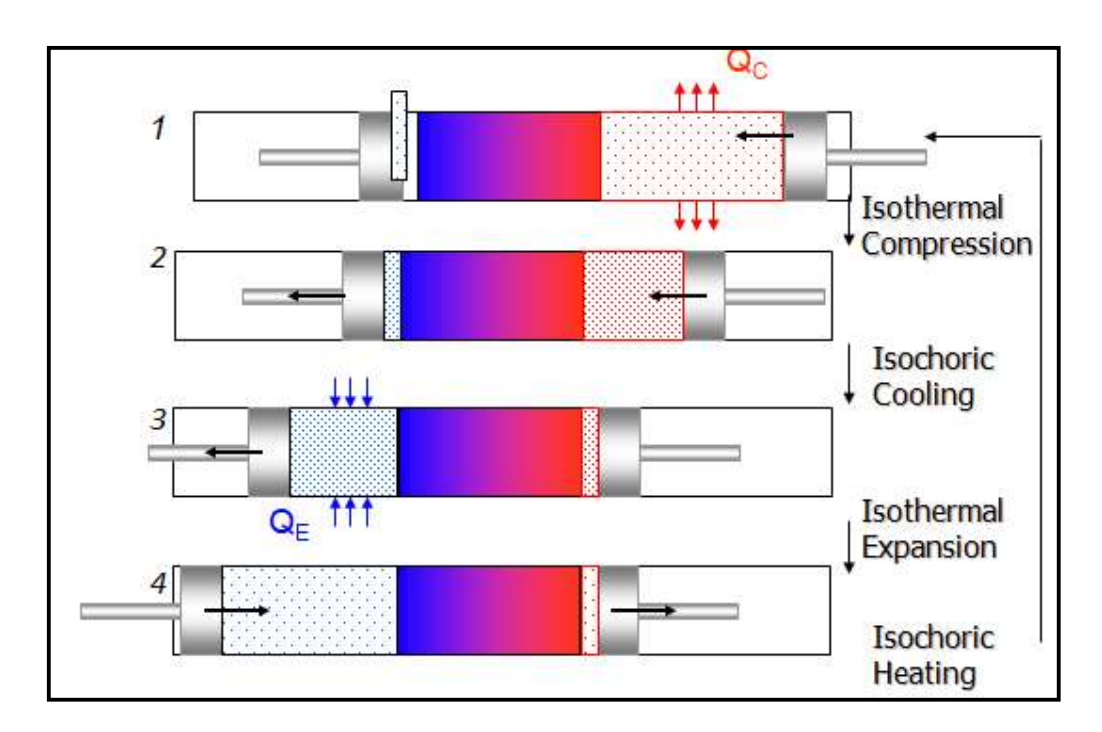


Figure 5.4 Processes of an Ideal Stirling Refrigerator

In an ideal case, the fluid is assumed to remain concentrated at the end of each process, which is very difficult to achieve. In practice, the cooler operates with a sinusoidal motion of the reciprocating elements with a phase lag between the compressor and expander motions since this motion can be achieved with much ease as shown in Fig. 5.5.

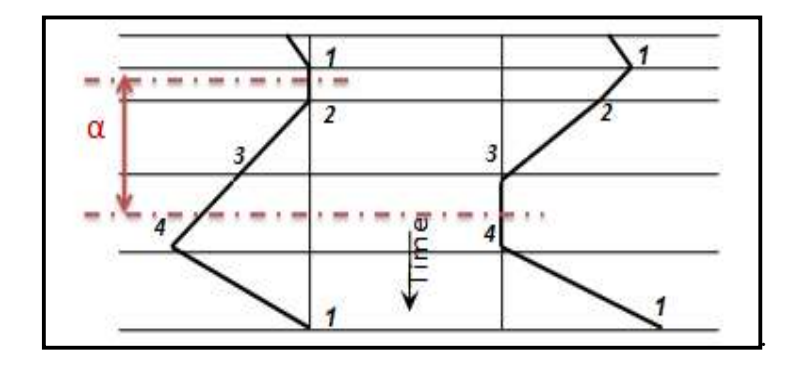


Figure 5.5 Ideal Stirling cycle phase diagram

5.2 Thermodynamic Analysis

The cooler is analyzed using the first-order thermodynamic assessment without taking the actual losses associated with the cycles. Several assumptions made include the perfect regeneration, uniform instantaneous pressure, p, throughout the system, linear temperature profile in dead space, fixed mass of working fluid, and uniform and fixed temperature of each space. The expansion volume, V_{exp} at any instant, is represented as the swept volume of the expansion side, V_{Exp} , and is represented by Singh et al. [82]

$$V_{\text{exp}} = \frac{1}{2} V_{\text{Exp}} (1 + \cos \emptyset) \tag{5.1}$$

volume deviation of compression space is defined as the piston and regenerator cum displacer having a phase lag α , then

$$V_{exp} = \frac{1}{2}kV_{Exp}(1 + \cos(\phi - \alpha))$$
 (5.2)

Where κ is represented by V_{comp}/V_{exp} .

The periodic refrigeration produced or the expansion side heat removal Q_{exp} is describe as V_{Exp} , p_{mean} , intermediary parameters θ and δ , and is represented by Yang et al [104] as:

$$Q_{exp} = \frac{V_{exp} \cdot p_{mean} \cdot \delta \cdot \pi \cdot sin\theta}{\left[\sqrt{(1-\delta^2)} + 1\right]}$$
(5.3)

Here the parameter θ can be represented as

$$\theta = tan^{-1} \frac{k.\sin \alpha}{\tau + k.\cos \alpha} \tag{5.4}$$

The constant τ is represented as $\frac{T_{comp}}{T_{exp}}$ and

$$\delta = \frac{\sqrt{\tau^2 + k^2 + 2.\tau \cdot k + 2S}}{\tau + k + 2S} \tag{5.5}$$

In this equation, the constant S is the reduced dead volume which is represented as

$$S = \frac{2X\tau}{\tau + 1} \tag{5.6}$$

Where $X = \frac{V_{nsw}}{V_{Exp}}$, dead volume ratio; V_{nsw} is total non-swept volumes. Also, the

pressure, p at an instance, is represented with, p_{max} , and is represented as follows.

$$p_{inst} = \frac{p_{max}(1-\delta)}{[1+\delta.\cos(\phi-\theta)]}$$
 (5.7)

Where the p_{max} , is defined as

$$p_{max} = p_{mean} \sqrt{\frac{1+\delta}{1-\delta}} \tag{5.8}$$

Taking the combined swept volume V_T and considering eq (5.3), (5.7), and (5.8), a term cyclic dimensionless heat extracted, $Q_{exp}^* = \frac{Q_{exp}}{p_{max} \cdot V_T}$ represented as

$$Q_{exp}^* = \frac{\pi (1-\delta)^{1/2} \cdot \delta \cdot \sin\theta}{(1+k) \cdot (1+\delta)^{1/2} \cdot \left[1 + (1-\delta^2)^{1/2}\right]}$$
(5.9)

The term W, work done on the system can be defined as

$$W = Q_{comp} - Q_{exp} = (\tau - 1). Q_{exp}$$
 (5.10)

Where the term Q_c , the heat rejected by the system can be represented as

$$Q_{comp} = \tau. Q_{exp} \tag{5.11}$$

The *COP ideal* is defined as:

$$COP_{ideal} = \frac{Q_{exp}}{W} = \frac{1}{\tau - 1} = \frac{T_{comp}}{T_{comp} - T_{exp}}$$

$$(5.12)$$

Likewise, Eq. (5.9), W* can be represented by using Eq. (5.10) and written as:

$$W^* = (\tau - 1). Q_{exp}^* \tag{5.13}$$

5.3 Sample calculation to determine the compressor piston and regenerator tube sizes

Given Data: $Q_{Exp} = 0.5$ Watt, $T_{Exp} = 80$ K, $T_{Comp} = 300$ K

Assumed Data: Dead volume ratio, $X = \frac{V_{nsw}}{V_{Exp}} = 3$, Swept volume ratio, $k = \frac{V_{Comp}}{V_{Exp}} = 3.5$

Temperature Ratio,
$$\tau = \frac{T_{Comp}}{T_{Exp}} = \frac{300}{80} = 3.75$$

Mean temperature, $T_{\text{mean}} = \frac{T_{Exp} + T_{Comp}}{2} = 190 \text{ K}$

$$S = \frac{(2X\tau)}{(\tau+1)} = 4.736$$

$$A = \sqrt{(\tau^2 + 2\tau k \cos \alpha + k^2)} = 5.1295$$

$$B = (\tau + k + 2s) = 16.722$$

$$\delta = \frac{A}{B} = \frac{5.1295}{16.722} = 0.3067$$

Instantaneous pressure, $p_{exp} = \frac{k}{B[\delta\cos(\emptyset - \theta) + 1]}$

For
$$p_{min}$$
, $\emptyset = \theta$ $p_{min} = \frac{k}{B[\delta+1]} = 16$ bar

For
$$p_{max}$$
, $\emptyset = (\theta + \pi)$, $p_{max} = \frac{k}{B[\delta - 1]} = 30.19$ bar

Mean cycle pressure,
$$p_{mean} = p_{max} \sqrt{\frac{1-\delta}{1+\delta}} = 22 \text{ bar}$$

$$Q_{Exp}\!=\!\!\frac{V_{Exp}\,\pi\,p_{mean}\,\delta\,sin\theta}{1\!+\!\sqrt{1\!-\!\delta^2}}\ therefore,$$

$$V_{Exp} = \frac{Q_{Exp} + [1 + \sqrt{1 - \delta^2}]}{\pi p_{mean} \delta \sin \theta} = 46.03 \text{ mm}^3$$

Now,
$$V_{Exp} = 46.03 \text{ mm}^3$$

$$\frac{\pi}{4} d^2 (1) = 46.03 \text{ mm}^3$$

Hence, Regenerator diameter (d) = 7.65mm

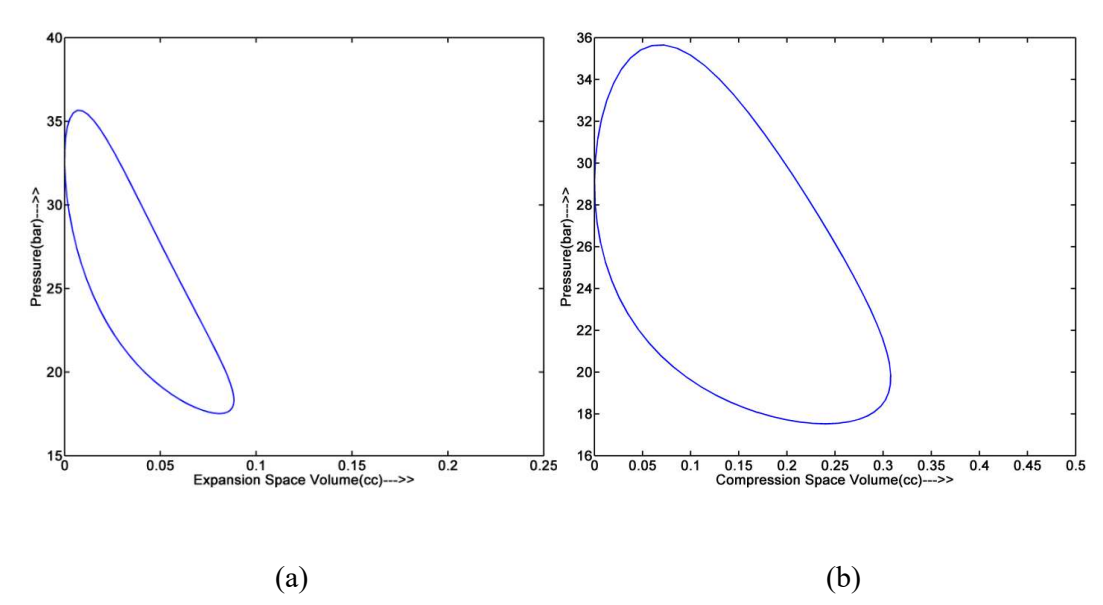
$$k = \frac{V_{Comp}}{V_{Exp}}$$
, So, $V_{Comp} = k(V_{Exp}) = 161.1 \text{ mm}^3$

Now,
$$V_{Comp} = 161.1 \text{ mm}^3$$

Hence, Compressor diameter (D) = 14.32 mm

5.4 Calculations for Design Optimization

Numerical calculations have been carried out to analyze various design factors of cryocooler's performance. In the analysis, only the parameter of interest has been varied keeping the other parameters the same. Figs 5.6 (a) and 5.6 (b) show the theoretical *p-v* graph for the expansion and compression spaces volume respectively, whereas Fig. 5. 6 (c) shows the net *p-v* graph. The area of these diagrams depicts the amount of heat extracted and the work done. The corners of the curves are not sharp due to the consideration of continuous sinusoidal motion.



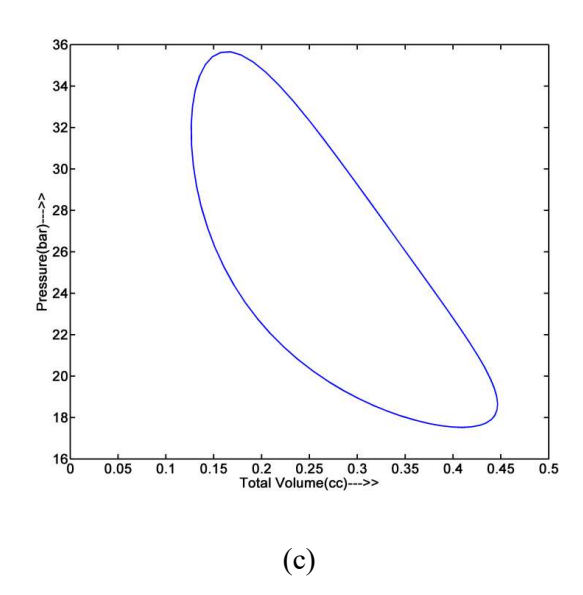


Figure 5.6 Theoretical P-V curve for cryocooler (a) Expansion space (b) Compression space (c) Total working space

In Fig 5.7 (a) and 5.7 (b), the non-dimension refrigeration produced and cyclic workout on α and κ are represented for various ratios of dead volume in the cycle. The ideal heat extraction exists at a phase angle of 100° , and the dead volume fraction raises the periodic refrigeration produced and descends with a phase angle of 90° . Also, refrigeration produced varies by only $\pm 10\%$ when the phase angle lies from 60° to 110° . So for the ease of manufacturing 90° arrangement is preferred.

The predicted ideal cooling capacity variation with speed for different charge pressures for the IDCA cooler has been shown in Fig. 5. 7(a). It can be pointed out that increasing these parameters linearly increases the ideal cooling capacity. Figure 5. 7(b) shows the abrupt reduction in heat extracted with decreasing expansion temperature T_e , presuming a constant compression temperature for various swept volume ratios. A clear optimum exists for the value of κ as 3.5, which is near the selected value in the present case for T_e equal to 80K.

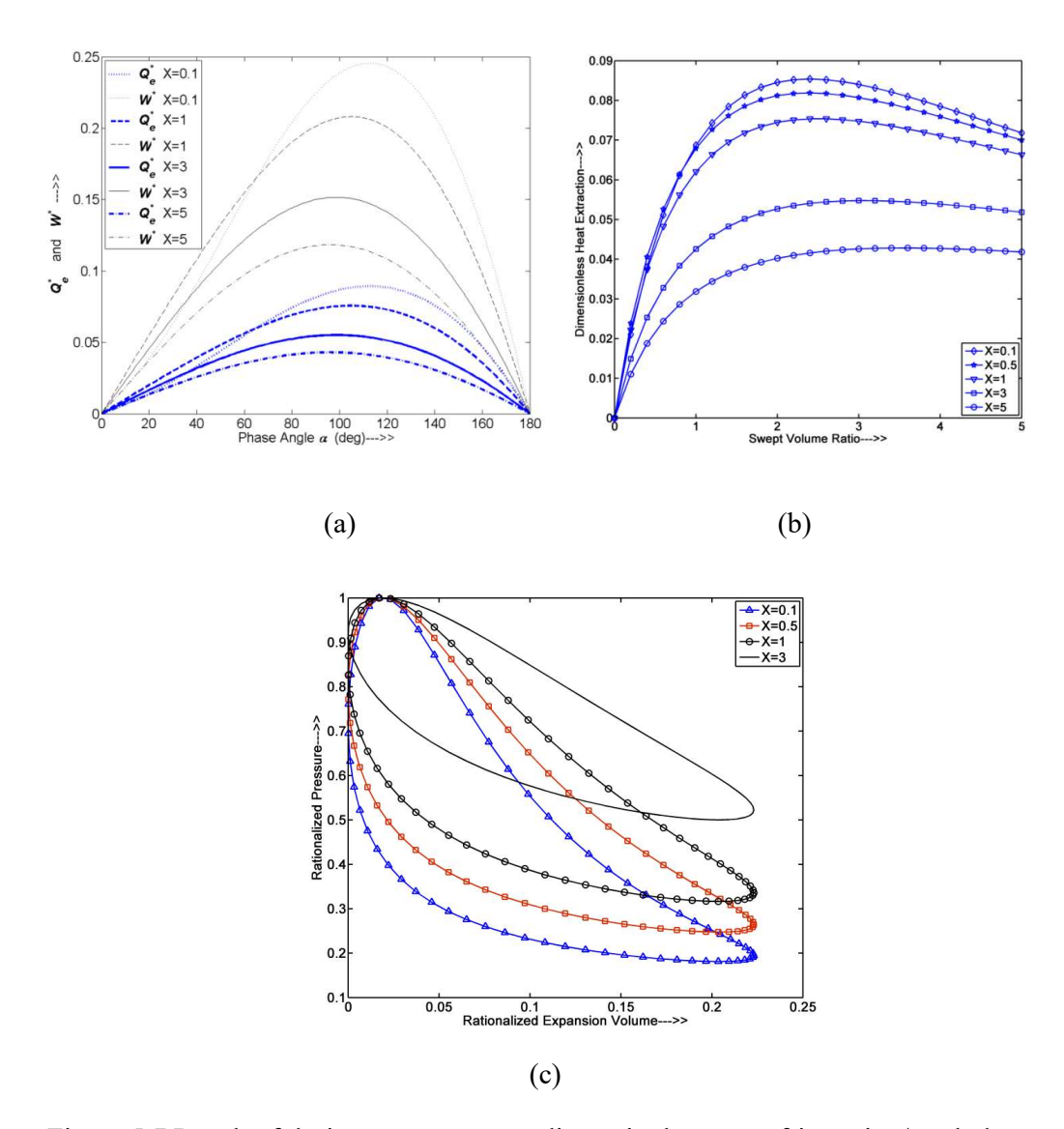


Figure 5.7 Result of design parameters on dimensionless net refrigeration/work done for different dead volume ratios X: (a) α (b) κ (c) dead volume ratios.

5.5 Loss Evaluation of System

The losses in the system are not considered in the theoretical analysis. However, practically there are losses due to the non-ideality present in the system. Considering these losses is essential for the estimation of the actual cooling capacity. These losses affect the refrigeration produced. Considering the losses, COP_{actual} , is represented as:

$$COP_{actual} = \frac{Q}{P} \tag{5.14}$$

Here Q is the refrigeration capacity considering the losses and P is the power input corresponding to the actual cycle. The Carnot efficiency estimates the numerical value of the ideal to the real behavior of the system:

$$n_{Carnot} = \frac{COP_{actual}}{COP_{actual}} \tag{5.15}$$

From Eq. (5.12), with a temperature of $T_c = 300K$ and $T_e = 80K$

$$COP_{Ideal} = \frac{80}{(300-8)K} = 0.36$$

For the calculation of the actual COP, taking 0.5W as net refrigeration capacity and the power input as 15W

$$COP_{actual} = \frac{0.5}{15} = 0.033$$

Carnot efficiency from Eq. (5.15),

$$n_{carnot} = \frac{0.033}{0.36} = 0.092$$

Hence, it is necessary to calculate the losses to design an efficient cryocooler. The losses are categorized as [105]:

- 1. Losses responsible for consuming the input power for cooling as motor coil windage heating and irreversibility associated with compression space.
- 2. Losses consuming a fraction of the cold produced, and are related to the refrigeration space.

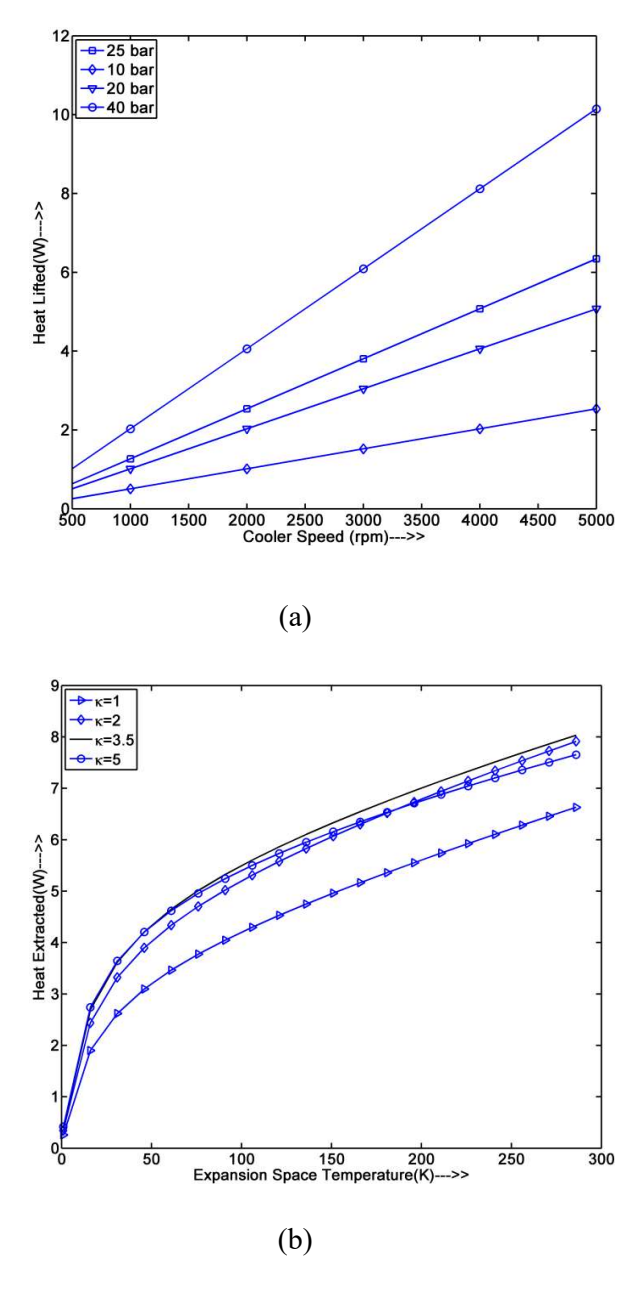


Figure 5.8 (a) Variation of Cooler speed vs heat lifted (b) variation of heat extracted vs temperature in expansion space

The available refrigeration at the expander end may be estimated as:

$$Q_{net} = Q_{max} - \sum Losses \tag{5.16}$$

$$Q_{net} = Q_e - \frac{(Q_{ief} + Q_{\Delta pf} + Q_{rt} + Q_{cmg} + Q_{shtl} + Q_{dewar})}{Regenerator \ Losses}$$
 (5.17)

Where Q_{net} is available refrigeration, Q_{max} is maximum available refrigeration, Q_{ief} is the ineffectiveness thermal loss, Q_{pf} is pressure drop loss due to friction, Q_{rt} is axial conduction loss, Q_{cmg} is the regenerator loss, Q_{shtl} is the shuttle loss and Q_{cf} are and Dewar losses.

5.5.1. Regenerator Ineffectiveness Loss

Due to regenerator inefficiency, the temperature of the gas leaving the cold tube is higher than the regenerator material. This kind of loss is defined by Miyabe et al [106] as:

$$Q_{ief} = m \cdot C_{p.} (T_{comp} - T_{exp}) \cdot (1 - \varepsilon)$$
 (5.18)

Where $\dot{m}=$ mass flow rate and $C_p=$ specific heat. The effectiveness of the heat exchanger is defined by Pande et al. [107] as:

$$\varepsilon = \frac{Ntu(1-\lambda)}{1+Ntu} \tag{5.19}$$

Where Ntu is the number of heat transfer units as

$$Ntu = \frac{h_m \cdot A}{m \cdot C_p}$$

The heat transfer coefficient is estimated as

$$h = \frac{k_f \cdot N_{ud}}{d_m} \tag{5.20}$$

Reynolds number is given as

$$R_{ed} = \frac{d_m u}{u} \tag{5.21}$$

5.5.2. Pressure Drop Loss

The loss due to the pressure drop is calculated by the across the regenerator matrix flow resistance which reduces the expansion pressure. The loss is defined as

$$\nabla p_f = f. \, \rho. \, u^2. \, n/2 \tag{5.22}$$

The friction factor *f* is estimated as:

$$f = \frac{33.6}{Re_1} + 0.337 \tag{5.23}$$

Where Re_l is defined as

$$Re_l = \frac{l_m \cdot u}{v} \tag{5.24}$$

The pressure drop loss is calculated as:

$$Q_{\Delta pf} = \frac{Q_e \cdot \Delta p_f}{pa} \tag{5.25}$$

where pa is defined as compression ratio as

$$Pa = P_{mean} \frac{r-1}{r+1}$$
 (5.26)

5.5.3. Longitudinal Conduction Loss

Axial conduction along the regenerator is represented below:

$$Q_{rt} = \frac{k_m \cdot A_t \cdot (T_{comp} - T_{exp})}{l_r}$$
 (5.27)

Axial conduction through regenerator material and can be estimated as:

$$Q_{cmg} = \frac{k_{eff}.A_{eff}.(T_{comp} - T_e x p)}{l_r}$$
 (5.28)

Where k_{eff} is given as

$$k_{eff} = k_f \cdot \frac{(1 + k_m/k_f) - (1 - \emptyset) \cdot (1 - k_m/k_f)}{(1 + k_m/k_f) + (1 - \emptyset) \cdot (1 - k_m/k_f)}$$
(5.29)

And A_{eff} is defined as:

$$A_{eff} = A_r(1 - \emptyset)$$

5.5.4. Regenerator Efficiency

The efficiency of the regenerator is defined as

$$\Psi = 1 - \frac{Q_{tr}}{Q_{st}} \tag{5.30}$$

Where Q_{tr} is the total of regenerator losses and Q_{ts} is defined as heat-stored

$$Q_{ts} = m_{\cdot}C_{p\cdot}(T_{comp} - T_{exp}).\varepsilon$$
 (5.31)

5.5.5. Shuttle Heat Transfer Loss

This loss is defined as convective heat transfer due to the motion of the regenerator within the cold tube [108]. It can be estimated as [109]

$$Q_{shtl} = \frac{k_f.\pi.d_r.s_l^2.(T_{comp} - T_{exp})}{(5.4).C.l_r}$$
 (5.32)

Where s_l is the length of the stroke and radial clearance is c.

5.5.6. Dewar Losses

Dewar losses are the sum of the conductive and radiative losses in the cold-finger. The conduction losses are due to the temperature difference between both ends of the cold tube end. One end is maintained at 80K and the other is at room temperature. The radiation losses are due to the radiation heat between the inner and outer surfaces of the Dewar vessel. The convection losses in the Dewar can be minimized by maintaining a high vacuum of the order of 10^{-7} milli-bar.

5.6 Analysis Results

The regenerator design and losses can be optimized by analytical analysis. The design methodology is represented in Fig. 5.9. Mesh sizes (100 to 500 no.) have been analyzed. Stainless Steel is selected for wire mesh due to its moderate thermal properties. Different regenerator losses are represented in Fig. 5.10(a) at 400-size mesh. The increase of loss due to the mesh number increase may be mainly attributed to the increase in fluid velocity through the matrix because of the corresponding decrease in porosity. Moreover, the total losses are minimal in the 35-45 mm range. Fig 5.10(b) shows the increase of pressure drop losses with the increasing length and mesh number. The effectiveness increases with increasing length, as shown in Fig. 5.11(a), due to the larger area available for heat transfer. It is observed that the effectiveness increases with an increase in mesh number with initial length and later converges for all the mesh sizes due to the reduced thermal gradient. Any length between this zone may be chosen depending on the other constraints based on configuration and weight. Fig. 5.11 (b) shows the efficiency variation with regenerator length. The graph shows that in the given length of the regenerator between 30-40 mm, the efficiency is maximum with 500 No mesh size.

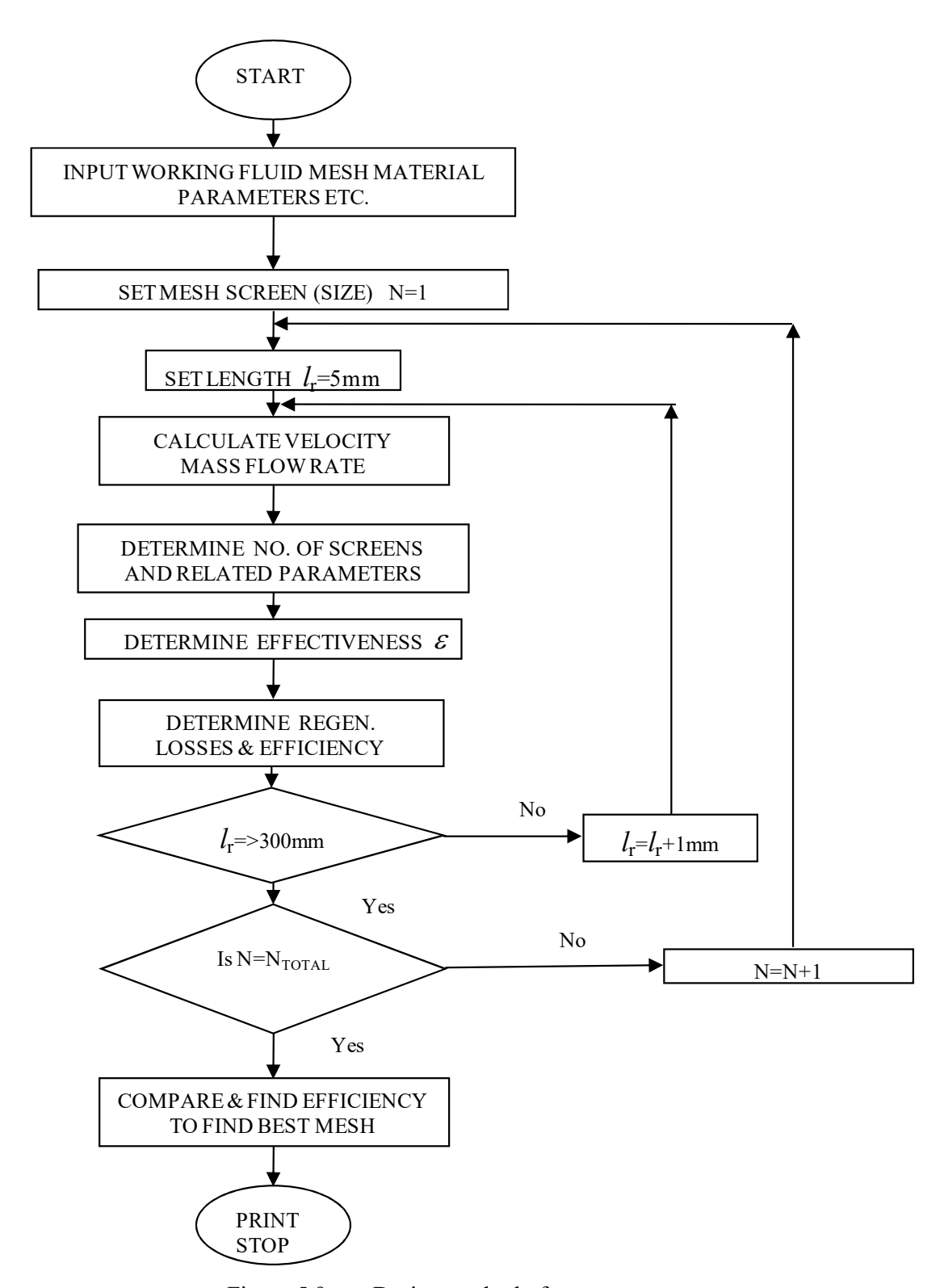


Figure 5.9 Design method of regenerator

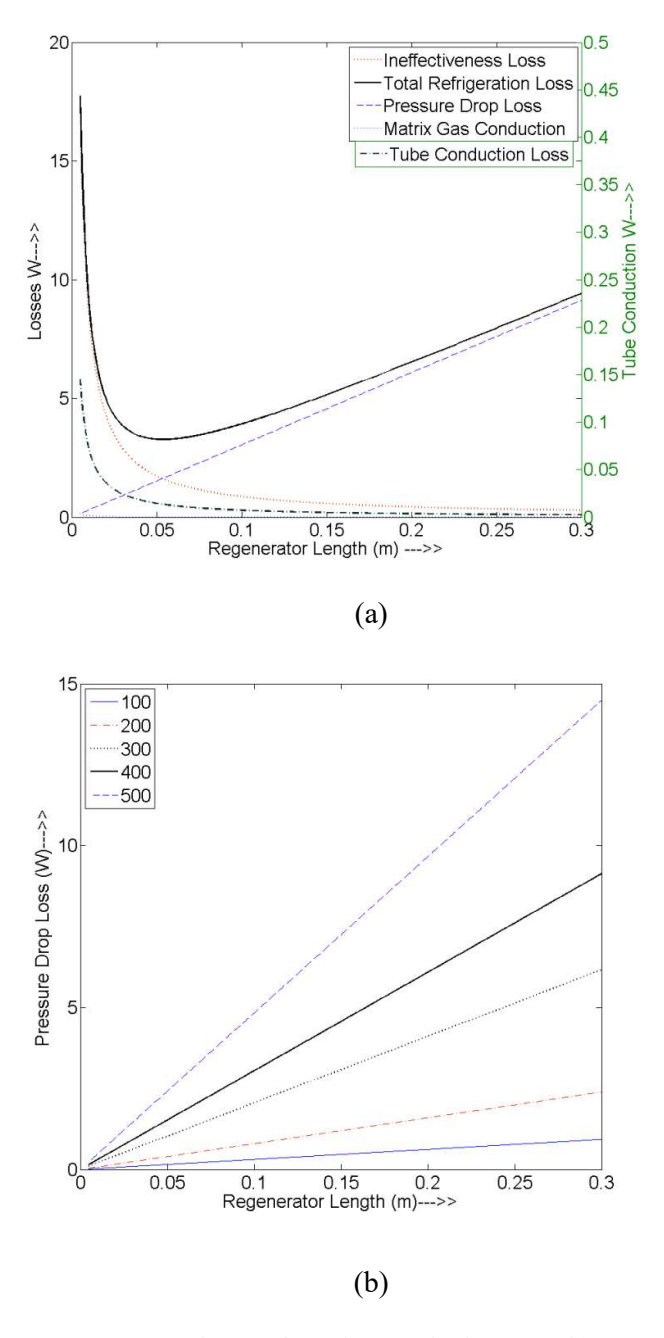


Figure 5.10 (a) Regenerator losses for wire mesh size 400 (b) Pressure drop loss

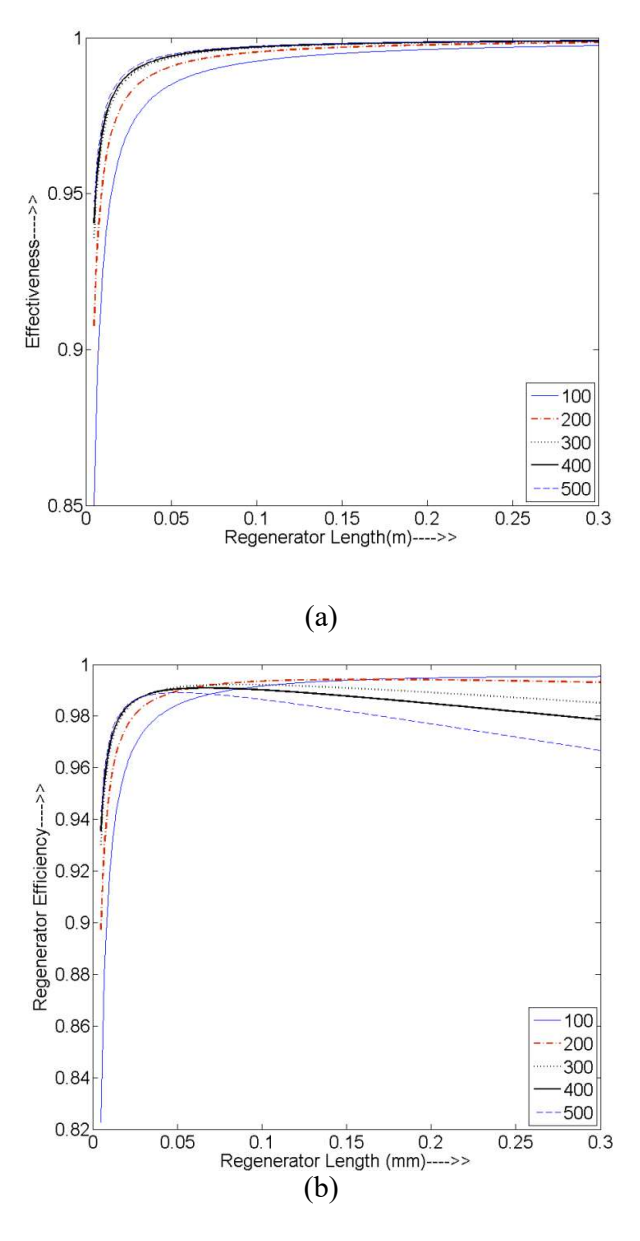


Figure 5.11 (a) Effectiveness of regenerator with length (b) Efficiency of regenerator vs length

The increase in total dewar heat load with rising ambient temperature is shown in Fig. 5.12(a) for different cold-tip temperatures and Fig. 5.12(b) depicts the individual losses for the cold tip at 80K. The radiation losses although less in magnitude, increase more steeply due to their proportionality to the fourth power of temperature. It assumes equal importance in small-capacity cryocoolers where a small amount of cooling power is

left over for cooling actual load, as is in the present study.

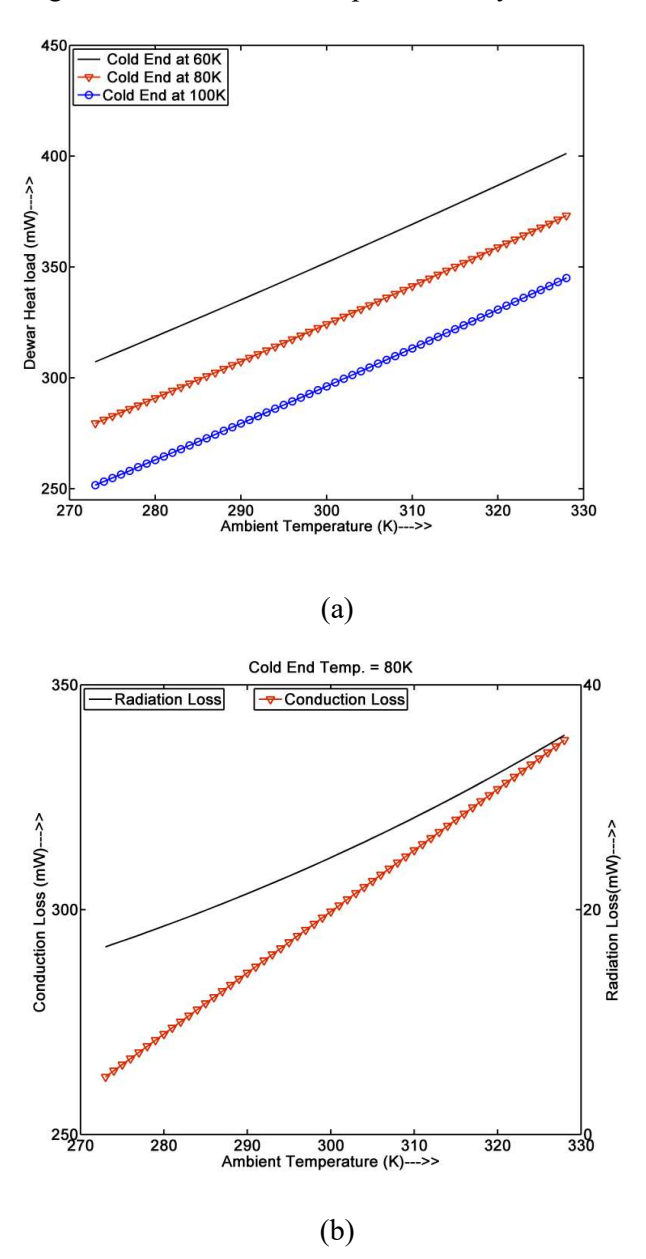


Figure 5.12 (a) Convective and Conductive heat load for different cold-tip temperatures (b) Conduction and radiation losses for cold-tip, radiation loss on second Y-axis.

Fig 5.13 shows the effect of stroke length on shuttle heat loss considering different radial clearances between the regenerator and cold finger. These losses may be minimized by selecting shorter stroke lengths and larger clearances subject to the

constraints imposed by other previously discussed governing factors. Also, increasing the clearances increases appendix losses, through which the fluid gas from the cold region directly starts mixing with the gas from the hot region, thereby reducing the refrigeration available.

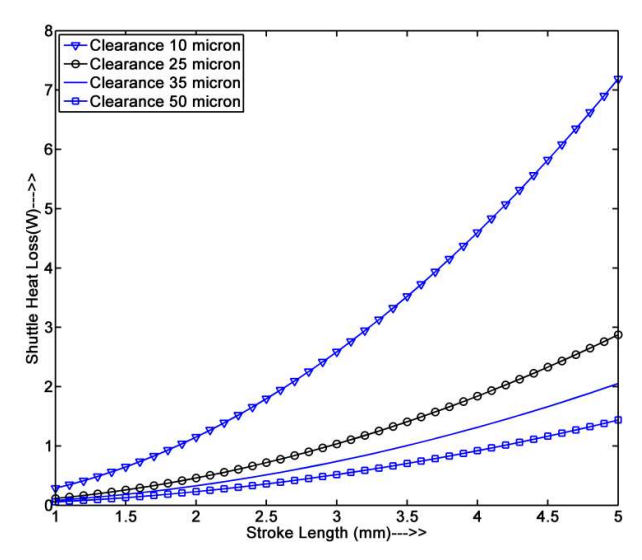


Figure 5.13 Shuttle heat transfer loss as a function of stroke length for various radial clearances

A heat balance sheet for the Stirling cryocooler has been presented in Table 5.1.

Table 5.1 Heat balance of Stirling cryocooler

Regenerator ineffectiveness loss, Q_{ief}	2.26 W
Pressure drop loss, $Q_{\Delta pf}$	1.15 W
Regenerator longitudinal conduction, Q_{rt} + Q_{cmg}	0.04 W
Shuttle heat loss, Q_{shtl}	0.33 W
Dewar heat load, Q _{dewar}	0.32 W
Total Losses (A)	4.10 W
Ideal heat Extracted Q_e (B)	5.07 W
Available Refrigeration $Q_{net}(C=B-A)$	0.97 W
Actual cooling requirement for detector (D)	0.20 W
Losses unaccounted for (C-D)	0.77

A generic flowchart highlighting the computational modelling approach for Stirling cryocooler simulation is shown in Fig. 5.14.

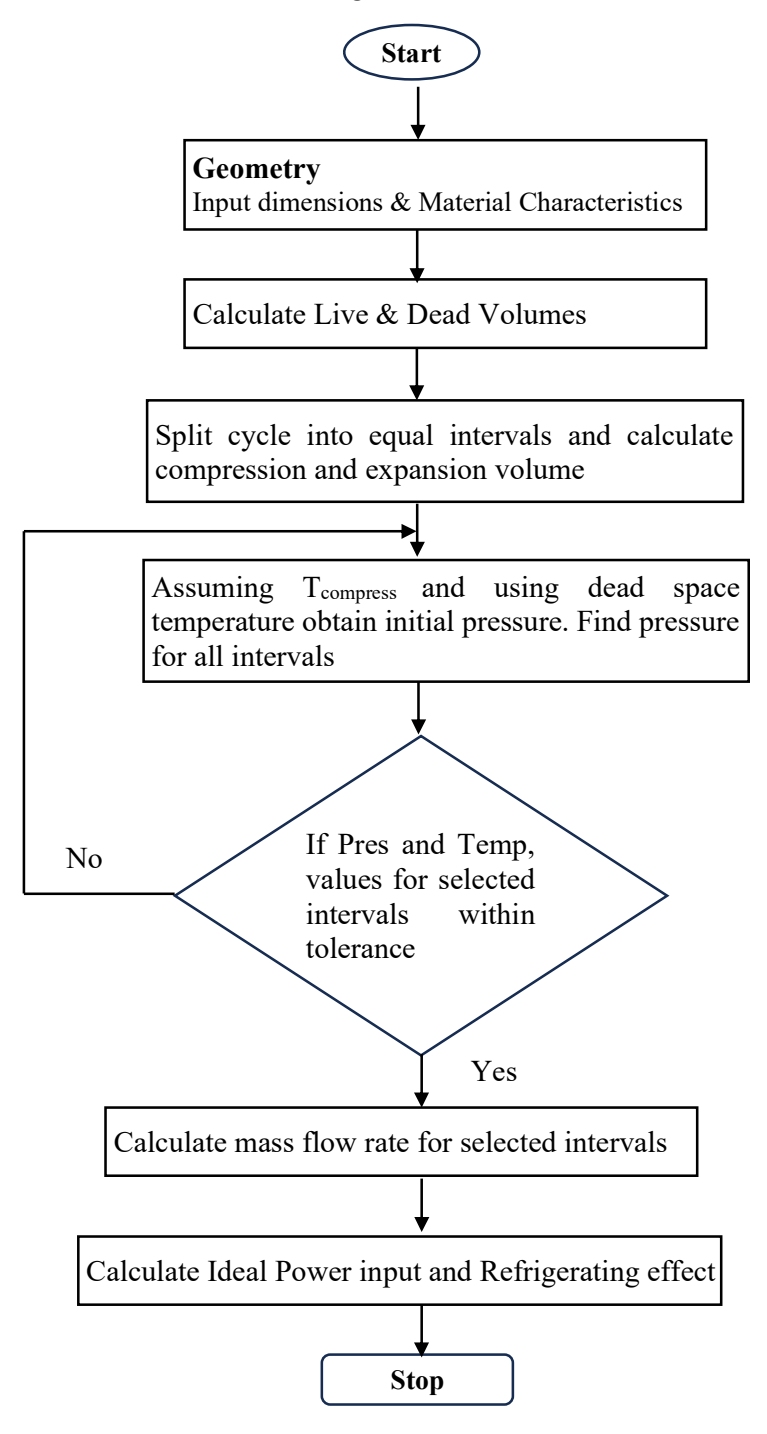


Figure 5.14 Generic Flow chart for computational modelling of Stirling cooler

5.7 Effect of various parameters on Stirling cryocooler design and performance

- 1. Thickness of cold finger and Thermal conductivity of cold finger material
- 2. Coating on Piston of cryocooler

5.7.1 Effect of thickness and material thermal conductivity on Cold Finger Design

Q (heat transfer Rate) =
$$\frac{KA(T_{hot} - T_{cold})}{L}$$
 (Watt) where, $k = \frac{W}{m}$. k (5.33)

 $A = Cross - sectional area (m^2);$

 $T_{hot} = High temp(k)$

 $T_{cold} = Low \ temp \ (k);$

L = Length of cold finger (m);

t = cold finger thickness (m)

$$Q = K\pi (R^2 - r^2) \frac{(T_{ho} - T_{cold})}{L}$$
 (5.34)

$$= K\pi [R^2 - (R-t)^2] \frac{(T_{ho} - T_{cold})}{L} = K\pi [2Rt - t^2] \frac{(T_{hot} - T_{cold})}{L}$$
 (5.35)

Taking, $2Rt - t^2 \approx 2Rt$

$$Q = 2\pi kRt \frac{[T_{hot} - T_{cold}]}{L}$$
 (5.36)

 $Q \propto f(t)$

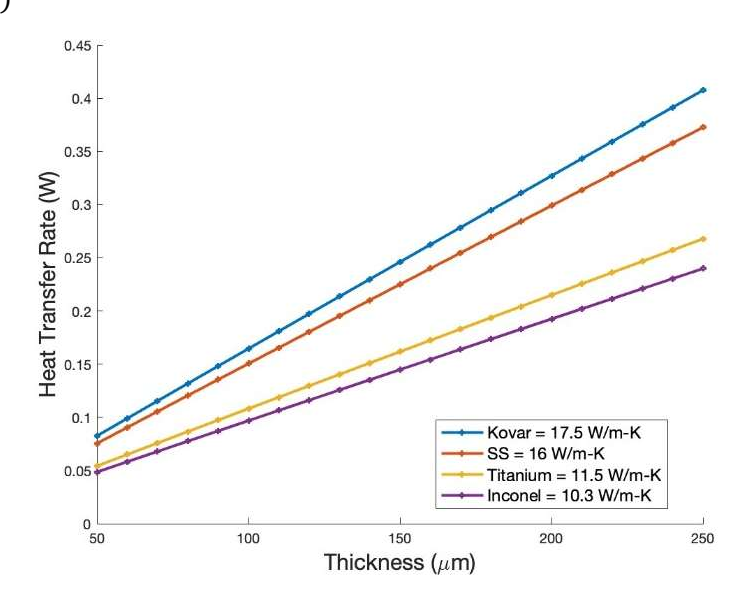


Figure 5.15 Effect of cold Finger Thickness and thermal conductivity on Heat Transfer

Heat transfer must be minimal for maximum cooling at the cold end. Fig. 5.15 shows that heat transfer reduces with the reduction in the thickness of the cold finger and thermal conductivity. Therefore, Inconel is a preferred metal for the cold finger, though titanium is another alternative.

5.7.2 Effect of type of coating on cryocooler pistons

5.7.2(a) Coating methodology

A semi-industrial sputtering system was used for TiN coatings with the effective plasma volume of the sputtering system being 0.005832 m³. The sputtering system mainly consists of a cylindrical double-walled water-cooled vacuum chamber with several ports acting as the sputtering chamber. It houses the magnetron cathodes, the substrate holder, feed-throughs, etc. A high vacuum pumping system with a turbomolecular pump for creating a vacuum in the chamber of the order of 5.6x10⁻⁶ mbar. The coatings were deposited at a substrate temperature in the range of 250-325°C. Plasma Assisted Chemical Vapour Deposition (PACVD) method with magnetron sputtering techniques was used for DLC coating. The processing temperature (< 250°C) at which the material properties of the parent material remain unaffected. The general coating parameters for the deposition of TiN and DLC coatings on the pistons are listed in Table 5.2.

Table 5.2 General parameters for TiN and DLC coating

Parameters	TiN Coating	DLC Coating
Coating Technique	PVD	PACVD
Colour of Coating	Golden Brown	Black
Coating Temperature (°C)	250-325	<250
Friction Coefficient	0.4	0.1
Micro Hardness HV 0.5	691	1173
Thermal Conductivity (W/mK)	19.2	500

A piston cylinder is shown in Fig.5.16. The required thickness of the coating on the piston is within 2-3 μ m and the uniformity of thickness within 1 μ m is a crucial requirement for the maintenance of the part geometry. The parent material before the coating is M42 alloy steel, hardened and ground to a hardness of 55-60 HRC with a surface roughness value of Ra $\sim 0.20~\mu$ m. After coating, the piston-cylinder pair is lapped and polished to the surface finishes of the order of 0.05 μ m Ra. TiN-coated and DLC-coated piston samples are shown in Fig.5.17.

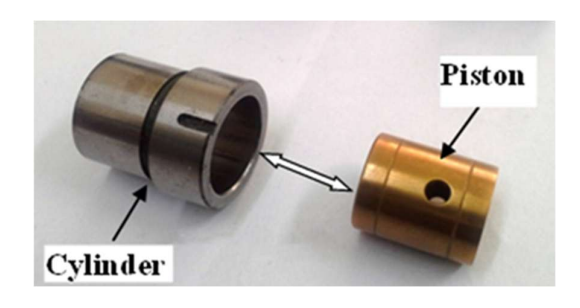
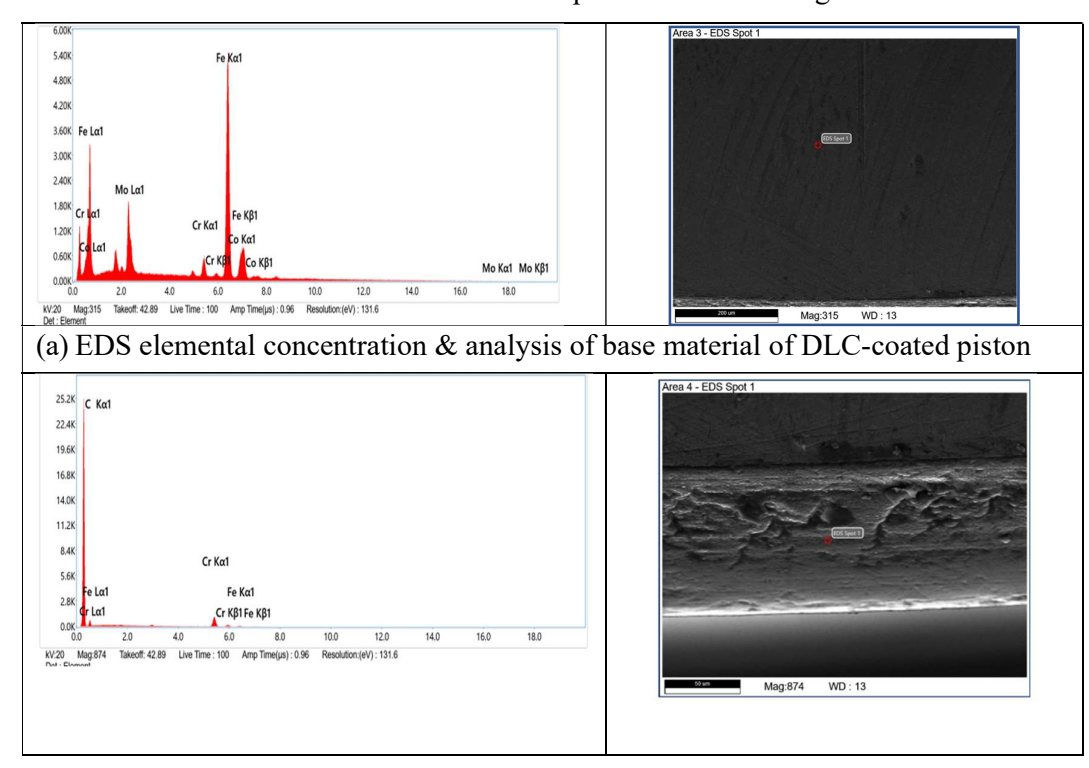


Figure 5.16 Piston and cylinder pair of a Stirling cryocooler

Figure 5.17 Piston samples (1&2-TiN coated, 3 & 4-DLC coated)

5.7.2 (b) Characterization of the coating

The SEM and EDS results of the coated samples are shown in Fig.5.18



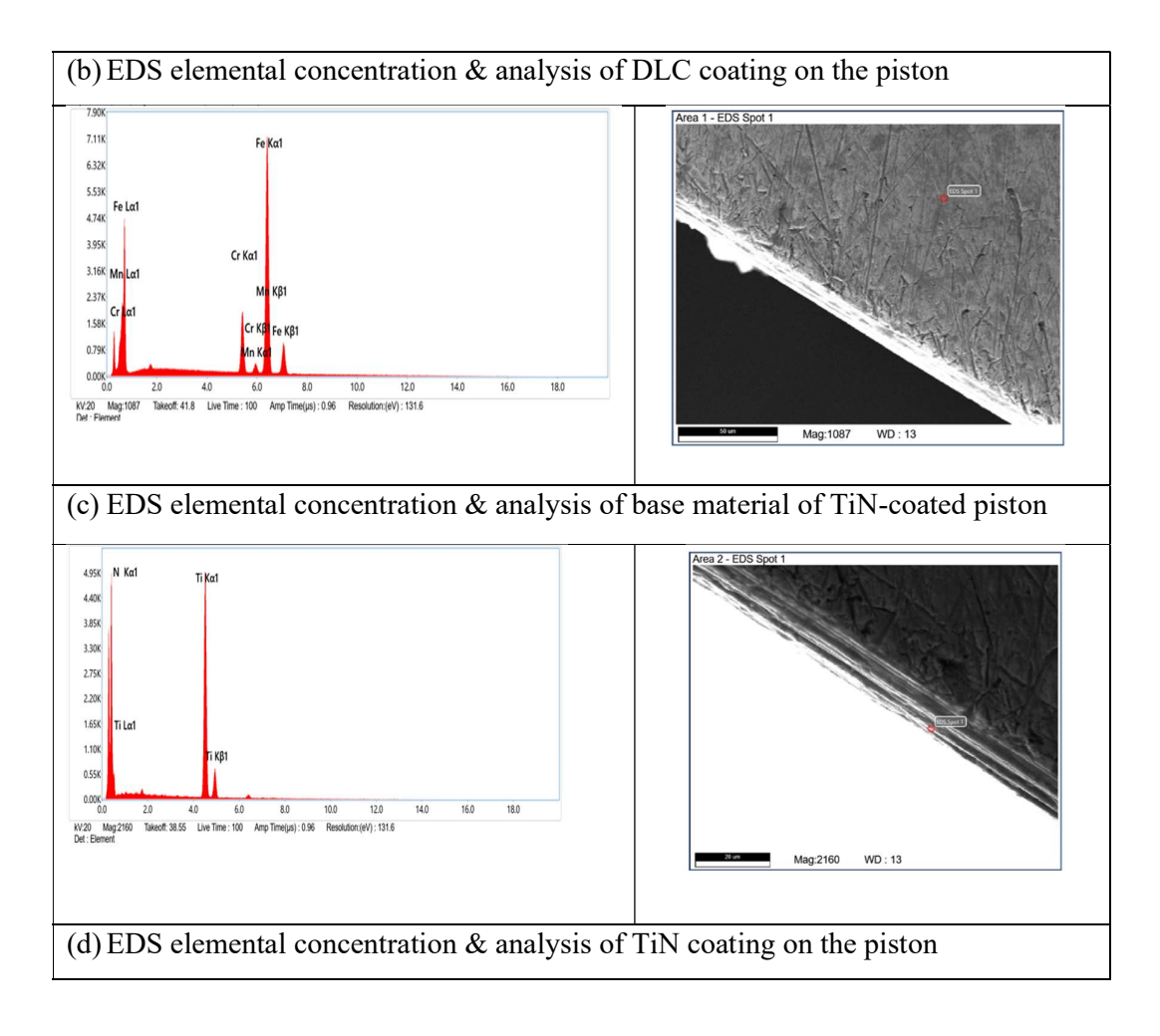


Figure 5.18 EDAX elemental concentration & analysis of base material and both coatings

The SEM micrographs reveal the coatings' morphology, and the coating's chemical composition was evaluated using EDS. In the energy spectrum, as presented alongside the micrographs, the titanium peaks in the coated sample and the carbon peaks in the DLC-coated sample are visible in the test results. The elemental concentration of TiN and DLC coating was identified by a scanning microscope coupled with energy-dispersive X-ray spectroscopy (EDS). EDS analysis with the elemental concentration corresponding to each coating is shown in Tables 5.3 and 5.4.

Table 5.3 Elemental concentration of TiN Sample

Element	N	Ti	Fe
Weight %	19.83	77.56	2.62

The measurements of the sample microhardness were performed using the DURAMIN-40 A2 testing machine. The testing method was VICKERS on HV 0.5 scale and the dwell time was 15 sec. Table 5.5 shows the surface hardness of the TiN and DLC-coated samples. The readings are taken at four different points to consider the repeatability

Table 5.4 Elemental concentration of DLC Sample

Element	С	Cr	Ar
Weight %	74.28	24.57	0.75

Table 5.5 Microhardness of TiN and DLC coated piston on HV0.5 scale

Sample	Mean	Standard deviation
TiN coated	691.92	15.81
DLC coated	1173.29	78.13

Fig. 5.19 shows the indentation imprints made by the diamond indenter on the samples after a 500 gf normal load was applied during the hardness test. The shape of the indentation marks reveals a pile-up in TiN-coated samples, while no such pile-up was observed in DLC-coated samples due to the softer coating.

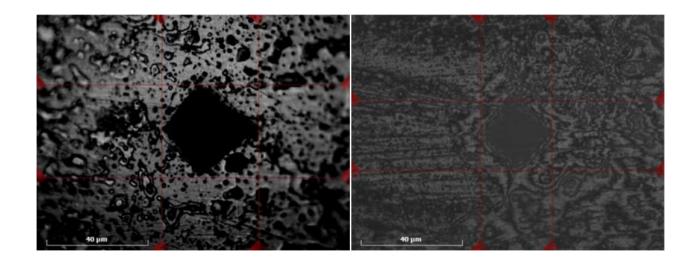


Figure 5.19 Microstructure of TiN & DLC samples after indentation (left to right)

Further, GIXRD measurements were also carried out on the samples. The pattern developed in DLC and TiN-coated samples is shown in Fig. 5.20 (a) and (b) respectively. Phase analysis of the coated samples reveals that the most intense diffraction peaks originate mainly due to the Ti microparticles on the coating surface. On the other hand, the DLC-coated sample shows the presence of the graphite phase

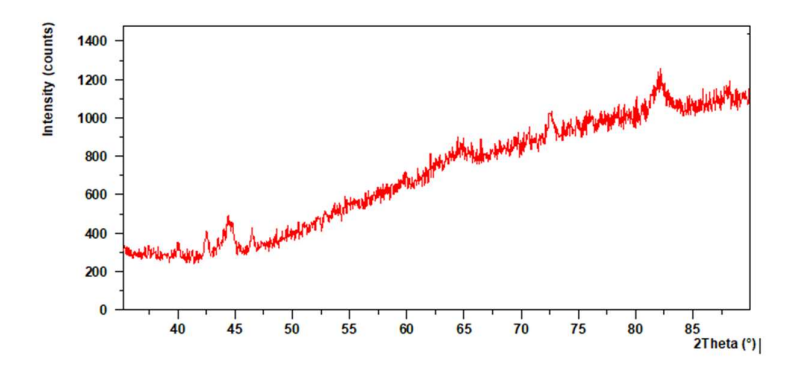


Fig.5.20 (a) Grazing Incidence X-ray diffraction (GIXRD) patterns of DLC-coated Piston

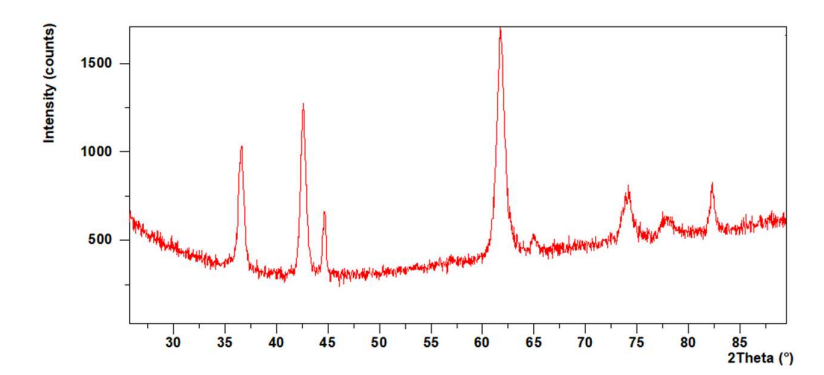


Figure 5.20 (b) Grazing Incidence X-ray diffraction (GIXRD) patterns of TiN-coated Piston

5.7.2(c) Testing of coolers with coated pistons

The cooler 1, after operating satisfactorily initially, showed a gradual increase in power, and its peak value went up to more than 20 Watts along with high audible sound levels (>35 dB). Due to the continuous high power being drawn and a very high audible sound from the cooler, the testing had to be discontinued. A similar pattern was observed for cooler 2, during 37 hours of continuous run. Both the coolers failed to meet the required thermal test specifications and were disassembled to analyse the reasons for the failure and the rise in input power. Visible rubbing and scratch marks on the piston/cylinder appeared to be the most probable reason for failure as the cooler drew a high current and the coating came out as brown powder. The cooler was disassembled to find the reasons for failure, especially for the power rise. The following were the main observations:

- a) A brown powder-like substance could be seen on the components such as the piston & cylinder, crankcase, displacer assembly, etc. Brownish color powder could also be seen on the inner side of the main body
- b) Several rubbing marks were seen on the piston and sleeve assembly which hindered optimal operation as clearance space was filled with powder/debris.
 The piston images before and after assembly are shown in Fig. 5.21

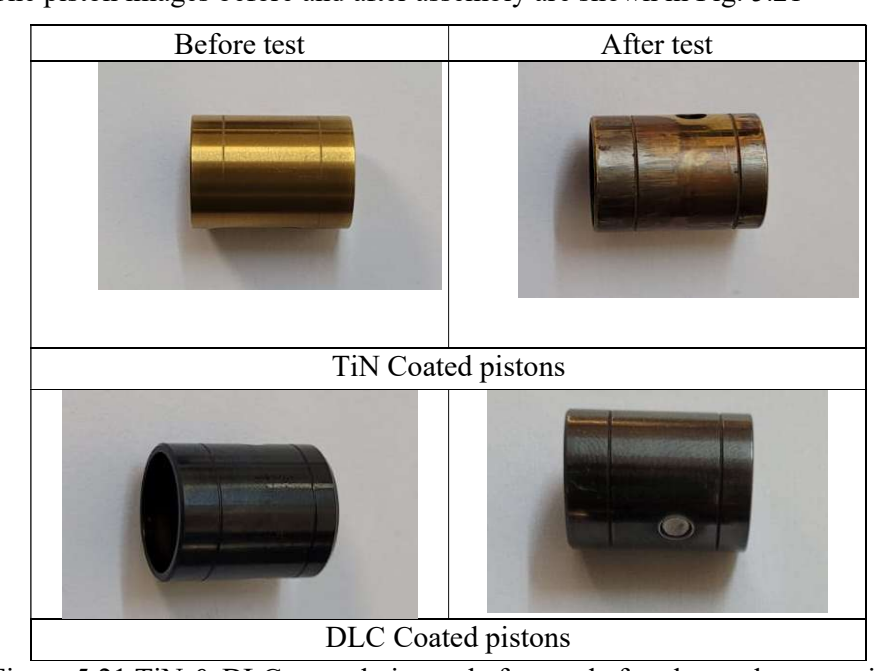


Figure 5.21 TiN & DLC coated pistons before and after the cooler operation

Both coolers were opened and reassembled with fresh DLC-coated pistons. Cooler-1 operated continuously for 83 hrs and cooler-2 operated for 101 hrs without any sign of a mechanical seizure, abnormal sound, vibration, or any surge in current/power during the testing. The cold tip temperatures versus time logged and the power versus time on the data acquisition system are shown in Figures 5.21 (a) & 5.21 (b) respectively for TiN-coated pistons. The cold tip temperature and power drawn measured during the experiment are shown in Figs. 5.22 (c) & 5.22 (d) for DLC-coated pistons.

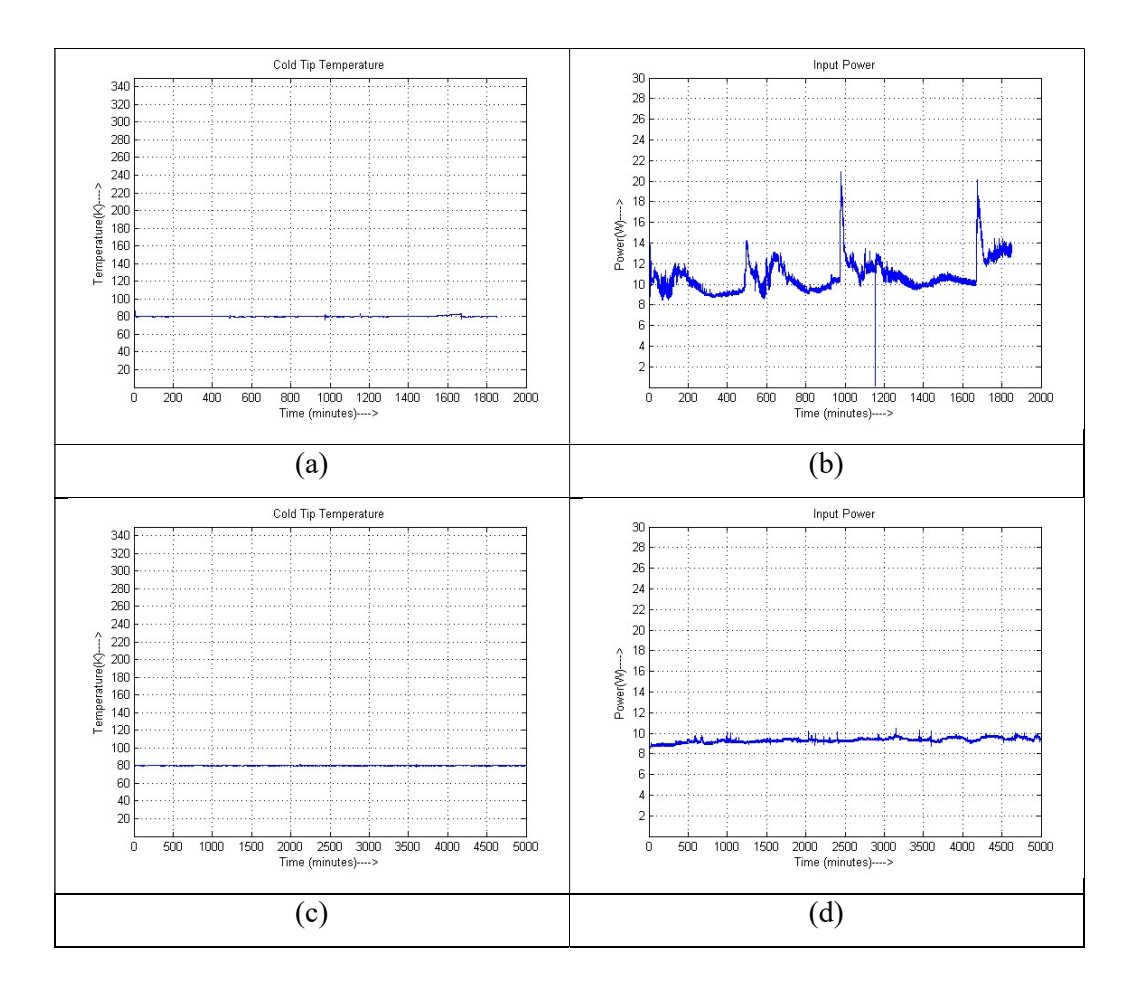


Figure 5.22 Time vs Cold tip temperature (left) and power characteristics (right) for TiN coated piston (a-b) &DLC coated piston (c-d)

5.8 Developed Stirling cooler prototype

	Specifications		
1.	Cooling Capacity	0.5 W @ 80K@ 23°C	
2.	Cold Finger Size (Dia.)	8mm max	
3.	Cool Down Time	< 6 minutes	
4.	Type of Drive	Crank Driven, DC Brushless Motor	
5.	Max. Input Power	< 20W	
6.	Steady State Input	< 7 W @ 220 mW @80K	
7.	Operating Temperature	-40 to 70°C	
8.	Weight	<0.5kg	



Figure 5.23 Specification of Stirling cryocooler prototype developed

EXPERIMENTAL TESTING AND VALIDATION

The objective was to investigate the necessary thermal conditions for the best performance of IR detectors and transducers in tactical applications such as missile seekers or hand-held thermal imaging as in our case.

The comprehensive simulation studies presented in Chapter 3 for cryochamber layout with different materials offer a crucial understanding of the various factors that affect the thermal performance of the cryochamber. To confirm the efficacy of the developed thermal model and analyse its capability in predicting the thermal performance of developed IR cryochambers, adequate experimentation needs to be carried out involving the measurement of cool-down temperature. With limited available literature on thermal modelling and the performance of such cryochambers, experimentation validation becomes even more important.

The following sections of the chapter detail the experimental validation studies conducted on the prototypes of infrared cryochamber integrated with the Joule Thomson cryocooler and Stirling cryocooler prototype developed. An overview of the experimental setup utilized and its critical subcomponents is also presented.

The validation has specifically been carried out for hollow glass configuration with properties corresponding to Case-I and Case-2 and for Inconel cryochamber corresponding to Case 3 as detailed in Chapter 3. These glass and Inconel configurations were integrated with the developed JT cryocooler. A prototype of the Stirling cryocooler developed after extensive thermal analysis was also experimentally tested for validation.

6.1 Experimental test setup for cryochamber testing with JT cooler

A test setup was developed for experiments on developed prototypes to validate the numerical simulation. The schematic in Figure 6.1, shows the arrangement of the Joule-Thomson cooler and Infrared cryogenic chamber assembly connected to a high-pressure bottle within a system including solenoid valves and regulation valves. Filters (molecular sieve and particulate) in the system ensure the purity of working fluid to

prevent choking and clogging of the cryocooler.

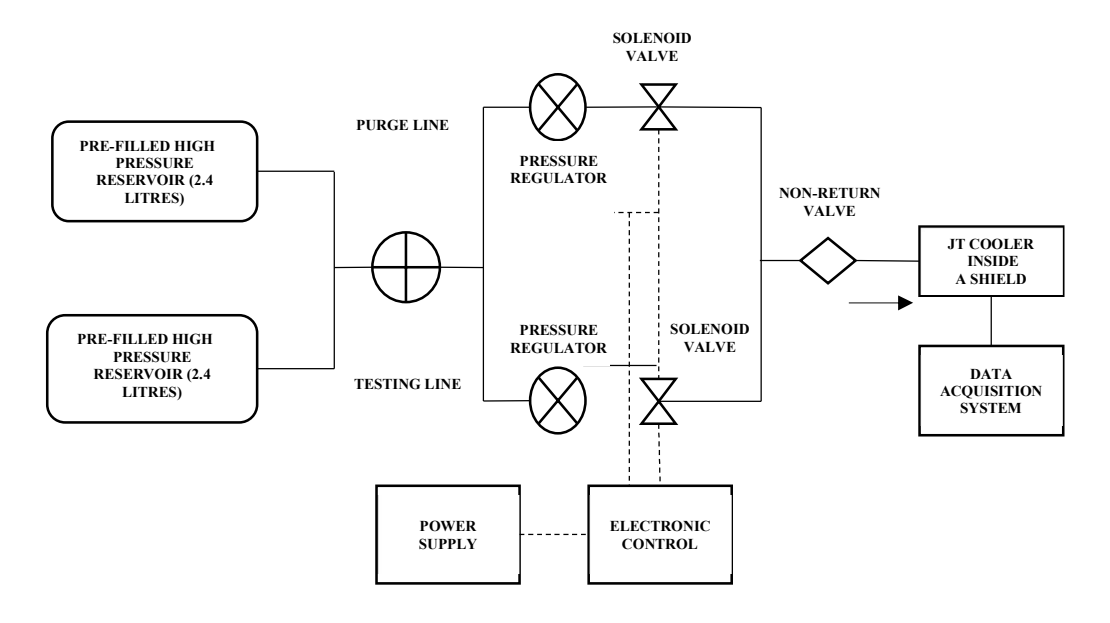


Figure 6.1 Test setup for integrated cryochamber and JT cryocooler assembly

6.1.1 Actual Experimentation

After completing the requisite pre-experimental procedures including recharging a high-pressure gas bottle and a thorough purging process to eliminate any residual contaminants, the high-pressure reservoir is set to the specific pressure necessary for experimentation. During the experiment, it is anticipated that the pressure within the reservoir may exhibit fluctuations; however, it is to be noted that the inlet pressure of the system is maintained at a constant level through the gas pressure regulation techniques and equipment. The operation of the gas flow is adeptly controlled by a solenoid valve, which functions by switching the flow on and off ensuring optimal conditions for the experiment. Before the gas enters the cryocooler, it is passed through a specialized filter assembly, for removing any particulate matter and impurities. Furthermore, the entire experimental setup is designed for remote operation, utilizing custom-designed Data Acquisition System (DAS) that facilitates real-time monitoring and data collection throughout the experimental process. In terms of temperature measurement, the system employs a highly accurate Resistance Temperature Device, either the Pt-100 or Pt-1000 models, specifically the PR-17 Model manufactured by Omega, for better precision and reliability. It is during this phase of the experiment that the observed temperature variations are closely monitored, and on stabilisation within the defined range, it is assumed that the system has successfully reached a steady-state condition. At this juncture, it is crucial to emphasize that data is systematically collected while the experiment is operating in this assumed steady-state, ensuring that the findings are both valid and reproducible for further analysis.

6.1.2 Testing with Glass Cryochamber

A glass cryochamber integrated with a developed JT cooler prototype and assembly was initially tested without simulating any device heat load. The time taken by the integrated assembly from an ambient temperature of 300K to reach 88K in 'device OFF' mode, is approximately 98 seconds to the predicted simulation value of 94 seconds. The experimental results for cooldown duration for the same glass cryochamber in the 'device OFF' mode at 328 K is approximately 116 seconds against the predicted simulation value of 114 seconds. Experimental findings are illustrated in Fig. 6.2.

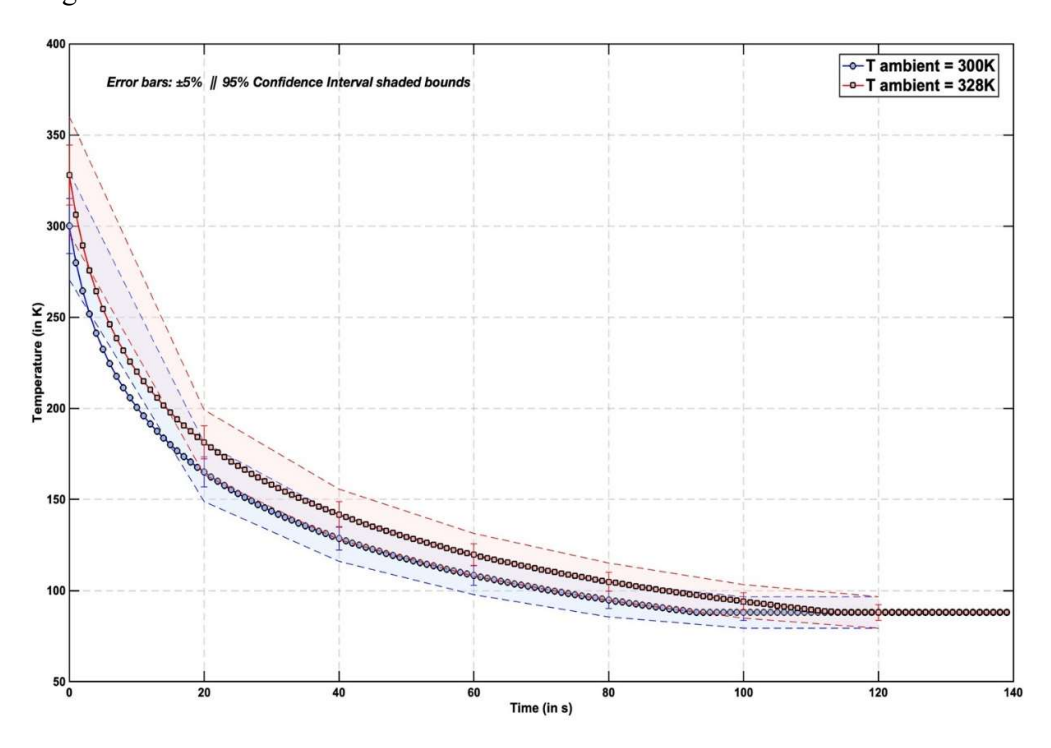


Figure 6.2 Experimental detector cool down time (CDT) for glass cryochamber at an ambient temperature of 300K & 328 K under "device OFF" condition

The cryochamber when functioning in 'device ON' mode, the experimental values of cooldown for the same glass cryochamber and JT cooler assembly increase to 100 seconds in comparison to the predicted simulation value of 98 seconds when the ambient temperature is 300 K while the cooldown duration is 118 seconds against the predicted simulation value of 116 seconds at an ambient temperature of 328 K. Experimental findings in 'device ON' condition for both 300K and 328K are illustrated in Fig. 6.3.

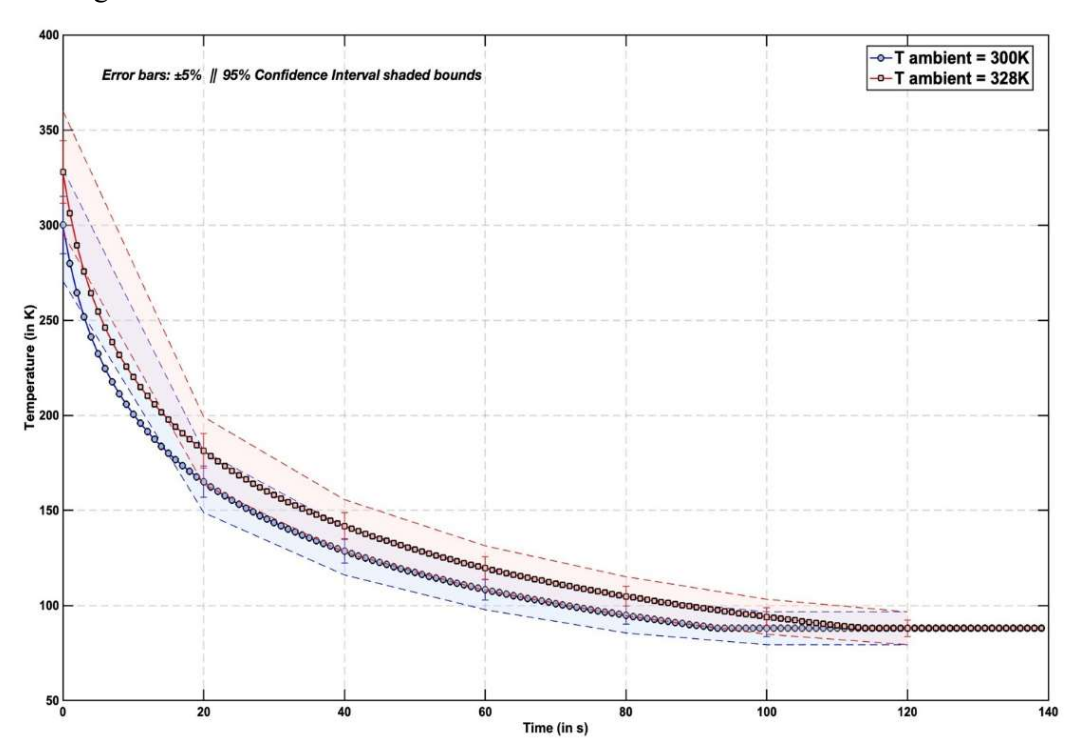


Figure 6.3 Experimental detector cool down time (CDT) for glass cryochamber at an ambient temperature of 300K & 328 K under "device ON" condition

6.1.3 Testing with Rapid Cooldown Inconel Cryochamber

For the rapid cooldown requirement of the applications, a metal cryochamber with an inner cryochamber of Inconel was designed and fabricated. The metal cryochamber was integrated with a developed JT cooler prototype, and the assembly was initially tested without simulating any device heat load. It is apparent from Fig. 6.4 that the experimental results for cooldown duration in 'device OFF' mode, specifically the time required to attain the target temperature of 88 K, is approximately 10 seconds

against the predicted simulation value of 9 seconds at an ambient temperature is 300 K. The results for cooldown duration for the same Inconel cryochamber assembly in the 'device OFF' mode at 328 K is approximately 11 seconds and matches with the predicted simulation value of 11 seconds.

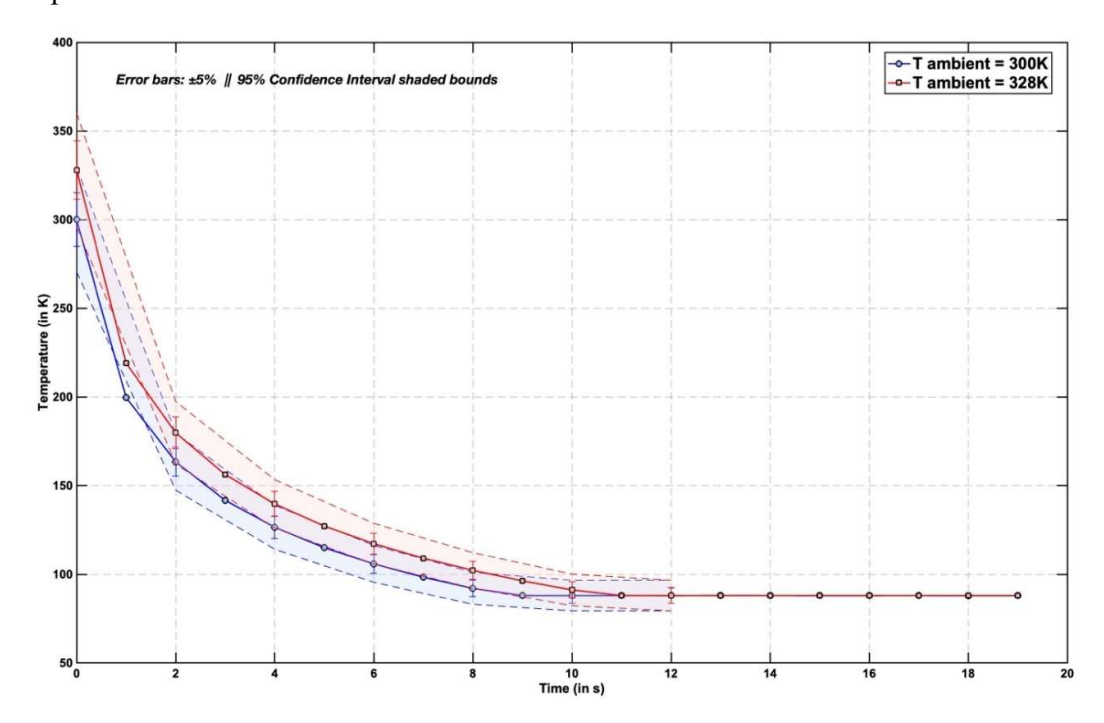


Figure 6.4 Experimental detector cool down time (CDT) for Inconel cryochamber at an ambient temperature of 300K & 328 K under "device OFF" condition

In a condition where the cryochamber is functioning in 'device ON' mode, the experimental values of cooldown duration for the Inconel cryochamber and JT cooler assembly is 12 seconds and matches with the predicted simulation value of 12 seconds for an ambient temperature of 300 K. The cooldown duration is 14 seconds against predicted simulation value of 13 seconds at 328 K. Experimental findings in 'device ON' condition for both 300K and 328K is illustrated in Fig. 6.5

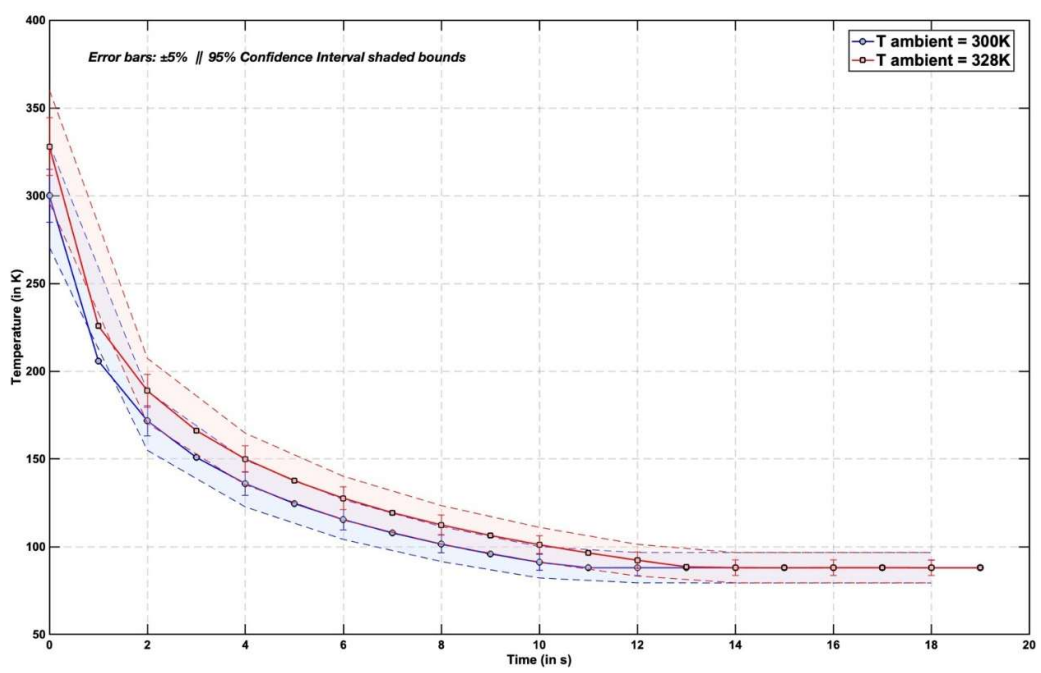


Figure 6.5 Experimental detector cool down time (CDT) for Inconel cryochamber at an ambient temperature of 300K & 328 K under "device ON" condition

6.2 Experimental test setup for cryochamber testing with Stirling cooler

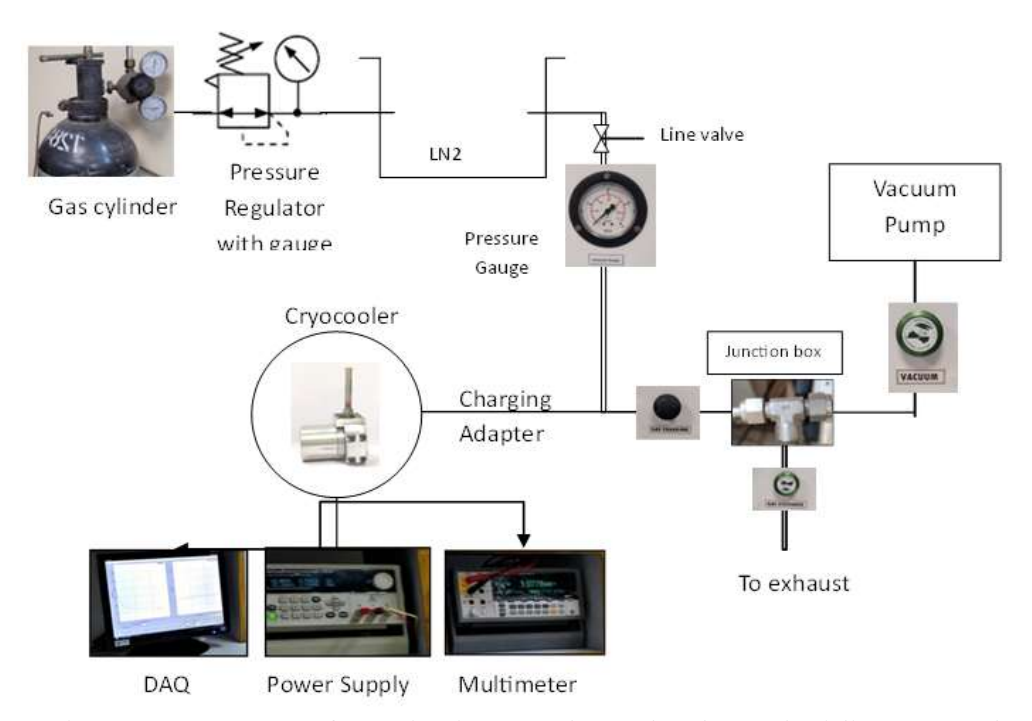


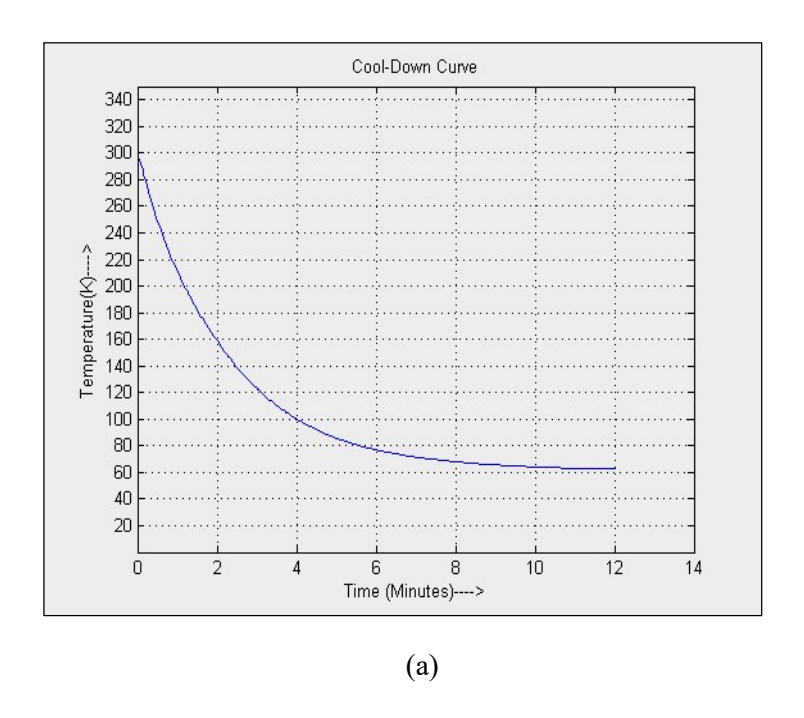
Figure 6.6 Test setup for testing integrated cryochamber and Stirling cryocooler

The cryocooler is tested on a dedicated experimental rig where the output parameters are continuously monitored through a dedicated data acquisition system shown in Fig. 6.6 The cryocooler is subjected to multiple cycles of charging and purging at ambient room temperature utilizing a rotary pump, to eliminate various contaminants in the form of dirt, water vapour, grease, and other particulates that may indirectly affect cooler operation. The helium gas charging line is equipped with a cryogenic trap, wherein a coil is immersed in liquid nitrogen, serving as a means of filtration to effectively capture and expel any moisture or contaminants present within the gas before its introduction into the system. Following the exhaustive purging to ensure maximum cleanliness, the cryocooler is replenished with 99.99% high-purity helium gas introduced into the system at a charge pressure ranging from 26 to 28 bar, ensuring optimal operational conditions. Upon the completion of the final assembly phase, the prototype cryocooler is subjected to a series of tests intended to evaluate its mechanical and thermal performance metrics, which are then compared against targeted specifications, shown in Table 6.1.

Table 6.1 Comparison of Targeted specifications and the achieved specifications for the Stirling cooler

Specifications	Target	Achieved
Cold Tip Temperature	80 K	< 80 K (~65K)
Cool down Time	8 minutes	6-7 minutes
Maximum Power	15 W	10 W
Steady State Power	10 W	8 W (Approx)

Furthermore, the performance data captured during these evaluations is recorded, and representative screenshots obtained from the data acquisition system are presented for analysis in Fig. 6.7.



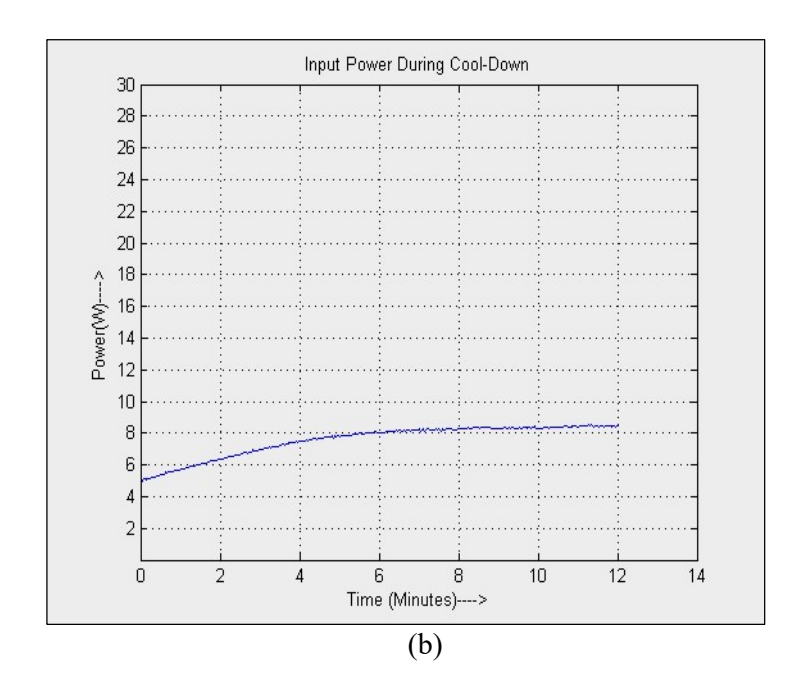


Figure 6.7 Screenshot of (a) Cooldown & (b) Power consumption of Stirling cryocooler

The current work is an exhaustive examination of the various thermal conditions and phenomena critically important for ensuring the optimal functionality and efficiency of infrared (IR) detectors, which play a pivotal role in applications across different scientific and technological domains. A comprehensive qualitative assessment of the design considerations associated with a cryochamber, also known as a Dewar, that houses these sophisticated IR devices has been meticulously conducted; this analysis encompasses a range of factors, including mechanical design considerations that ensure structural integrity, the imperative requirement for maintaining vacuum integrity to minimize thermal conduction, and the exploration of applicable refrigeration systems that are necessary for achieving the desired operational cryogenic temperatures. Additionally, a detailed finite volume analysis has been performed to facilitate a deeper understanding of the thermal phenomena within the cryochamber, thereby contributing to the overall body of knowledge regarding thermal management in such systems. Because traditional analytical methods necessitate the employment of an error function, which is recognized for being computationally demanding and resource-intensive, a more generalized numerical approach has been judiciously adopted to conduct both steady and transient thermal analyses, thereby enabling a more efficient exploration of the thermal dynamics involved.

The thermal modelling of the cryochamber has been systematically executed for both steady-state and transient conditions, and to ensure that the numerical model developed is sufficiently robust and reliable, an assessment was conducted to evaluate grid convergence and the independence of time steps, thereby confirming the accuracy and validity of the simulation results.

A comprehensive theoretical and thermophysical investigation of miniature Joule-Thomson (JT) and Stirling cryocoolers has also been conducted to elucidate design considerations and evaluate the influence of specified parameters on the operational efficacy and performance of both coolers.

Separate experimental setups were developed for testing cryochambers with JT cooler

and Stirling cryocoolers. Results obtained from theoretical analysis and modeling exercise have undergone a rigorous validation process through experimental investigations conducted on developed test setups, to establish the efficacy and reliability of the proposed thermal models.

The experimental results for cooldown duration for the glass cryochamber and JT cooler assembly in the *device OFF*' mode, specifically the time required to attain the target temperature of 88 K, is approximately 98 seconds in comparison to the predicted simulation value of 94 seconds when the ambient temperature is 300 K. The experimental results for cooldown duration for the same glass cryochamber assembly in the 'device OFF' mode at 328 K is approximately 116 seconds against the predicted simulation value of 114 seconds.

In instances where the cryochamber is functioning in 'device ON' mode, the experimental values of cooldown duration for the same glass cryochamber and JT cooler assembly increase to 109 seconds in comparison to the predicted simulation value of 105 seconds when the ambient temperature is 300 K while the cooldown duration is 118 seconds against the predicted simulation value of 116 seconds at an ambient temperature of 328 K

In the case of rapid cooldown metallic (Inconel) cryochamber, the experimental results for cooldown duration in 'device OFF' mode, is approximately 10 seconds against the predicted simulation value of 9 seconds when the temperature is 300 K and the value in 'device OFF' mode at 328 K is approximately 11 seconds matching with the predicted simulation value of 11 seconds.

In 'device ON' mode, the experimental values of cooldown duration for the Inconel cryochamber and JT cooler assembly is 12 seconds and matches with the predicted simulation value of 12 seconds when the ambient temperature is 300 K while the cooldown duration is 14 seconds against the predicted simulation value of 13 seconds at 328 K

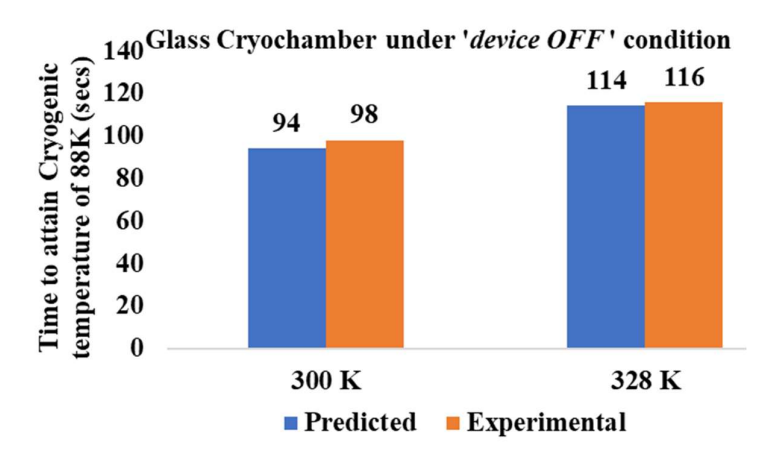


Figure 7.1 Comparison chart for predicted and experimental values of the cool-down duration for glass cryochamber under 'device OFF' condition

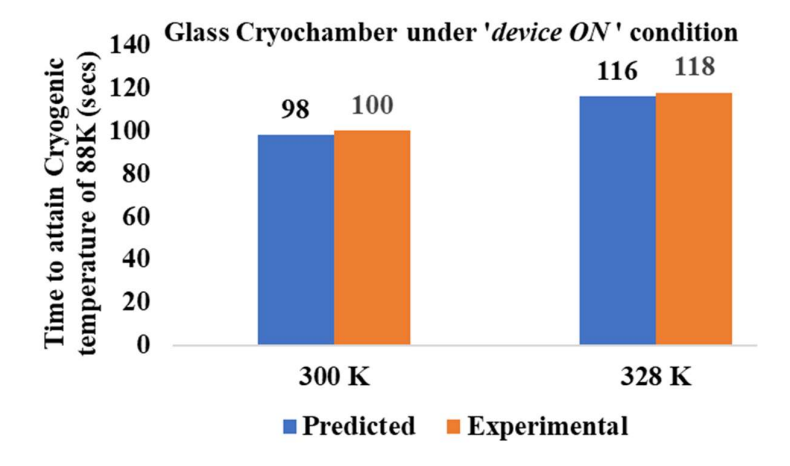


Figure 7.2 Comparison chart for predicted and experimental values of the cool-down duration for glass cryochamber under 'device ON' condition

Consequently, the numerical analysis accurately predicts the duration required for the cooldown process, as evidenced by an empirically observed maximum deviation of approximately 4.2% when applied to the glass cryochamber scenario, while exhibiting a significantly lower error of 1% in the context of the rapid cooldown metallic cryochamber. The comparison charts for the predicted and experimental values for the cool-down duration for glass cryochambers are shown in Fig. 7.1 and 7.2 under 'device OFF' and 'device ON' conditions respectively.

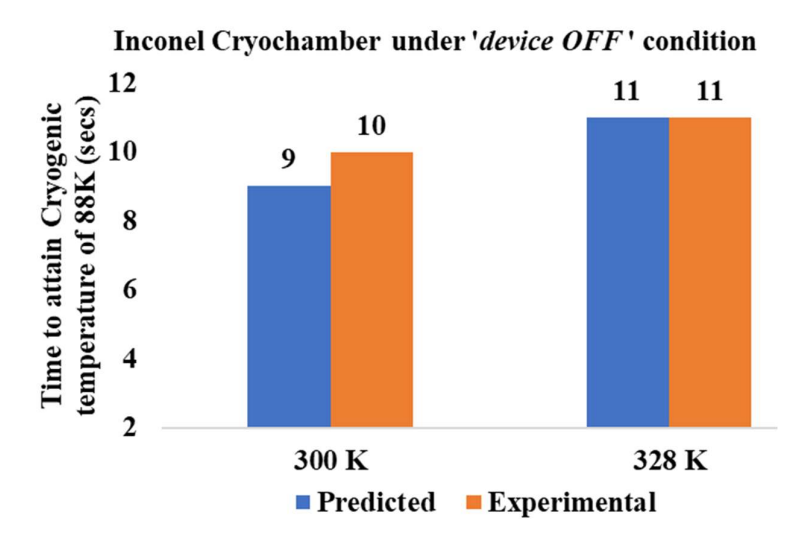


Figure 7.3 Comparison chart for predicted and experimental values of the cool-down duration for Inconel cryochamber under 'device OFF' condition

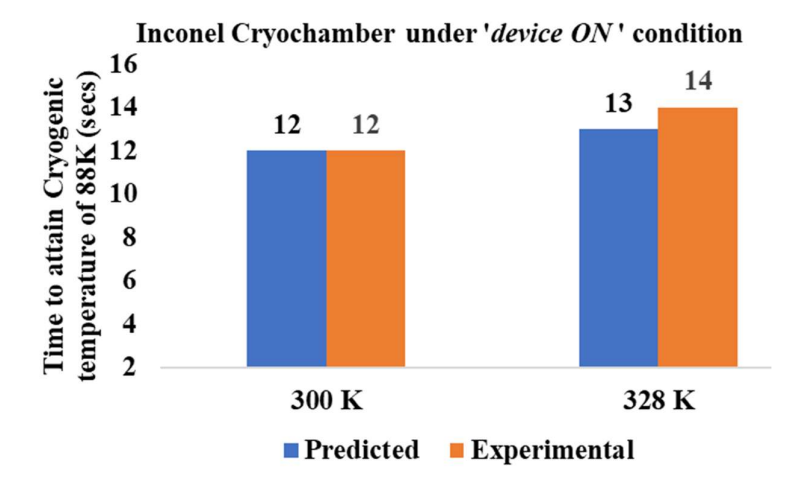


Figure 7.4 Comparison chart for predicted and experimental values of the cool-down duration for Inconel cryochamber under 'device ON' condition

The comparison charts for the predicted and experimental values for the cool-down duration for Inconel cryochambers are shown in Fig. 7.3 and 7.4 under 'device OFF' and 'device ON' conditions respectively.

The integrated Stirling cryocooler and cryochamber assembly was also tested on the developed experimental setup and could meet the desired specifications proving the design of the cooler and the specific cryochamber.

The inferences that can be derived from the extensive numerical simulations that were conducted utilizing the developed model in conjunction with theoretical analysis for both the Joule-Thomson (JT) cooler and the Stirling cooler systems are as follows:

7.1 IR Cryochamber

- The gas conduction coefficient can be characterized as fundamentally dependent on the pressure within the confines of the cryochamber and demonstrates an increasing trend corresponding to an increase in the pressure levels.
- The gas conduction coefficient is crucial in influencing the existing temperature length profile, particularly when the system has reached a steady state, thereby highlighting its significant impact on the thermal distribution within the system.
- The temperature length profile exhibits a markedly steeper gradient when the cold well is constructed from metal Inconel in this case, as opposed to when it is fabricated from glass, indicating a marked difference in thermal behaviour based on the material composition of the cold well.
- In 'device OFF' conditions, the estimated time required for cool-down is significantly shorter than when the cryochamber is functioning under a 'device ON' condition, despite both cases being maintained at the same temperature level.
- When comparing the estimated cool-down time under 'device ON' conditions, it is observed that this duration is considerably longer when the initial ambient temperature is set at 328 K, in contrast to the situation where the cryochamber operates from a standard ambient temperature of 300 K.
- It has been noted that variations in thermal conductivity affect the duration of the cool-down time experienced by the detector, which suggests a vital correlation between these two parameters.

7.2 Joule Thomson (JT) Cryocooler

(a) Thermo-physical properties vary significantly at low temperatures. The effect of property variation on the heat exchanger performance is studied.

(b)Parametric study on the J-T cryocooler

- The investigation into the influence exerted by various parameters—including supply pressure, fin height, fin density, and mass flow rate—on the overall performance metrics of the cooler has been carried out. It has been observed that as the mass flow rate experiences an increase, the pressure drop experiences an increase within the hot fluid leading to a decrease in the overall effectiveness of the heat exchanger.
- An increase in the fin density improves the operational effectiveness of the HX. However, pressure drop on the cold side increases since dense fins offer greater resistance to gas flow on the cooler side.
- Hot and cold fluids experience a decrease in pressure drop with the increase in fin length. However, the pressure drop decrease in cold fluid is greater than in hot fluid.

(c) Performance analysis for the developed J-T cooler

- An investigation is conducted to understand the impact of mass flow rate on overall system performance. With an increase in mass flowrate, cooling capacity increases up to 0.2 g/s and then decreases.
- The increase in pressure drop of the hot fluid experiences an increase when the mass flow rate is increased.
- A mass flow rate of 0.2 g/s gives optimum performance 2.9 W at 80 K coolingcapacity while the pressure drop corresponding to it in a hot fluid is 37 bar.
- Effect of gas supply pressure is studied With an increase in supply pressure, cooling capacity increases.
- The required mass flow rate to produce maximum cooling power increases with pressure.
- With supply pressure increase, the maximum flow rate for operating the

cryocooler increases.

• On increasing the supply pressure, there is a decrease in pressure drop in hot fluid

7.3 Stirling Cryocooler

- For the regenerator design, it is concluded that the mesh size 500 has better efficacy than 400 & 300 number mesh sizes. The regenerator performance has also been enhanced resulting in lesser cool-down time and lower cold-tip temperature.
- The introduction of DLC Coating on the compressor piston reduced the power consumption and increased the number of operational hours.
- To minimize the overall conductive type of thermal load on the cryochamber, the thickness of the cold tube is reduced to $100\mu m$.
- Inconel is used for cold tube fabrication due to lower thermal conductivity (reduces axial conduction) and better machinability.

7.4 Industrial relevance or technology readiness level (TRL)

As discussed, the technology of the Infrared detector is extremely critical for the indigenous development of thermal imaging systems for defence applications. The research work carried out has resulted in the optimization and development of sub-technologies of ultra-high vacuum packaging and cryocoolers required for maintaining the Infrared device at cryogenic temperature. The effort has propelled the technology to overall TRL levels of 6 and it is planned to initiate integration with the main systems.

RECOMMENDATIONS FOR FUTURE WORK

The performance and operation of infrared detectors (IR) are affected primarily by two main components,

- a. Vacuum-sealed cryochamber housing the IR detector
- b. Cooling technology for attaining the cryo temperature necessary for optimal performance of the housed detector

The present study focuses on theoretical and experimental analysis of IR cryochamber, Joule Thomson Cryocooler, and Stirling Cryocooler in sufficient detail. A few areas for future studies are listed below:

- a) Systematically identify and analyze the Infrared detector cryochamber failure modes such as failure of electrical bonds, degradation of diodes, loss of vacuum, leak of the working medium, wear, and chamber contamination due to outgassing. This identification and analysis of the failure modes will help in improving the overall reliability of the advanced infrared systems.
- b) Stirling cryocoolers due to variable cooling capacity, reliability, and ability to operate over a wide range of temperatures and non-sensitivity for the satellite attitude have significant potential in space applications for cooling infrared sensors, scientific instruments, and other payloads on satellites and space probes. Study on design aspects of suitable Stirling cryocoolers with relatively compact size and lightweight construction along with their thermophysical analysis is another area with future scope.
- c) As infrared detector cooling technologies, Stirling coolers and Joule-Thomson (JT) coolers are the main solutions. Stirling coolers have mechanical reciprocating motions leading to noise and a limiting lifespan whereas Joule-Thomson coolers use high-pressure gas cylinders; which require frequent replacement due to their limited volume capacity. Multistage thermoelectric coolers emerge as a good alternative, offering numerous advantages, including the absence of moving parts, independence from refrigerants, exceptional

reliability, and a remarkable maintenance-free operational capability. The use of genetic algorithms in the comprehensive design framework of thermoelectric coolers with the deployment of optimization algorithms aimed at fine-tuning the current in each stage to enhance the overall performance and efficiency can be a prominent area for future investigation and research for Infrared detector cooling using thermoelectric cooler.

References

- [1] Vincent, J. D. (1990). Fundamentals of infrared detector operation and testing (p. 504).
- [2] D. L. Shumaker, J. T. Wood, C. R. Thacker. Infrared Imaging Systems Analysis. ERIM Series in Infrared & Electro-Optics, Environmental Research Institute of Michigan (1993)
- [3] Matthews, S. J. (2004). Thermal imaging on the rise. *Laser focus world*, 40(3), 105-109.
- [4] Kastberger, G., & Stachl, R. (2003). Infrared imaging technology and biological applications. *Behavior Research Methods, Instruments, & Computers*, *35*, 429-439.
- [5] E.A. Sergeant, "Cryogenics in industry, research and medicine", Modern Refrigeration Air control, Oct 1996
- [6] Walker, G., & Bingham, E. R. (1994). Low-capacity cryogenic refrigeration (No. 9). Oxford University Press.
- [7] Radebaugh, R. (2009). Cryocoolers: the state of the art and recent developments. *Journal of Physics: Condensed Matter*, 21(16), 164219.
- [8] Rogalski, A. (2002). Infrared detectors: an overview. *Infrared physics & technology*, 43(3-5), 187-210.
- [9] Rogalski, A. (2011). Recent progress in infrared detector technologies. *Infrared Physics & Technology*, 54(3), 136-154.
- [10] Veprik, A., Riabzev, S., Avishay, N., Oster, D., & Tuitto, A. (2012, May). Linear cryogenic coolers for HOT infrared detectors. In *Infrared Technology and Applications XXXVIII* (Vol. 8353, pp. 657-667). SPIE.
- [11] Fraenkel, R., Haski, J., Mizrahi, U., Shkedy, L., Shtrichman, I., & Pinsky, E. (2014, June). Cooled and uncooled infrared detectors for missile seekers. In *Infrared Technology and Applications XL* (Vol. 9070, pp. 211-220). SPIE.
- [12] Bhan, R. K., & Dhar, V. (2019). Recent infrared detector technologies, applications, trends and development of HgCdTe based cooled infrared focal plane arrays and their characterization. *Opto-Electronics Review*, 27(2), 174-193.
- [13] Rogalski, A. (2012). Progress in focal plane array technologies. *Progress in Quantum Electronics*, 36(2-3), 342-473.

- [14] Incropera, F. P., DeWitt, D. P., Bergman, T. L., & Lavine, A. S. (1996). Fundamentals of heat and mass transfer (Vol. 6, p. 116). New York: Wiley.
- [15] Pal, R. (2017). Infrared technologies for defence systems. *Def Sci J*, 67(2), 133-134.
- [16] Tidrow, M. Z., & Dyer, W. R. (2001). Infrared sensors for ballistic missile defense. *Infrared Physics & Technology*, 42(3-5), 333-336.
- [17] Karim, A., & Andersson, J. Y. (2013, December). Infrared detectors: Advances, challenges and new technologies. In *IOP Conference Series: Materials Science and Engineering* (Vol. 51, No. 1, p. 012001). IOP Publishing.
- [18] Webb, D. B. (1982). Thermal imaging via cooled detectors. *Radio and Electronic Engineer*, 52(1), 17-30.
- [19] Veprik, A., Ashush, N., Shlomovich, B., Oppenhaim, Y., Gridish, Y., Kahanov, E., ... & Tuito, A. (2014, June). Ruggedizing infrared integrated Dewardetector assemblies for harsh environmental conditions. In *Infrared Technology and Applications XL* (Vol. 9070, pp. 757-766). SPIE.
- [20] Lai, C., Yang, S., & Lu, G. (2013, July). Failure analysis of integrated detector Dewar cryocooler assembly. In 2013 International Conference on Quality, Reliability, Risk, Maintenance, and Safety Engineering (QR2MSE) (pp. 935-938). IEEE.
- [21] Yang, S., & Lai, C. (2014, August). Accelerated test and life prediction of integrated Dewar for infrared detector. In 2014 10th International Conference on Reliability, Maintainability and Safety (ICRMS) (pp. 230-232). IEEE.
- [22] Jain, A., & Biswas, A. (2017). Parasitic Flux analysis of cooled Infrared Detectors for Space applications. *Defence Science Journal*, 67(2), 193.
- [23] Byung-Ha, K. (2006). Thermal analysis of a cryochamber for an infrared detector considering a Radiation shield. *Korean Journal of Air-Conditioning and Refrigeration Engineering*, 18(8), 672-677.
- [24] Zhang, X., Bai, J., & Yin, S. (2016, January). The optical design of highly efficient cold shield in IR detector based on ASAP. In *Journal of Physics: Conference Series* (Vol. 680, No. 1, p. 012015). IOP Publishing.
- [25] Hoon, L. J. (2004). An experimental study on the cooling characteristics of an infrared detector cryochamber. *Korean Journal of Air-Conditioning and Refrigeration Engineering*, 16(10), 889-894.

- [26] Kim, Y. M., Kang, B. H., & Park, S. J. (2008). An experimental study on the thermal load of a cryochamber with Radiation shields. *Korean Journal Of Air-Conditioning and Refrigeration Engineering*, 20(1), 11-16.
- [27] Singhal, M., Singhal, G., Verma, A. C., Kumar, S., & Singh, M. (2017). Numerical investigation of steady-state thermal behavior of an infrared detector cryo chamber. *Thermal Science*, *21*(3), 1203-1212.
- [28] Kim, H. Y., Kang, B. H., & Lee, D. Y. (2000). A parametric study on the cooling characteristics of an infrared detector cryochamber. *Cryogenics*, 40(12), 779-788.
- [29] Singhal, M., Singhal, G., Verma, A. C., Kumar, S., & Singh, M. (2016). Thermophysics modeling of an infrared detector cryochamber for transient operational scenario. *Infrared Physics & Technology*, 76, 103-110.
- [30] Kushare, M., Jhaveri, A., & Bhargav, A. (2017, May). Radiation heat transfer analysis of spectrometer's Dewar Cooling Assembly. In 2017 16th IEEE Intersociety Conference on Thermal and Thermomechanical Phenomena in Electronic Systems (ITherm) (pp. 793-799). IEEE.
- [31] Raab, J., Tward, E., Toma, G., & Nguyen, T. (2012). Integrated detector cooler assembly for space applications. *Cryocoolers*, *17*, 525-529.
- [32] Veprik, A., Shlomovich, B., & Tuito, A. (2015, November). Warm-up calorimetry of Dewar-Detector Assemblies. In *IOP Conference Series: Materials Science and Engineering* (Vol. 101, No. 1, p. 012114). IOP Publishing.
- [33] Boffito, C., Ferrario, B., Rosai, L., & Doni, F. (1987). Gettering in cryogenic applications. *Journal of Vacuum Science & Technology A: Vacuum, Surfaces, and Films*, 5(6), 3442-3445.
- [34] Glaister, D. S., Donabedian, M., Curran, D. G. T., & Davis, T. (1999, March). An assessment of the state of cryocooler technology for space applications. In *1999 IEEE Aerospace Conference. Proceedings (Cat. No. 99TH8403)* (Vol. 5, pp. 367-382). IEEE.
- [35] Wiecek, B. (2006, January). Cooling and shielding systems for infrared detectors-requirements and limits. In 2005 IEEE Engineering in Medicine and Biology 27th Annual Conference (pp. 619-622). IEEE.
- [36] Wiatr, W., Opalski, L., Piotrowski, J., & Krysicki, M. (2016, May). Modeling

- interconnects for thermoelectrically cooled infrared detectors. In 2016 21st International Conference on Microwave, Radar and Wireless Communications (MIKON) (pp. 1-4). IEEE.
- [37] Bhatia, R. S., Chase, S. T., Jones, W. C., Keating, B. G., Lange, A. E., Mason, P. V., ... & Sirbi, G. (2002). Closed cycle cooling of infrared detectors to 250 mK. *Cryogenics*, 42(2), 113-122.
- [38] Cao, H. S., Mudaliar, A. V., Derking, J. H., Lerou, P. P. P. M., Holland, H. J., Zalewski, D. R., ... & Ter Brake, H. J. M. (2012). Design and optimization of a two-stage 28 K Joule–Thomson microcooler. *Cryogenics*, *52*(1), 51-57.
- [39] Levenduski, R., & Scarlotti, R. (1996). Joule-Thomson cryocooler for space applications. *Cryogenics*, *36*(10), 859-866.
- [40] Ardhapurkar, P. M., Sridharan, A., & Atrey, M. D. (2014). Experimental investigation on temperature profile and pressure drop in two-phase heat exchanger for mixed refrigerant Joule–Thomson cryocooler. *Applied thermal engineering*, 66(1-2), 94-103.
- [41] Marquardt, E. D., Radebaugh, R., & Dobak, J. (1998). A cryogenic catheter for treating heart arrhythmia. In *Advances in Cryogenic Engineering* (pp. 903-910). Boston, MA: Springer US.
- [42] Jin, L., Lee, C., Baek, S., & Jeong, S. (2018). Design of high-efficiency Joule-Thomson cycles for high-temperature superconductor power cable cooling. *Cryogenics*, *93*, 17-25.
- [43] Atrey, M. D. (1998). Thermodynamic analysis of Collins helium liquefaction cycle. *Cryogenics*, *38*(12), 1199-1206.
- [44] Gupta, P. K., Kush, P. K., & Tiwari, A. (2007). Second law analysis of counter flow cryogenic heat exchangers in presence of ambient heat-in-leak and longitudinal conduction through wall. *International journal of heat and mass transfer*, 50(23-24), 4754-4766.
- [45] Barron, R. F., & Nellis, G. F. (2017). Cryogenic heat transfer. CRC press.
- [46] Flynn, T. M. "Cryogenic engineering", Marcel Dekker, 2nd rev. ed, New York, 2005.
- [47] Xue, H., Ng, K. C., & Wang, J. B. (2001). Performance evaluation of the recuperative heat exchanger in a miniature Joule–Thomson cooler. *Applied Thermal*

- Engineering, 21(18), 1829-1844.
- [48] Ng, K. C., Xue, H., & Wang, J. B. (2002). Experimental and numerical study on a miniature Joule–Thomson cooler for steady-state characteristics. *International journal of heat and mass transfer*, 45(3), 609-618.
- [49] Chua, H. T., Wang, X., & Teo, H. Y. (2006). A numerical study of the Hampson-type miniature Joule—Thomson cryocooler. *International Journal of Heat and Mass Transfer*, 49(3-4), 582-593.
- [50] Hong, Y. J., Park, S. J., & Choi, Y. D. (2009). A numerical study of the performance of a heat exchanger for a miniature Joule-Thomson refrigerator. *Cryocoolers*, 15, 379-386.
- [51] Ardhapurkar, P. M., & Atrey, M. D. (2014). Performance optimization of a miniature Joule–Thomson cryocooler using numerical model. *Cryogenics*, 63, 94-101.
- [52] Chou, F. C., Pai, C. F., Chien, S. B., & Chen, J. S. (1995). Preliminary experimental and numerical study of transient characteristics for a Joule-Thomson cryocooler. *Cryogenics*, 35(5), 311-316.
- [53] Chien, S. B., Chen, L. T., & Chou, F. C. (1996). A study on the transient characteristics of a self-regulating Joule-Thomson cryocooler. *Cryogenics*, 36(12), 979-984.
- [54] Hong, Y. J., Park, S. J., Kim, H. B., & Choi, Y. D. (2006). The cool-down characteristics of a miniature Joule–Thomson refrigerator. *Cryogenics*, 46(5), 391-395.
- [55] Hong, Y. J., Park, S. J., & Choi, Y. D. (2010). A numerical study on operating characteristics of a miniature Joule-Thomson refrigerator. *Progress in Superconductivity and Cryogenics*, 12(4), 41-45.
- [56] Yu, J., Tian, G., & Xu, Z. (2009). Exergy analysis of Joule–Thomson cryogenic refrigeration cycle with an ejector. *Energy*, *34*(11), 1864-1869.
- [57] Derking, J. H., Ter Brake, H. J. M., Sirbi, A., Linder, M., & Rogalla, H. (2009). Optimization of the working fluid in a Joule–Thomson cold stage. *Cryogenics*, 49(3-4), 151-157.
- [58] Damle, R. M., & Atrey, M. D. (2015). The cool-down behaviour of a miniature Joule–Thomson (J–T) cryocooler with distributed J–T effect and finite reservoir capacity. *Cryogenics*, 71, 47-54.

- [59] Cao, H. S., Vanapalli, S., Holland, H. J., Vermeer, C. H., & Ter Brake, H. J. M. (2017). Numerical analysis of clogging dynamics in micromachined Joule—Thomson coolers. *international journal of refrigeration*, 81, 60-68.
- [60] Cao, H. S., Vanapalli, S., Holland, H. J., Vermeer, C. H., & ter Brake, H. J. (2015). Sensitivity of micromachined Joule-Thomson cooler to clogging due to moisture. *Physics Procedia*, 67, 417-422.
- [61] Collaudin, B., & Rando, N. (2000). Cryogenics in space: a review of the missions and of the technologies. *Cryogenics*, 40(12), 797-819.
- [62] Ross, R. G. (2007). Aerospace coolers: a 50-year quest for long-life cryogenic cooling in space. In *Cryogenic Engineering* (pp. 225-284). New York, NY: Springer New York.
- [63] Wang, B., & Gan, Z. H. (2013). A critical review of liquid helium temperature high frequency pulse tube cryocoolers for space applications. *Progress in Aerospace Sciences*, *61*, 43-70.
- [64] Radebaugh, R. (2009). Cryocoolers: the state of the art and recent developments. *Journal of Physics: Condensed Matter*, 21(16), 164219.
- [65] Bhatia, R. S. (2002). Review of spacecraft cryogenic coolers. *Journal of spacecraft and rockets*, 39(3), 329-346.
- [66] Wang, G., Cai, J., Jing, W., Yang, L., & Liang, J. (2007). Development of a 0.5 W/40 K pulse tube cryocooler for an infrared detector. International Cryocooler Conference.
- [67] Radebaugh, R. (2000). Pulse tube cryocoolers for cooling infrared sensors. *Infrared Technology and Applications XXVI*, 4130, 363-379.
- [68] Squires, M. (2014). Cobham microcooler for high temperature applications. *Power (W)*, 18(20), 25.
- [69] Willems, D., Mullié, J., Wordragen, F. V., de Jonge, G., & BV, T. C. (2018). A linear Stirling cooler for extreme ambient temperatures. In *International Cryocooler Conference*.
- [70] Olson, J. R., Champagne, P., Roth, E. W., Kaldas, G. B., Nast, T., Saito, E., ... & Dobbins, C. L. (2014). Coaxial pulse tube microcryocooler. *Cryocoolers*, 18, 51-57.
- [71] Walker, G., Fauvel, R., & Reader, G. (1989). Miniature refrigerators for

- cryogenic sensors and cold electronics. Cryogenics, 29(8), 841-845...
- [72] Higa, W. H. (1965). A practical Philips cycle for low-temperature refrigeration.
- [73] Davey, G., & Orlowska, A. H. (1987). Miniature Stirling cycle cooler. *Cryogenics*, 27(3), 148-151.
- [74] Penswick, B., & Urieli, I. (1984, August). Duplex stirling machines. In *Proc., Intersoc. Energy Convers. Eng. Conf.; (United States)* (Vol. 3, No. CONF-840804-). Sunpower, Inc., Athens, Ohio.
- [75] Doğan, B., Ozturk, M. M., & Erbay, L. B. (2018). Effect of working fluid on the performance of the duplex Stirling refrigerator. *Journal of Cleaner Production*, 189, 98-107.
- [76] Langdon-Arms, S., Gschwendtner, M., & Neumaier, M. (2018). A novel solar-powered liquid piston Stirling refrigerator. *Applied energy*, 229, 603-613.
- [77] Caughley, A., Sellier, M., Gschwendtner, M., & Tucker, A. (2016). A free-piston Stirling cryocooler using metal diaphragms. *Cryogenics*, 80, 8-16.
- [78] Getie, M. Z., Lanzetta, F., Bégot, S., Admassu, B. T., & Hassen, A. A. (2020). Reversed regenerative Stirling cycle machine for refrigeration application: A review. *International Journal of Refrigeration*, 118, 173-187.
- [79] Toghyani, S., Kasaeian, A., Hashemabadi, S. H., & Salimi, M. (2014). Multi-objective optimization of GPU3 Stirling engine using third order analysis. *Energy Conversion and Management*, 87, 521-529.
- [80] Xu, Y., Sun, D., Qiao, X., Yan, S. W., Zhang, N., Zhang, J., & Cai, Y. (2017). Operating characteristics of a single-stage Stirling cryocooler capable of providing 700 W cooling power at 77 K. *Cryogenics*, 83, 78-84.
- [81] Bhojwani, V., Inamdar, A., Lele, M., Tendolkar, M., Atrey, M., Bapat, S., & Narayankhedkar, K. (2017). Opposed piston linear compressor driven two-stage Stirling Cryocooler for cooling of IR sensors in space application. *Cryogenics*, 83, 71-77.
- [82] Singh, M., Sadana, M., Sachdev, S., & Pratap, G. (2013). Development of miniature Stirling cryocooler technology for infrared focal plane array. *Defence Science Journal*, 63(6), 571.
- [83] Zhao, X., & Zhang, J. (2014). Numerical simulation of a high power Stirling cryocooler.

- [84] Curzon, F. L., & Ahlborn, B. (1975). Efficiency of a Carnot engine at maximum power output. *American Journal of Physics*, 43(1), 22-24.
- [85] Petrescu, S., Costea, M., Harman, C., & Florea, T. (2002). Application of the direct method to irreversible Stirling cycles with finite speed. *International Journal of Energy Research*, 26(7), 589-609.
- [86] Chen, L., Wu, C., & Sun, F. (1998). Cooling load versus COP characteristics for an irreversible air refrigeration cycle. *Energy Conversion and Management*, 39(1-2), 117-125.
- [87] Martaj, N., Grosu, L., & Rochelle, P. (2006). Exergetical analysis and design optimisation of the Stirling engine. *International Journal of Exergy*, *3*(1), 45-67.
- [88] Feidt, M. L. (2008). Optimal use of energy systems and processes. *International Journal of Exergy*, 5(5-6), 500-531.
- [89] Cha, J. S., Ghiaasiaan, S. M., & Kirkconnell, C. S. (2008). Oscillatory flow in microporous media applied in pulse–tube and Stirling–cycle cryocooler regenerators. *Experimental thermal and fluid science*, *32*(6), 1264-1278.
- [90] Costa, S. C., Barreno, I., Tutar, M., Esnaola, J. A., & Barrutia, H. (2015). The thermal non-equilibrium porous media modelling for CFD study of woven wire matrix of a Stirling regenerator. *Energy conversion and management*, 89, 473-483.
- [91] Srinivasan, K. V., Manimaran, A., Pokale, R. D., & Arulprakasajothi, M. (2017). Theoretical analysis and optimization of regenerator of Stirling cryocooler. *American Journal of Science and Technology*, 4(4), 67-73.
- [92] De Boer, P. C. T. (2011). Optimal performance of regenerative cryocoolers. *Cryogenics*, 51(2), 105-113.
- [93] Tao, Y. B., Liu, Y. W., Gao, F., Chen, X. Y., & He, Y. L. (2009). Numerical analysis on pressure drop and heat transfer performance of mesh regenerators used in cryocoolers. *Cryogenics*, 49(9), 497-503.
- [94] Zhao, Y., & Dang, H. (2016). CFD simulation of a miniature coaxial Stirling-type pulse tube cryocooler operating at 128 Hz. *Cryogenics*, 73, 53-59.
- [95] Li, R., & Grosu, L. (2017). Parameter effect analysis for a Stirling cryocooler. *International Journal of Refrigeration*, 80, 92-105.
- [96] Devienne, F.M., Low Density Heat Transfer, *Adv Heat Transfer* 1965, 2: 271-356

- [97] Springer G. S., Heat Transfer in Rarefied gases, *Adv Heat Transfer* 1970; 7: 163-218
- [98] Schaber, K. (1998). Cryogenic Engineering TM Flynn, New York; Marcel Dekker, 688 S., 195\$(1997).
- [99] Holman, J.P. Heat and mass transfer, Tata McGraw Hill, 8th edition, 1989.
- [100] John, James E.A. Gas dynamics, 2nd edition, Pearson Prentice Hall, 2009.
- [101] Maytal, B. Z. (2008). Open cycle Joule-Thomson cryocooling by mixed coolant. International Cryocooler Conference, Atlanta.
- [102] Anderson, D., Tannehill, J. C., Pletcher, R. H., Munipalli, R., & Shankar, V. (2020). *Computational fluid mechanics and heat transfer*. CRC press.
- [103] Patankar, S. (2018). Numerical heat transfer and fluid flow. CRC press.
- [104] Yang X., Chung J.N., Size effects on miniature Stirling cycle cryocoolers, cryogenics 45(2005) 537-545.
- [105] Thirumaleshwar, M., & Subramanyam, S. V. (1986). Heat balance analysis of single-stage Gifford-McMahon cycle cryo-refrigerator. *Cryogenics*, 26(3), 189-195.
- [106] Miyabe, H., Hamaguchi, K., & Takahashi, K. (1982, August). An approach to the design of Stirling engine regenerator matrix using packs of wire gauzes. In *Proc., Intersoc. Energy Convers. Eng. Conf.; (United States)* (Vol. 4, No. CONF-820814-). Department of Mechanical Engineering, Meiji University, 1-1-1 Higashimita Tamaku, Kawasaki-shi.
- [107] Pande, G. V., & Narayanamurthy, H. (1995). Design studies for Stirling cycle cooler regenerator. *Journal of Spacecraft Technology*, *5*(1), 57-63.
- [108] Chang, H. M., Park, D. J., & Jeong, S. (2000). Effect of gap flow on shuttle heat transfer. *Cryogenics*, 40(3), 159-166.
- [109] Zimmerman F. J., and R. C. Longsworth. Shuttle heat transfer. In Advances in cryogenic engineering 16, 1970, pp. 342-351.